Spring 4-19-2022

Second-Order Enhanced Coupling Strength Grating Out-Couplers for a Monolithic Laser-Electro-Absorption Modulator

Maryam Dezfuli
Southern Methodist University, mdezfuli@smu.edu

Recommended Citation

Dezfuli, Maryam, "Second-Order Enhanced Coupling Strength Grating Out-Couplers for a Monolithic Laser-Electro-Absorption Modulator" (2022). *Electrical Engineering Theses and Dissertations*. 49.
https://scholar.smu.edu/engineering_electrical_etds/49

Second-Order Enhanced Coupling Strength Grating Out-Couplers for a Monolithic Laser-Electro-Absorption Modulator

Approved by:

Dr. Gary Evans

Professor, Electrical and Computer Engineering

Dr. Jerome Butler

Professor, Electrical and Computer Engineering

Dr. Jennifer Dworak

Professor, Electrical and Computer Engineering

Dr. Ping Gui

Professor, Electrical and Computer Engineering

Dr. Ralph Johnson

Chief Technology Officer at Photon Sciences Inc.

Second-Order Enhanced Coupling Strength Grating Out-couplers for a Monolithic Laser-Electro-Absorption Modulator

A Dissertation Presented to the Graduate Faculty of the

Lyle School of Engineering

Southern Methodist University

in

Partial Fulfillment of the Requirements

for the degree of

Doctor of Philosophy

with a

Major in Electrical Engineering

by

Maryam Dezfuli

B.S., Electrical Engineering, University of Tehran, Tehran, Iran
M.S., Photonics Engineering, Amirkabir University of Technology, Tehran, Iran

May 14, 2022

Acknowledgements

This work could not have been accomplished without the wisdom of my fantastic advisor, Prof. Gary Evans, and his colleagues in the Department of Electrical Engineering here at SMU. I want to thank Dr. Ralph Johnson, Professor Nai-Hsiang Sun, and Professor Jerome Butler for their helpful comments and suggestions throughout my journey as a Ph.D. Student. I would also like to thank my colleagues Freddie Castillo II, Weida Zhang, Scott McWilliams, Rue-Hua He, and Kent Liu for contributing to this work.

I am forever grateful to my parents for encouraging me throughout my entire education journey and it has always been my biggest motivation to make them happy and proud even when I live 7273 miles away. Hope this does it!

Dezfuli, Maryam
B.S., University of Tehran, Tehran, Iran
M.S., Amirkabir University of Technology, Tehran, Iran

Second-Order Enhanced Coupling Strength Grating Out-couplers for a Monolithic Laser-Electro-Absorption Modulator

Advisor: Dr. Gary Evans
Doctor of Philosophy conferred May 14, 2022
Dissertation completed Apr 19, 2022

Conventional grating out-couplers in III-V waveguides typically require lengths of several hundreds of microns to outcouple 50 to 90% of the incident optical power. Enhanced coupling strength (ECS) gratings, which reduce the out-coupler grating length to tens of microns, have a large relative permittivity difference between the materials on either side of the grating boundary along with a high index cover layer. With appropriately chosen permittivity and layer thicknesses, the addition of a cover layer "pulls" the peak of the optical mode towards the grating region, resulting in a significant increase in the grating confinement factor. The resulting ECS out-coupler is short, highly efficient, and can be integrated with other III-V optical components, including horizontal cavity lasers and modulators.

The theoretical dependence of the magnitude and spectral width of the out-coupled power as a function of cover layer thickness, low index material thickness, grating depth, and duty cycle is shown using a Floquet-Bloch analysis for two different ECS grating geometries. The design of a high-speed datacom transmitter with ECS grating reflectors and an ECS grating out-coupler is discussed. The proposed laser with an integrated electro-absorption modulator (Laser-EAM) theoretically provides Pulse Amplitude Modulation 2-Level (PAM-2) data rates in excess of

100Gbps with lower latency, less power consumption, and lower cost than existing commercial devices.

Table of Contents

List of Figures

List of Tables

List of Acronyms

ECS – Enhanced Coupling Strength	QW – Quantum Well
ECSL – Enhanced Coupling Strength with Liner	MQW – Multiple Quantum Well
ECSNL – Enhanced Coupling Strength Non-Liner	BAL- Broad Area Laser
MBE – Molecular Beam Epitaxy	DWDM – Dense Wavelength Division Multiplexing
EPI – Epitaxy	
EAM – Electro Absorption Modulator	
BCB - bisbenzocyclobutene monomers	
TE – Transverse Electric	
TM – Transverse Magnetic	
DBR – Distributed Bragg Reflector	
DFB – Distributed Feedback Laser	
OC – Out-coupler	
QW – Quantum Well	
MQW – Multiple Quantum Well	
BAL- Broad Area Laser	
SOG – Spin on Glass	
LIV – Light-Current-Voltage	
FWHM – Full Width at Half Max	
PAM4 - Pulse-Amplitude Modulation 4-Level	
PAM2-Pulse-Amplitude Modulation 2-Level	
NRZ- Non-Return-to-Zero	

Dedication

This work is dedicated to my amazing husband Alexander Ricco Esq. who has been by my side since the very first day of my Ph.D. program. I could not have managed to finish my Ph.D. while working a full-time job if it wasn’t for his love, support, help and presence.

Chapter 1

INTRODUCTION

The idea of integrated photonics originated from integrated electronics which has proven to provide higher performance than non-integrated circuits. Integrated optical circuits or photonic integrated circuits are fully optical circuits made of optical components with some electronic control. These circuits can be fabricated on a common substrate like silicon, silicon dioxide, or indium phosphide (InP). Optical components like amplifiers, lasers, and modulators are the components that can be connected via optical waveguides. InP specifically provides a desirable substrate to build several different optical components due to its direct bandgap. Integrated photonic circuits are generally used in telecommunication, data communications, and sensors. Integrated circuits offer the advantage of simultaneous fabrication of multiple devices and circuitries on a single substrate, which significantly decreases the fabrication costs and increases the reliability of each component as opposed to a structure built from individual components. On the other hand, the compact nature of integrated circuits makes them ideal for applications where the space and weight of the device are essential. Another advantage is that the data transfer rate increases when the interconnects or waveguides are built on the same substrate as other circuit components. This is due to both decreases in the physical distance between the devices and a reduction of parasitic capacitance and inductance between circuits.

Intuitively, building multiple devices on a single chip might seem more difficult and time-consuming. Still, the number of devices produced in a single wafer is enough to make the process more cost-effective at the end of the process. Integrated designs provide higher reliability because all the devices and interconnections are made on the same substrate [1]. However, integrated photonics has faced their own challenges compared to integrated circuits. The problem with integrated photonics is that it has no equivalent for an electrical diode. Instead, an integrated optical waveguide isolator must be used to be able to integrate thousands of optical components.

Integrated photonic circuits are categorized into two types: monolithic and hybrid. An integrated photonic circuit is called monolithic if all components are built on a single piece of a semiconductor like an InP wafer. In contrast, a hybrid circuit may contain more than one monolithic circuit or other components that are connected via interconnections. Monolithic circuits are easier to fabricate and more cost-effective to mass-produce, while hybrid circuits provide better isolation.

This dissertation proposes a new structure for an out-coupler as part of an integrated laser-modulator device. Calculations and simulations provided in this work show advantages of this structure over conventional gratings. The integrated laser-modulator device was fabricated twice as part of a Small Business Innovation Research (SBIR) funded by the Department of Energy to work at a wavelength of 1550nm and again on National Aeronautics and Space Administration (NASA) SBIRs, where the device was modified to accommodate the need to work at a 1310 nm wavelength. Fabrication of the out-coupler was postponed to future phases (a Phase II NASA will begin this summer). However, Enhanced Coupling Strength (ECS) grating simulations showed that filling the grooves with a low index material and adding a high index material as a cover layer on top of the grating would results in significantly higher out-coupled power (second-order Bragg condition) and high reflected power (first-order Bragg condition) for short (on the order of 10 microns) compared to conventional gratings. Such ECS gratings provide over 80 to 90% out-coupling (~ 10 to 20 microns), while conventional gratings require much longer gratings (250 to 1000 microns) to achieve such high out-coupling.

The Laser-EAM can theoretically operate at 100 Gbps non-return-to-zero (NRZ) or 200 Gbps PAM4/channel and utilize coarse wavelength division multiplexing (CWDM) of 6 wavelengths without temperature control. If coupled to a 12-channel fiber ribbon, the aggregate data rate is 7.2 Tbps. Theoretically, the EAM can be driven at greater than 200 GHz. The modulation rate depends on the development of a high-speed electronic driver for the modulator. Demand for such systems is high in all major data centers and high-performance computers [2].

The high integration density of the proposed device makes it attractive for an extensive range of detectors, including calorimeters and trackers. The fundamental laser bandwidth is capacitance-limited with a small modulator section (<40fF capacitance) that can be further reduced. It is temperature insensitive, requires low energy per bit, utilizes a compact (~10 to 20μm long) EAM structure. The small EAM active area minimizes radiation-induced leakage currents.

Some benefits of this Laser-EAM include a significant improvement in energy efficiency, increased bandwidth, and low latency, resulting in a reduction in size and complexity of fiber optic cabling [2].

Furthermore, the proposed laser-EAM is radiation tolerant, making it a good candidate for military, aerospace, and scientific applications. This device does not need error correction or temperature control which significantly decreases the power per bit down to four times less power compared to the state-of-the-art Externally Modulated Lasers (EMLs) and more than 80% reduction in power compared to Si Photonics (SiP) solutions.

Chapter 2

UNDERSTANDING THE PRINCIPLES

In this chapter, theories and principles used for the design and fabrication of the grating out-coupler and the proposed Laser-EAM device are elaborated. Subsequently, each component used in this transceiver device, including the DBR grating, grating out-coupler, laser, electro-absorption modulator (EAM), and the connecting waveguide, is introduced and explained in detail.

2.1. Optical Waveguide Theory

Optical waves are the carriers of optical communications, similar to electrons' role in electrical circuits. Propagation of optical waves in any media, including optical waveguides, follow Maxwell's Equations. Based on James Clerk Maxwell's finding on the electromagnetic theory of light in [3], the four fundamental laws that apply to both electromagnetics and optical signals are as follows:

$$\nabla \times E + \frac{\partial B}{\partial t} = 0 \tag{2.1}$$

$$\nabla \times H - \frac{\partial E}{\partial t} = J \tag{2.2}$$

$$\nabla . D = \rho \tag{2.3}$$

$$\nabla . B = 0 \tag{2.4}$$

Where E with a unit of volts per meter (V/m) and H with an SI unit of amperes per meter (A/m) are the electric and magnetic field intensity vectors, respectively, and the x indicates the curl of the vector. From these two field vectors the electromagnetic wave equation can be obtained for E and H. The electric displacement vector D has a unit of coulomb per square meter (C/m^2) and the magnetic flux density vector B has a SI unit of Tesla. B and D include the effect of media on the electromagnetic waves. And finally, ρ with a unit of coulomb per cubic meters (C/m^3) and

J with a unit of ampere pe squared meters (A/m^2) are the electric charge density (scalar) and the electric current density (vector).

The electric displacement and magnetic flux density vectors are related to the electric field and magnetic field intensity vectors by Eqs. (2.5) and (2.6).

$$D = \epsilon E \tag{2.5}$$

$$B = \mu H \tag{2.6}$$

Where $\epsilon = \epsilon_r \epsilon_0$ is the permittivity of the media with a unit of Farad per meter (F/m) and $\mu = \mu_r \mu_0$ is the permeability of the media measured in Henries per meter (H/m). Hence, Eqs. (2.5) and (2.6) are called material equations. At optical frequencies the magnetic permeability of a material is constant and equal to the magnetic permeability of vacuum $\mu = \mu_0 = 4\pi \times 10^{-7} Hm^{-1}$. However, the dielectric permittivity is wavelength-dependent. This relationship is described in Eq. (2.7) where $\epsilon_0 = 8.854 \times 10^{-12}\ F.m^{-1}$ is the dielectric permittivity of vacuum and n is wavelength-dependent.

$$\epsilon = n^2 \epsilon_0 \tag{2.7}$$

The dielectric constant is defined as $\kappa = n^2 = \epsilon/\epsilon_0$. Maxwell's equations can be solved with the help of equations (2.5) and (2.6). Optical communications usually deal with waves going from one media to another (like in a dielectric waveguide). Therefore, boundary conditions are required to solve the equations in different media and different geometries. [4]

Dielectric slab waveguides are the simplest form of waveguides used in photonics. Figure 1 shows a schematic of symmetric (a) and asymmetric (b) slab waveguides and their different types of fabrication in (c), (d) and (e). For the mode to be guided through the waveguide, it is essential to choose the suitable material for substrate, core, and cladding. In general, the core needs to have a higher refractive index than the substrate and cladding for the mode guiding to happen ($n_{core} > n_{sub} \geq n_{clad}$). In case $n_{sub} = n_{clad}$ there is a symmetric slab as shown in Figure 1 (b).

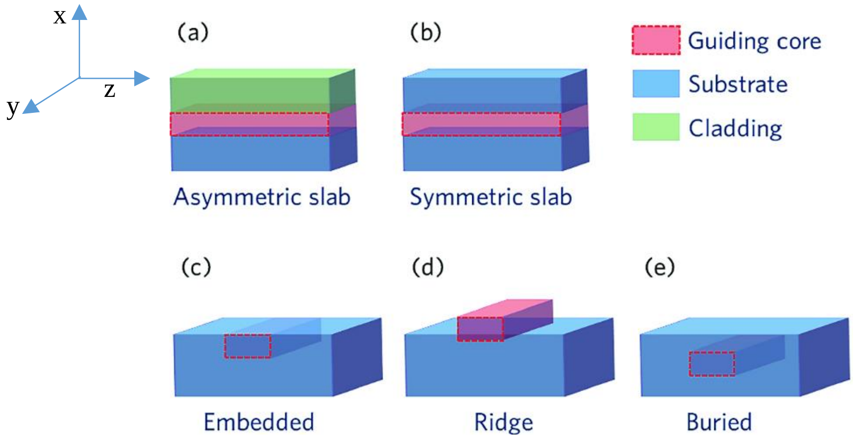

Figure 1 Schematic diagram of different types of slab waveguides [5]

The slab waveguide only guides a limited number of modes called guided modes that would be guided in its maximum level at a specific frequency and is cut-off if the frequency is far enough from that frequency. However, solving the maxwell equations for a slab waveguide produces the answer to both guided and unguided modes, and boundary conditions must be used to find the eigenvalue equations for the guided modes.

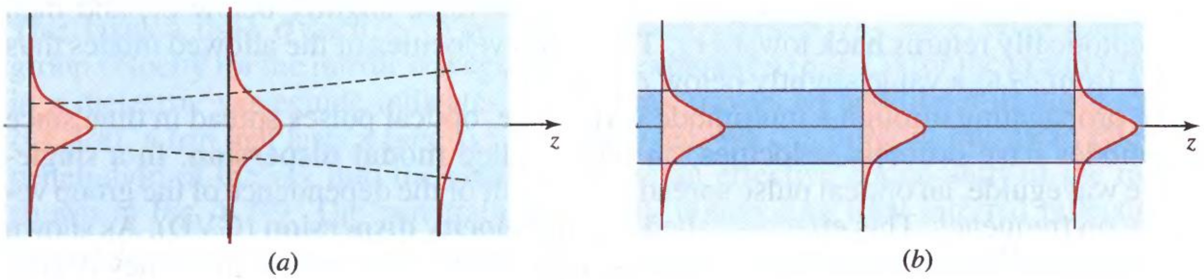

Figure 2 Field distribution of (a) Gaussian beam in a homogenous medium and (b) guided mode in a dielectric waveguide [6]

Before addressing the TE and TM mode solutions to Maxwell's equations, it is worth looking at the guided modes in a slab waveguide from a ray optics point of view to explain a few constants that will be used in future chapters.

In Figure 2 (a), the wave travels mainly in the core layer. In ray optic terms, this is a result of total internal reflection happening since $n_{core} > n_{sub} \geq n_{clad}$, meaning the optical ray is confined in the core layer. Total internal reflection happens when light propagating through a media comes across a boundary with a lesser index of refraction and therefore bends away from the normal.

Figure 3 shows a simple planar slab waveguide schematic when light propagates through it. The angle at which total internal reflection happens is called critical angle (θ_c) and follows $\sin\theta_c \geq \frac{n_{sub}}{n_{core}}$ and $\sin\theta_c \geq \frac{n_{clad}}{n_{core}}$. Therefore, for the light to be reflected from both boundaries and trapped inside the core region without leaking out (light to be confined), the refractive indices of the three regions should be selected in a way that the angle θ is equal or greater than the largest critical angles described above. Snell's law describes the relationship between the angle of incident and the angle of refraction when light travels from medium one to medium two. This is described in Eq. (2.8) where θ_1 is the angle of incident and θ_2 is the angle of refraction.

$$n_1 \sin\theta_1 = n_2 \sin\theta_2 \tag{2.8}$$

Now using the definition of critical angle, if $\sin\theta_2 = \sin 90° = 1$ is plugged into Eq. (2.8), the critical angle as described in (2.9) is produced.

$$\sin\theta_c = \frac{n_2}{n_1} \tag{2.9}$$

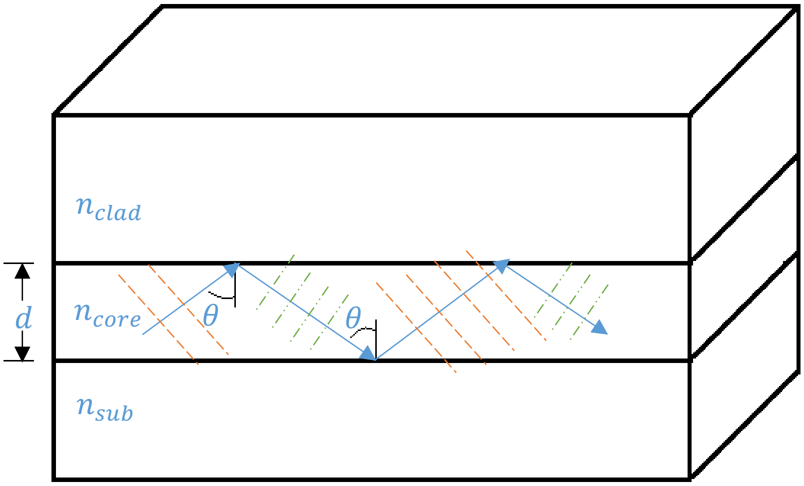

Figure 3 Propagation of light in a slab dielectric waveguide from a ray optics point of view

From a wave optics point of view, light travels in the direction shown by the blue arrows in Figure 3 in the form of plane waves that can be identified with their propagation constants, $k = k_0 n_{core}$ where k_0 is the free space propagation constant. The phase fronts shown in dashed lines suggests that the total field propagating through the waveguide can be seen as the sum of two uniform plane waves. The propagation constant of a plane wave is a vector in the direction of propagation. Therefore, the propagation constants for the two plane waves propagating through the waveguide in Figure 3 are as shown in Figure 4 where h and β are the components of the propagation constant in x and y direction and are called transverse and longitudinal propagation constants, respectively.

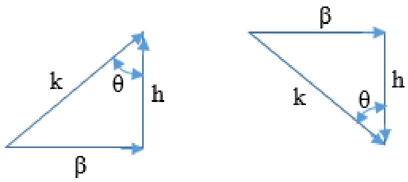

Figure 4 The propagation constant for the two plane waves traveling through the waveguide

Considering the sum of the two vectors, it is clear that the transverse propagation constants h interfere to produce the transverse mode pattern. The sum of βs create the longitudinal propagation mode in the z-direction. From trigonometry, the relation between β and k is as follows.

$$\beta = k \ \sin\theta = k_0 n_{core} \sin\theta \tag{2.10}$$

Defining the effective index as $n_{eff} = n_{core} \sin\theta$ illuminates the formula relating the effective index of the media to the longitudinal propagation constant as expressed in Eq. (2.11).

$$\beta = k_0 n_{eff} \tag{2.11}$$

In other words, effective index changes the wavelength of the traveling wave in free space wavelength λ_0 to $\lambda_g = \frac{\lambda_0}{n_{eff}}$ in the waveguide [7]. Knowing the relationship between the wavelength and propagation constant $k_0 = 2\pi/\lambda_0$ the relationship between the propagation constant and the effective index of the media can be found as shown in Eq. 2.12

$$k = \frac{2\pi n_{eff}}{\lambda_0} \qquad 2.12$$

2.2. Modes of the Waveguide

Modes describe the field distribution of a propagating wave in the waveguide. This propagating wave can either have a form of guided-mode (transverse), radiations mode (longitudinal), or leaky mode. For a lossless dielectric waveguide, the power in the waveguide is simply the sum of the power carried by each mode [4]. The guided and radiation modes are orthogonal to each other.

Maxwell's equations must be solved to find the modes propagating in a dielectric slab waveguide. Considering the coordinates shown in Figure 1, it is safe to assume that the electromagnetic field remains the same in the y-direction which simplifies Maxwell's equations.

There are two types of waveguide modes, TE or transverse electric and TM or transverse magnetic. TE modes are the ones with no electric field in the direction of propagation, therefore only have E_y, H_x and H_z components. TM modes are the ones with no magnetic field in the direction of propagation, therefore only have H_y E_x and E_z components. Assuming the slab is infinite in the yz plane a periodic time-dependent complex parabolic such as $e^{j\omega t}$ can describe the field where ω is the angular frequency and is related to the wave frequency with $\omega = 2\pi f$. Since the waveguide is intended to carry the signal in a longitudinal (z) direction it can be assumed that the field within the waveguide varies as $e^{-\gamma z}$ where $\gamma = \alpha + j\beta$ is the complex propagation constant, α is the attenuation constant and β is the phase constant. Combining these time-dependent and space-dependent factors produces Eq. (2.13), which describes a wave traveling within a waveguide in positive z-direction.

$$\psi = e^{j\omega t - \gamma z} \tag{2.13}$$

Now, employing $\gamma = \alpha + j\beta$ and assuming the attenuation is negligible $\alpha = 0$ produces the field distribution as a function of the longitudinal propagation constant shown in Eq. (2.14).

$$\psi = e^{j\omega t - j\beta z} = e^{j(\omega t - \beta z)} \tag{2.14}$$

The relationship between the angular frequency ω and the propagation constant β in a waveguide is called the "Dispersion Relation". Defining the phase velocity of the wave as shown in (2.15) gives the dispersion relation. In this equation, the phase velocity, ν_P, is an indication of the speed at which the wave travels in the medium.

$$\nu_P = \frac{\omega}{\beta} \tag{2.15}$$

This suggests that the relationship between ω and β is directly related to the wave speed in that medium. The propagation constant of free space is $k = \omega/c$ where c is the speed of light in free space and the propagation constant of the waveguide is β. From Eq. (2.14) the relationship between these two can be found using the electric and magnetic fields components of $e^{j(\omega t - \beta z)}$. Figure 5 shows a generic $\omega - \beta$ diagram for a dielectric waveguide where three of the guided modes are shown within the guided region.

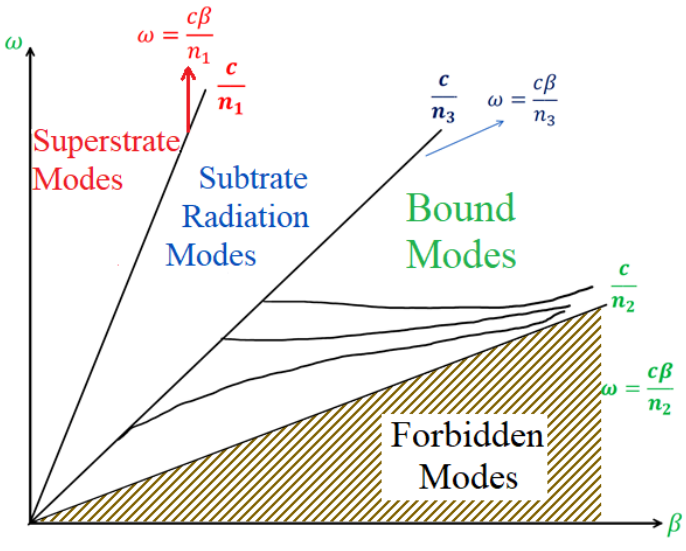

Figure 5. $\omega - \beta$ diagram of a typical dielectric waveguide

Only a discrete, limited number of guided modes are allowed within the guided region. In the forbidden region, where ω/β is smaller than $\frac{c}{n_2}$, modes are not allowed. For $\frac{\omega}{\beta} > \frac{c}{n_3}$ continuum of radiation modes exists either in the substrate or superstrate. Bound modes are only achieved if $\frac{c}{n_2} < \frac{\omega}{\beta} < \frac{c}{n_3}$. Limiting the frequency to stay between the cut-off from fundamental mode ($\nu = 0$) and the first-order mode ($\nu = 1$) guarantees single-mode propagation which is ideal for broadband applications [8]. Assuming $n_{sub} > n_{superstrate}$ condition for a bound mode is as follows

$$n_{sub}k \leq \beta \leq n_{core}k \tag{2.16}$$

Dividing this equation by k yields the boundaries for β as follows:

$$n_{sub} \leq \beta/k \leq n_{core} \tag{2.17}$$

Eqs. (2.11) and (2.16) results in the boundaries for the effective index of the guided mode propagating through the waveguide as follows:

$$n_{sub} \leq n_{eff} \leq n_{core} \tag{2.18}$$

2.3. Semiconductor Materials

Semiconductor materials belong to a group of materials whose conductivity lies between that of conductors and isolators. What makes them appealing is that their conductivity can be controlled with impurity content, temperature, and optical excitement. By doping (inserting appropriate elements to add electrons and holes), the conductivity of a semiconductor can be increased by 8 orders of magnitude. Semiconductors can be a single element (elemental) like silicon (Si) or germanium (Ge) from the fourth group in the periodic table. Semiconductor materials are also combinations of group III and V elements from the periodic table such as indium phosphide (InP) and gallium arsenide (GaAs). Certain combinations from column II and VI and from column IV also make semiconductor materials. Compound semiconductors are not only limited to the combination of two elements; they can be composed of multiple elements, for example aluminum indium gallium arsenide (AlInGaAs).

Electrical conductivity depends on the capability to flow electrons which is intrinsically available in metals since they have partially filled bands. While in semiconductors, electrons (or holes) should be excited from the valence band to the conduction band for them to be conductive. The valence band is the highest energy level at which electrons are commonly present at absolute zero (0 Kelvin) in semiconductors. In contrast, the conduction band is the lowest range of energy available for the electrons to move to.

When growing multiple layers of different semiconductors on top of each other (epitaxial growth), the two materials stacked on top of each other should have the same lattice constant (lattice matched) unless the layer is very thin. The percentage of each element can be controlled in compound semiconductors to assure lattice matching at a specific wavelength using Figure 6. For instance, to grow an $In_xGa_{1-x}As$ layer on top of an InP substrate the x value can be found as shown in Figure 6 with dashed lines connecting InP to the $In_xGa_{1-x}As$ line to be x = 0.53.

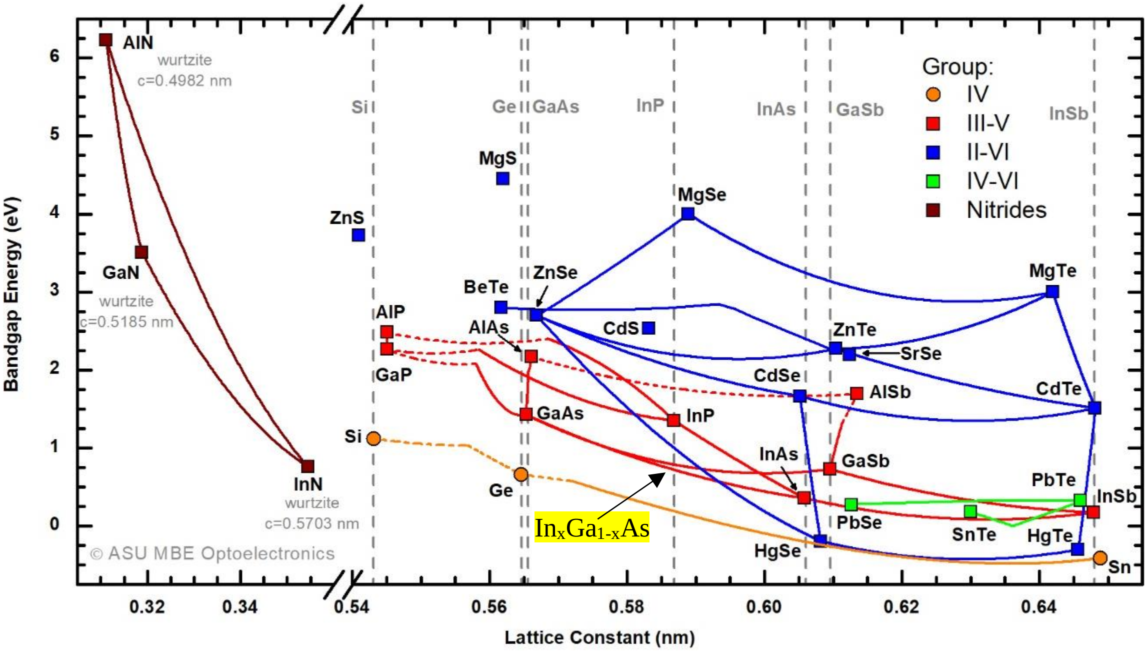

Figure 6 Bandgap as a function of lattice constant for compound semiconductors [9]

Semiconductors are divided into two categories based on to their bandgap: direct and indirect. In a semiconductor with a direct bandgap, an electron from the conduction band can recombine with a hole in the valence band and emit a photon. This emitted photon has an energy equal to the bandgap energy (E_g). On the other hand, the energy of a photon is directly related to the frequency with Plank-Einstein relation described in (2.19) where $h \approx 4.135 \times 10^{-15} \mathrm{eV/Hz}$ and f is the frequency in Hz.

$$E_{photon} = h.f \tag{2.19}$$

Therefore, converting frequency to wavelength ($f = c/\lambda$) and plugging in the constants h and $c = 2.99 \times 10^8\ m/s$ reveals the quantized energy an electron emits when recombination happens as shown below.

$$E_{photon} = E_g = h.f = \frac{h.c}{\lambda} \rightarrow E_{photon}(eV) = \frac{1.2398}{\lambda(\mu m)} \tag{2.20}$$

Figure 6 shows the solid lines that indicate direct bandgap material and the dashed curves that indicate indirect bandgap material. Materials made from combination of III-V components radiate from the infrared to the ultraviolet frequencies. However, adding some Al to GaAs producing AlGaAs will shift the wavelength into the red region of the visible range of light spectrum and create red visible diodes/lasers. An interesting observation from Figure 6 is that to create devices for optical communications (1.3μm to 1.5μm shaded area), only combinations of GaAs, InAs, AlAs, GaSb and InP can be used.

2.4. Semiconductor Lasers

LASER is an acronym for Light Amplification by Stimulated Emission of Radiation. The first laser was invented in 1960 at Hughes Research Lab. Since then, lasers have come a long way. There are several types of lasers, including semiconductor lasers. However, the principle of how lasers operate, is shared between all. Simply put, a laser is an oscillator that includes an active medium at which the radiation interacts with and creates coherent radiation [10]. Semiconductor lasers have semiconductor materials as their active medium and compared to other types of lasers can be designed in small sizes and for a specific frequency. They have been improved continuously to achieve narrow spectral bandwidth, low threshold current, low cost, high optical power output, and low power consumption. They can also be easily modulated, which makes them attractive for optical communications. Some of the disadvantages of semiconductor lasers are: higher linewidth compared to gas lasers, lower peak power, temperature variability and lower coherence. However, the advantages outweigh the disadvantages specially since they are compatible with optical fibers.

Semiconductor lasers can be categorized as bipolar or unipolar. In the former, the radiation is formed from the transition of electron/hole carriers between the valence band and conduction band. The latter indicates the carriers transitioning between three sub-bands within the conduction band. Hence, for a bipolar semiconductor laser, the energy of the photon emitted from recombination equals the bandgap of the semiconductor, while the energy of photons emitted in unipolar semiconductor lasers is much smaller than the bandgap of a semiconductor.

Figure 7 (a) indicates a double heterostructure semiconductor laser. If this p-i-n junction is forward biased, the electron and holes will be injected into the active region at which they recombine, as shown in Figure 7 (b) and (c). The energy of each photon emitted from recombination of an electron-hole pair is equal to $h\nu \leq E_g$ where E_g is the bandgap. Since these optical radiations all have the same frequency, ν, they coherently add to the optical field in the active region. These radiations experience gain (lasing) in the active region only if the injected current is more significant than a specific value called *threshold current*. Reducing the thickness of the active region naturally decreases the threshold current, and that explains the main idea behind the invention of quantum well lasers [11].

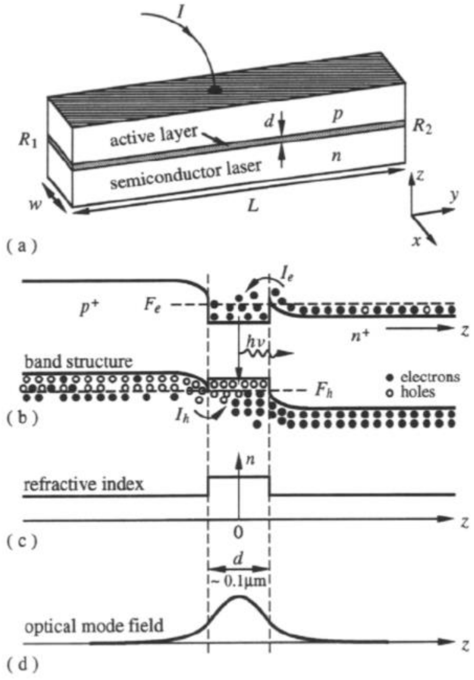

Figure 7 A schematic description of a semiconductor laser diode (a) the laser device geometry; (b) the energy band structure of a forward biased double heterostructure laser; (c) the spatial profile of the refractive index that is responsible for the dielectric waveguiding of the optical field; (d) the intensity profile of the fundamental optical mode. [12].

First lasers were made of homojunction structures, then single heterojunctions were introduced followed by then double heterojunctions that deployed thick active layers, then thin active layers (0.1 microns) in 1970 that allowed continuous wave operation at room temp for such lasers. *Separate confinement heterostructures* (SCH) which provides separate confinement for carriers in the active layer by confining the mode and provides separate confinement for the optical field which gives better performance than a simple double heterostructure. Later, in the late 1970s by mid 80s came SCH QWs were introduced and developed.

2.4.1. Quantum Well Lasers

Quantum well lasers are made of a thin nano-layer of undoped material (typically in nanoscale) called *quantum well* that acts as their active region. Active region is sandwiched between a p-type and an n-type material that inject holes and electrons, respectively. This forms a forward biased p-i-n diode as shown in Figure 7. Development of growth techniques in the 1970 and 80s, such as molecular beam epitaxy (MBE) and metal-organic chemical vapor deposition (MOCVD) enabled the deposition of ultrathin layers of semiconductors (single atomic layers), helped with the realization of quantum well lasers, and their popularity [12].

Deploying multiple quantum wells (MQW) separated by thin barriers, adjusting the well width, optimizing the barrier heights, thickness and refractive index leads to obtaining separate optical wave confinement and having efficient low threshold current lasers. In particular, introducing aluminum contents in the outer layers, was a breakthrough to extremely efficient MQW lasers [13].

In designing multiple quantum wells, the thickness of the barriers between each well is an essential factor. If the thickness of the barriers is big enough, the electrons are trapped in each well and have discrete bands. On the other hand, if the thicknesses of the barriers are comparable to the thicknesses of the well, electrons are going to be able to tunnel through these barriers and communicate with the electrons in the other wells. As a result, the energies of the electrons in the quantum wells form minibands and the electrons, and the holes form a superlattice.

Characteristics of lasers depend on optical confinement (trapping the light inside the gain media with the help of mirrors) and carrier confinement. Optical confinement can be achieved by having an active region with a higher refractive index than the cladding. Carrier confinement is also vital since confining the electron-holes in the active region increases the probability of radiative recombination which only depends on the material. However, the laser threshold is dependent on stimulated emission which increases when recombination and the optical field strongly overlap. A significant difference in the bandgap between the active region and cladding layers highly increases the carrier confinement, which explains the advantage of double-heterostructure lasers. Quantum well lasers provide an even more significant potential barrier between the well and barrier material and decrease the chance of tunneling.

2.4.2. Distributed Bragg Reflector Lasers

Distributed Bragg reflectors or DBRs are periodic structures that act as passive components that can reflect, transmit or couple out the light propagating inside a laser's active area. DBR Lasers are edge-emitting lasers named after the reflectors that are fabricated along one or both ends of the single-mode ridge waveguide that acts as the active region. One of the mirrors is designed with high reflectivity to provide resonance for the active region. In contrast, the other mirror has a lower reflectivity that could be a DBR or a cleaved surface that enables light to exit in-plane with the laser. Injecting current into the gain media creates a laser. The end mirrors are also designed to reflect the same longitudinal mode. As a result, DBR lasers are considered among single mode lasers [14].

The wavelength of DBR lasers can be tuned or fixed (for example in a WDM grid). The amount of current applied to the active region can control the operating wavelength. This working frequency is also highly dependent on temperature so that it can be tuned by temperature. Both these effects can be explained by the change in the refractive index of the gain material when applying current or temperature [15]. The operating wavelength shifts with a rate of 0.002 nm/mA towards longer wavelengths when increasing the applied current, as shown in Figure 8 (a). On the other hand, increasing temperature will shift the wavelength with a rate of 0.09 nm towards longer wavelengths, as shown in Figure 8 (b). Therefore, when designing a DBR laser, it is essential to design the mirrors to work over a wide range of frequencies to accommodate for this wavelength shift [16].

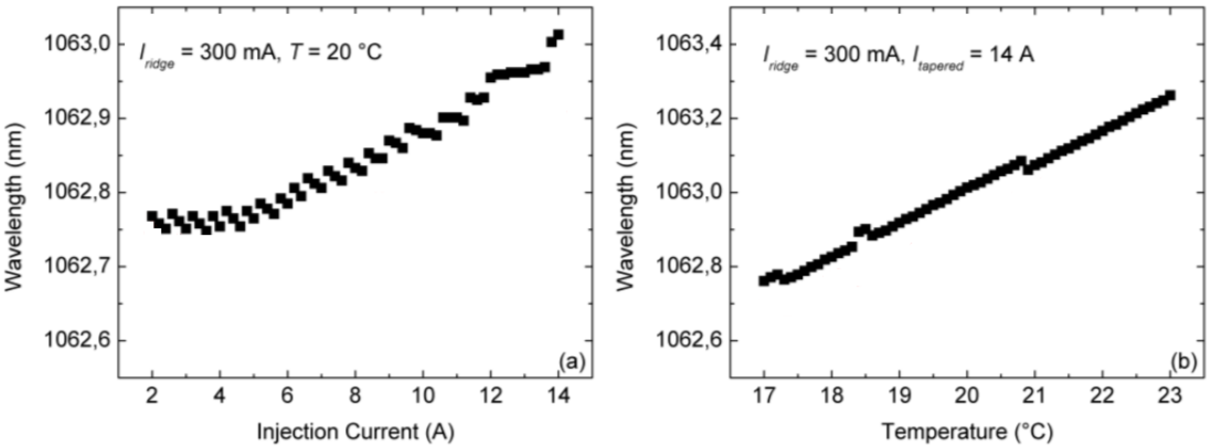

a) b)

Figure 8. Wavelength as a function of a) Injection current in amps and b) temperature in Celsius for a DBR laser [16].

2.4.3. Laser threshold and efficiency

The condition for laser oscillation has an amplitude component and a phase component. The phase condition requires the feedback signal to be coherent with the original signal. The amplitude condition for a laser to resonance requires the optical feedback to be sufficient to overcome the losses and is given by:

$$g_{th} = \Gamma_{active} \times g = \frac{1}{2\mathrm{L}} \ln\left(\frac{1}{R_1 R_2}\right) + \alpha_{int} \tag{2.21}$$

Where g_{th} is the threshold gain, Γ_{active} is the active layer confinement factor that accounts for the portion of the power that is contained in the active layer. The gain in the active region is g, L is the cavity length, R_1 and R_2 are the reflectivity of the front and back mirror and α_{int} is the loss in the active region [17], [18]. The confinement factor of the active region is equal to the confinement factor of a quantum well and can be found from Eq. (2.22).

$$\Gamma_{\text{active}} = \frac{\int_{active} |E(x)|^2\, dx}{\int_{-\infty}^{\infty} |E(x)|^2\, dx} \tag{2.22}$$

Threshold current density is another factor that needs to be confined to improve the laser efficiency, reduce the heating and stabilize the fundamental mode. Which can be achieved by reducing the area of the device that is electrically pumped (i.e., the active region length).

An ideal laser outputs an optical power equal to the energy produced by the total recombination of electron-holes. It completely emits out of the laser without being absorbed within the laser. However, this is not the case in reality. In reality, not all the electron-hole recombination emits photons, but some would dissipate energy in other forms, such as heat. On top of that, some of the produced photons get reabsorbed before they can find their way out of the active region. There are two parameters used to indicate the efficiency of lasers: External Differential Quantum Efficiency and Internal Quantum Efficiency.

Internal Differential Quantum Efficiency (η_i) is a parameter that indicates the ability of a laser structure to convert the injected current (electron-holes) into photons. This parameter does not account for whether the entire produced light makes it out of the laser, it only accounts for the recombination to photon generation ratio. Therefore, η_i is a measure of the material quality rather than geometry of the laser, such as the width or length of active region.

On the other hand, external differential quantum efficiency, η_d, is a measure of how efficient the entire laser design is, which is the ratio of total output light to the injected current, and is shown as follows:

$$\eta_d = 2\frac{\Delta P}{\Delta I}\left[\frac{q\lambda}{hc}\right] \tag{2.23}$$

Here, $q\lambda/hc$ is the slope of the L-I curve of an ideal laser emitting light with the wavelength λ, h is Plank's constant and c is the speed of light, and $\Delta P/\Delta I$ is the slope of the L-I curve of the actual laser [19]. Therefore, external differential quantum efficiency is a unitless parameter. The term 2 indicates that this particular laser is designed to have two mirror facets. If light is only coming out of one facet, this changes to 1.

The two parameters η_i and η_d are related to each other as shown below:

$$\eta_d = \eta_i \frac{\ln 1/R_f}{2\alpha\mathrm{L} + \ln(1/R_f R_r)} \tag{2.24}$$

Where α_i is the internal loss, R_f is the reflectivity of the front mirror, R_r is the reflectivity of the rear mirror, and L is the length of the laser cavity. Setting $L = 0$ results in $\eta_d = \eta_i$, which proves that η_i is independent of the geometry and is intrinsic to the material used in the active region [20], [21]. For surface-emitting lasers, it is assumed that the rear mirror is 100% reflective $(R_r = 1)$ so the entire output light comes out of the front mirror [17].

2.5. Electro-absorption Modulator

Electro-absorption modulators are quantum well modulators that work on the principle of quantum Confined Stark Effect (QCSE). QCSE refers to shifting the absorption spectrum due to an applied field. To better understand the Stark Effect, the absorption spectrum of semiconductor bulk material can be compared with those of quantum well structures. When a photon with energy higher than the bandgap of a semiconductor is introduced to the semiconductor, an electron-hole pair is formed by absorbing the photon. The electron moves to the conduction band, leaving behind a hole in the valence band. This electron-hole pair attract each other due to the Coulombic force to form a bound-state called an *exciton*. This energy is minimal which makes excitons very fragile. Therefore, excitons are only observable at low temperatures for a bulk material. On the other hand, in a quantum well structure, excitons are confined and therefore are held closer to each other increasing their binding energy by a factor of two or three [22]. This makes the excitons effect stable enough to be more significant at room temperature for quantum well structures as opposed to semiconductor bulk materials, as shown in Figure 9.

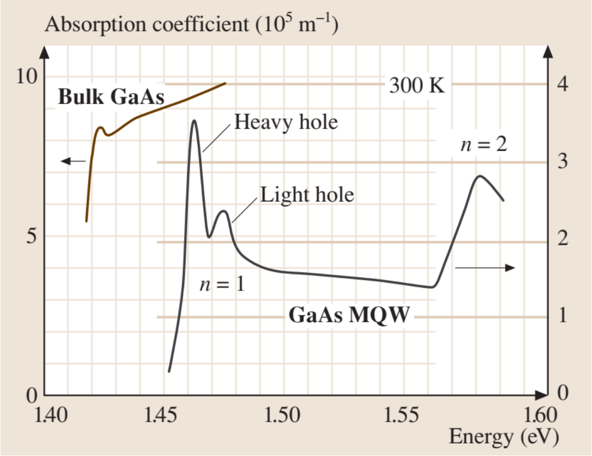

Figure 9. The absorption spectrum of bulk GaAs and a GaAs-Al0.28Ga0.72As 77 quantum well structure at room temperature [20].

The peaks on both curves indicate the existence of excitons. Comparing the two curves shows that even at room temperature, the excitons create a noticeable peak in the absorption spectrum of the MQW structure. Furthermore, the formation of energy sub-bands in MQW structures makes light or heavy holes peak at different energy levels. Thus, there are two peaks in the absorption spectrum of MQW structures. Another point to notice in Figure 9 is that the absorption band-edge of the MQW structure is larger than that of the bulk GaAs.

Lowering the temperature imposes two effects on the absorption spectrum. First, it shifts the bandgap to higher energy levels (shift to the right in Figure 9). Second, it sharpens the exciton peaks because their energy is more observable at lower temperatures. Applying an electric field to the semiconductor creates the same effect in the absorption spectrum, as shown in Figure 10 (b). This shift of energy in the absorption spectrum is due to QCSE. Figure 10 (a) shows the effect of applying an electric field on the bandgap and exciton wavefunction. The tilt in the bandgap enables the electrons to move from the valence band into the conduction band while remaining at the same energy level, and this mechanism is called tunneling.

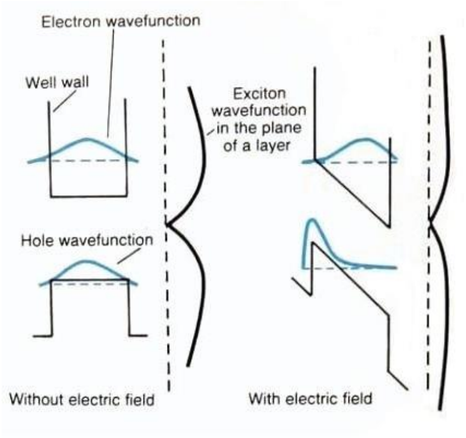

Figure 10. Excitonic wavefunction with and without an applied electric field [22].

The electron and hole wavefunctions become asymmetric because of the applied electric field. When a positive field is applied, the electrons move towards the positive electrode while the holes move towards the negative electrode while the barrier is still confining them. Therefore, the electron and holes wavefunction peaks are separated, as shown in Figure 10. The energy levels also drop since the wavefunctions reside more strongly in the deeper part of the well.

Note that an electric field in order of $10^4 V/cm$ is relatively small due to the quantum well structure usually having a very small thickness. Therefore, an applied voltage of 1V would create the required electric field to exploit the structure as an electro-absorption modulator. Figure 11 illustrates the shift in the absorption spectrum as a function of wavelength for different applied bias voltages for an InAsP/GaInP MQW structure.

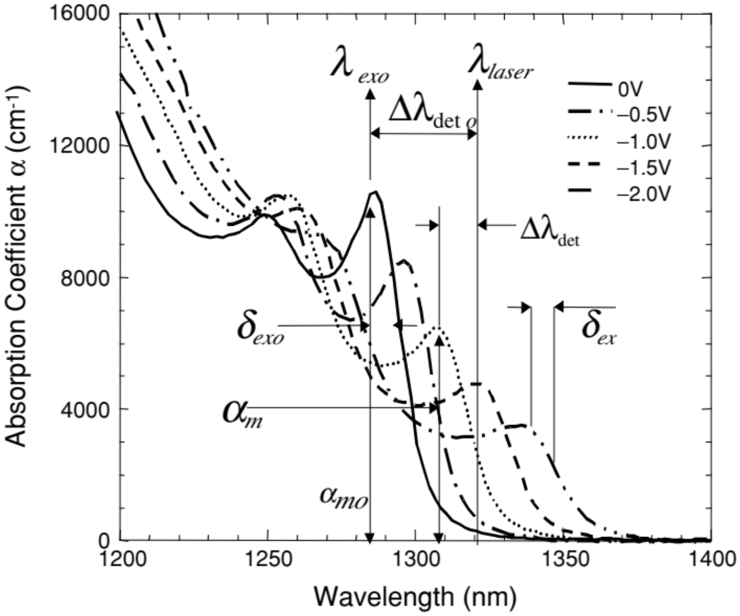

Figure 11. Absorption spectrum of InAsP/GaInP MQW for different applied voltages [23].

Optical extinction ratio is defined as the ratio of the two power levels when the optical power is on and off, respectively. Multiple quantum well electro-absorption modulators tend to provide large optical extinction ratio with low bias voltages due to the QCSE effect that causes the absorption coefficient to change drastically.

The optical intensity in and out of the EAM is related to the attenuation coefficient as follows:

$$I_{out} = I_{in} e^{-\alpha d} \tag{2.25}$$

Where α is the absorption coefficient with a unit of cm^{-1} and d is the total thickness of the active region (quantum well widths only, since barriers are transparent due to large bandgap compared to the quantum well). If α is in an order of $10^4 cm^{-1}$ then to achieve a ratio of

$P_{out}/P_{in} = e^{-1}$ assuming the well width is $10nm$, at least 100 quantum wells are needed for vertical illumination. For longitudinal excitation the mode is traveling in the direction of the wells and can overlap for long distance. Still because the quantum well confinement factor is not 1 it is advantageous to use several wells to increase the confinement factor and use a regime with high absorption. To achieve significant, measurable attenuation (which is the key to a high extinction ratio for an EAM) many quantum wells need to be used. EAMs are traditionally very long devices when they are made to use in low absorption regime. However, if the EAM operates in a very high absorption regime, that allows the devices to be shorter. A shorter device would yield a low capacitance, therefore, easier to drive at high speeds and not suffering from transmission delays. This is the principal concept used in designing the EAM for the laser-EAM device in this work.

From the definition of extinction ratio in Eq. (2.26) one can design the EAM for best performance at a particular bias field by maximizing $\Delta\alpha$ through material design and epitaxial growth considerations.

$$E.R. = \frac{I_{out}(E|_{bias})}{I_{out}(E=0)} = \frac{I_{in}e^{-\alpha|_{bias}L}}{I_{in}e^{-\alpha_0 L}} = e^{-(\alpha|_{bias}-\alpha_0\,)L} = e^{-\Delta\alpha.L} \tag{2.26}$$

Where I is the intensity of propagating mode, $\Delta\alpha$ is the average change in the attenuation coefficient due to the applied field E_{bias}. Using the waveguide configuration of the EAM which is an elevated ridge, as shown in Figure 12, the length L can be altered to increase the extinction ratio. Other design considerations to take when designing EAM include the index and the thickness of the waveguide core, the ridge's length, L, and the ridge's width, W. The design and fabrication of metal contacts, as well as the p-i-n structure, are key factors to achieve low series resistance and low capacitance [23].

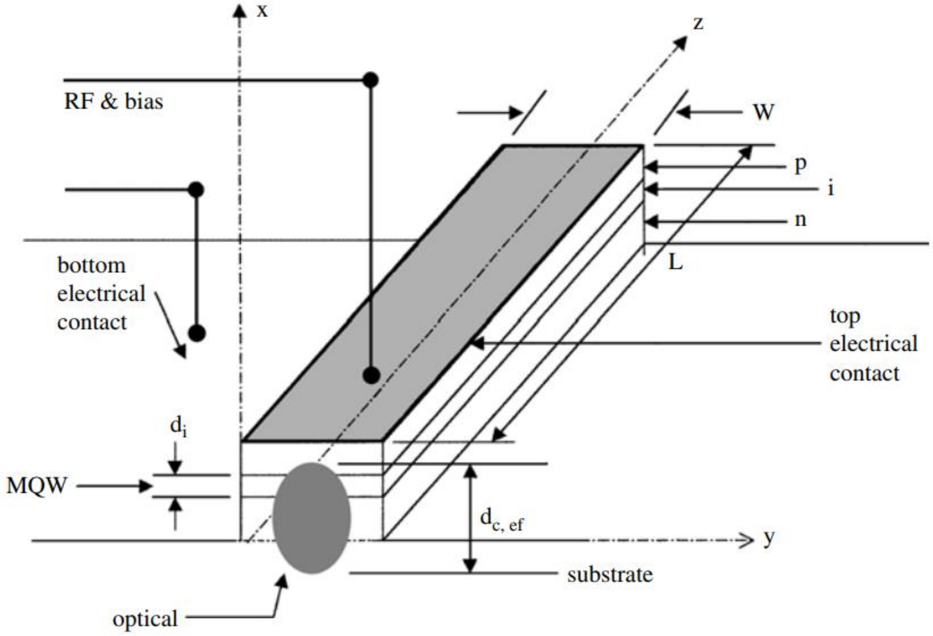

Figure 12. Schematic diagram of a basic ridge waveguide MQW EAM [23].

From a circuit point of view, the bandwidth of the p-i-n modulator highly depends on its capacitance, C and resistance, R. The modulation speed of the electro-absorption modulator is also limited by transmission delays. To avoid transmission delays in long low absorption EAM's the EAM itself is used as an electrical transmission line so that the applied electrical signal travels at the same rate as the optical mode. [23]. For short high absorption EAMs without significant transmission delays as used here R and C are minimized. Sources of delays then are the internal RC of the device, and parasitics such as the bond pad capacitance, any wire bond inductance, the driver impedance and small transmission delay from the bond pad to the device, These are all minimized through appropriate design. For example, flip chip mounting can be used to avoid the bond wire inductance. For these short devices projected bandwidth of > 100 GHz can be achieved if all the speed limiting issues are addressed. The internal capacitance is a primary concern and is addressed by having a thick active region with many quantum wells, as well as keeping the area small by using the high absorption regime and a high quantum well confinement factor.

$$L.W \leq \left(\frac{C}{\epsilon}\right) d_i \tag{2.27}$$

Where L is the EAM length, W is the width of the EAM, ϵ is the dielectric constant, and d_i is the thickness of the active region (MQW) as explained in Figure 12. From Eq. (2.27) modulator can be designed to reach a certain speed by decreasing the length or width of the EAM, increasing the number of quantum wells, or choosing a low index material. In a well-designed EAM, within a few pico-seconds, carriers settle in steady-state, and the active area acts as a variable capacitor whose capacitance depends on the absorbed optical power and applied reverse bias voltage [24].

The quantum wells should be specifically designed to have a substantial absorption response at the operating wavelength which would result in a short EAM with a low capacitance that is easy to be driven. Due to two effects the EAM's absorption curve changes with applied reverse voltage. First, the standard Stark shift makes the absorption edge move to longer wavelengths. Second, the reduction in the overlap of the electron and hole wavefunctions causes a reduction in absorption when increasing the applied reverse bias.

The reduction in absorption when increasing the bias voltage due to the decrease in wavefunction overlap is helpful generally over a wider temperature range than the standard Stark Shift, but either can be useful depending on both the details of the design, and the matching of the lasing wavelength to the absorption spectrum. The specific needs of each design determine which effect is optimal. The wavefunction overlap method is often more desirable than the standard Stark effect since it often has a more significant wavelength tolerance. However, carriers in transit cause a positive feedback effect which can limit the maximum modulated power resulting potentially in a locking up in one state. For the method of shifting the band edge the carriers in transit cause a negative feedback effect which limits the power handling capability by reducing the effect.

The quantum wells growth method also significantly affects the device performance. The MOCVD growth method is more susceptible to poor interface abruptness for group V compounds compared to the MBE method. Poor interface abruptness limits the well deepening when the bias voltage is applied which decreases the effectiveness of the Stark effect. It also works against the wavefunction overlap effect by preventing the desired separation and keeping the carrier wave functions together. The reduced absorption change with bias limits the optical extinction ratio achievable in device operation [2].

Commercial EAMs are traditionally very long high-power devices that operate in low-absorption regimes. Long EAMs have limitation on their speed due to long transmission times, because of working in low-absorption regimes. On the other hand, EAMs are mostly used in long distance communications which makes them require high operating powers which long low absorption devices are ideal for.

The EAMs designed for the Laser-EAM device in this work, are specifically important because they are designed as small low-capacitance devices that operate faster than commercial EAMs. Such EAMs are designed to be used in short-haul, low power applications, enabling them to work in a high absorption regime which allows for very short devices with low capacitance which in turn results in extremely fast modulators.

The EAMs share the same design and epi stack as the laser area and they both have a high quantum well confinement factor since quantum wells are specifically designed to deliver high absorption response for the EAM at the lasing wavelength. Since the quantum wells are shared between the two, the EAM absorption peak tracks the lasing wavelength when it changes with temperature which enables a short EAM that yields lower capacitance, which in turn allows for a fast modulation with greater than 100Gbps operation. Figure 13 shows the calculated absorption for the EAM as well as the laser gain at temperatures (a) 25˚C and (b) 125˚C.

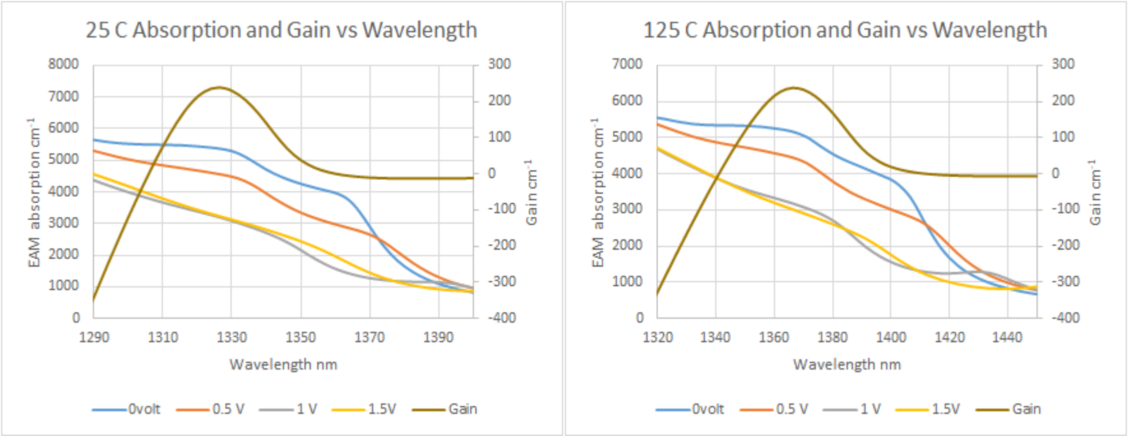

a) b)

Figure 13. Absorption and gain at (a) 25C and (b) 125C for applied voltages of 0, 0.5, 1, 1.5V [2].

The lasing wavelength occurs at a longitudinal mode near the peak gain shown in Figure 13. The changes in the absorption curves with applied reverse voltage are due to combination of two effects: (1) the absorption edge shifts to longer wavelengths due to the standard Stark shift, and (2) the reduction in overlap of the hole and electron wavefunctions causes a reduction in absorption with higher applied reverse bias. For the nominal "1310 nm" quantum well design, the region of reduction in absorption with increasing bias resulting from the decrease in wavefunction overlap is useful at both temperature extremes and intermediate temperatures.

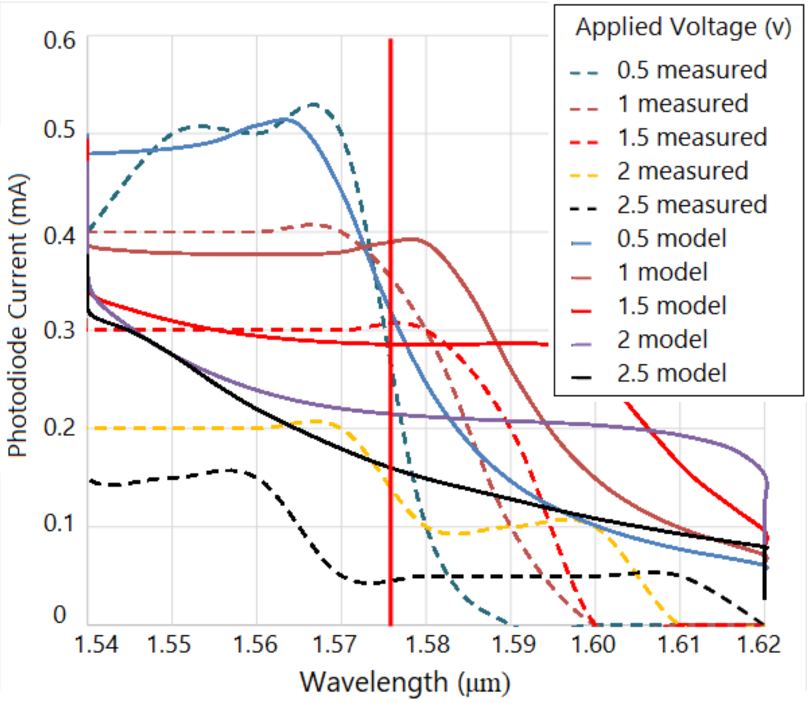

Figure 14. Experimental and theoretical photodiode current from proposed EAM operating as a photodiode as a function of illuminating wavelength and reverse bias voltage. The vertical red line indicates the measured lasing wavelength [2].

Design of the quantum well determines which of the two effects is in use. Both effects must be considered in designing the EAMs, but the wavefunction overlap method generally has the advantage of being effective over a larger wavelength, temperature and voltage range in maintaining the wavelength alignment between the laser and EAM.

2.6. Modulation Formats

Various modulation formats have been deployed to satisfy the demand for increasing data transmission speed over the past few decades. There are two possible coding schemes to achieve higher speeds like 200/400Gbps: *Non-Return-to-Zero* (NRZ), also known as pulse amplitude modulation 2-level (PAM-2), and Pulse Amplitude Modulation Level-4 (PAM-4). NRZ is an amplitude modulation technique with two voltage levels (hence, PAM-2), representing logic 0 and logic 1 in binary. The term non-return-to-zero points out that in this modulation technique, the voltage does not transition to zero. Instead, a negative voltage represents logic 0, and a positive voltage represents logic 1. On the other hand, PAM-4 is made of four voltage levels, each representing the four combinations of two-bit logics 00, 01, 10, 11 in the binary system, as shown in Figure 15. There are pros and cons to using each of these coding formats.

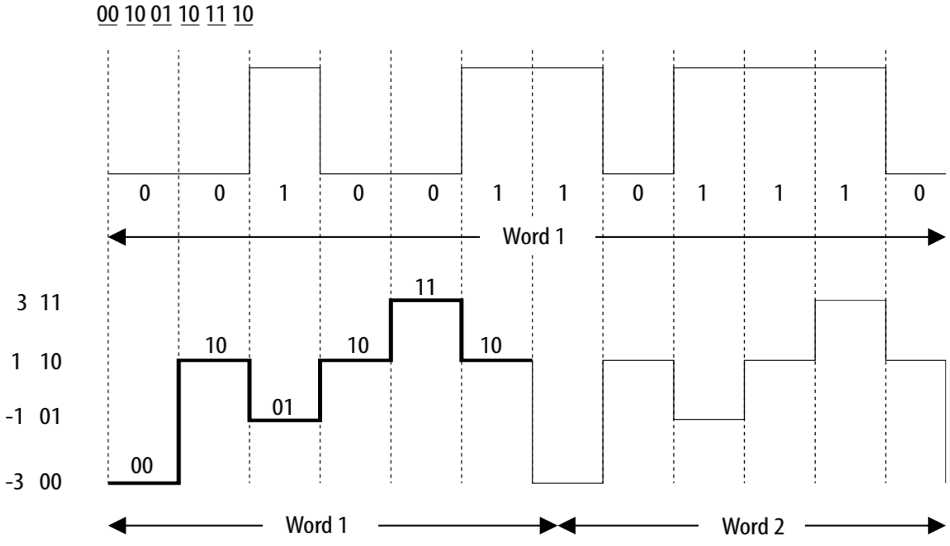

Figure 15. NRZ (PAM-2) (top) and PAM-4 (bottom) coding and voltage levels [25].

As displayed in Figure 15, with NRZ, two bits per clock cycle is achievable, while PAM-4 provides four bits per clock cycle, thereby doubling the bandwidth for a given clock frequency. NRZ, thus, requires a broader bandwidth channel to accommodate for the same data rate. In other words, “PAM-4 has half the Nyquist frequency and twice the throughput for the same Baud rate” [25]. Half Nyquist frequency enables doubling the modulated/transferred data density and higher resolution for PAM-4. However, there are drawbacks to this coding technique. The spacing between different voltage levels in PAM-4 is smaller, making the signal more susceptible to noise. Therefore, signal-to-noise ratio (SNR) for PAM-4 is worse than NRZ.

Four voltage levels in PAM-4 produce 12 signal transitions, as shown in Figure 16, which creates 3 eye-openings as opposed to NRZ with just one eye-opening. This increase in the eye-opening reduces each eye height to 1/3rd of the NRZ eye height from which the SNR loss compared to NRZ can be calculated as in Eq. (2.28).

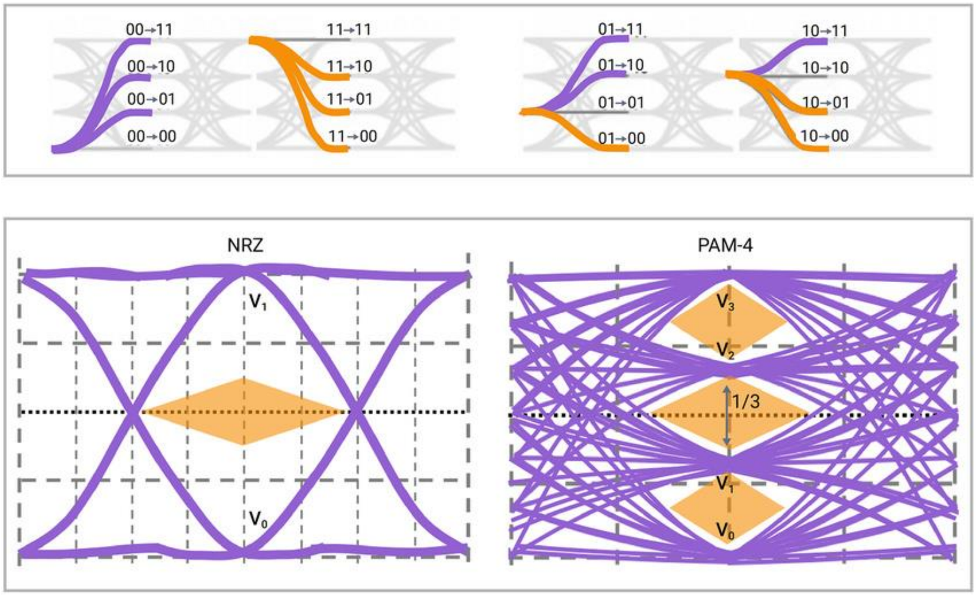

Figure 16. PAM-4 signal transitions (top), NRZ eye-opening (left) and PAM-4 eye-opening (right) [26].

$$SNR\ Loss = 20 \times \log_{10} \frac{1}{3} = 9.5dB \tag{2.28}$$

PAM-4 is also more sensitive to channel impairments and non-linearity. Therefore, a PAM-4 transceiver needs more advanced equalizations, is more complex, expensive, and requires higher power consumption. Hence, when designing the EAM, pros and cons of both modulating formats must be considered based on the EAM's application.

2.7. Floquet-Bloch Theory

Floquet-Bloch theory is a numerically accurate method to analyze wave propagation in periodic (grating) waveguides. This approach is specifically useful for solving deep grating structures or higher order gratings (2^{nd} order and above) due to its accuracy. Considering a mode propagating in a periodic medium, based on Floquet-Bloch theory, the field distribution can be obtained as the sum of all forward and backward waves [27]. Floquet theorem suggests that the field can be mathematically characterized in terms of the phase difference between the propagating fields and is discrete and a multiple of grating wavevector $K = 2\pi/\Lambda$.

Assuming a wave propagating in the +z direction in a periodic waveguide, the field distribution of this propagating wave can be expressed as Eq. 2.30 in terms of Floquet-Bloch analysis.

$$R(x,z) = R(x,z+\Lambda) = \sum_{n=-\infty}^{\infty} \psi_n(x)e^{-jnKz} \tag{2.29}$$

$$\Psi(\mathrm{x},\mathrm{z}) = \mathrm{e}^{-\gamma \mathrm{z}} R(x,z) \tag{2.30}$$

Where $R(x,z)$ is a periodic function in z direction with grating period Λ. $R(x,z)$ can be expanded using Fourier analysis as shown in Eq. 2.31

$$R(x,z) = R(x,z+\Lambda) = \sum_{n=-\infty}^{\infty} \psi_n(x)e^{-jnKz} \tag{2.31}$$

From which, the field distribution propagation can be rewritten as:

$$\Psi(\mathrm{x,z}) = \sum_{n=-\infty}^{\infty} \psi_n(x) e^{-j\gamma_n z} \qquad 2.32$$

Where $K = 2\pi/\Lambda$ is the grating wavenumber, $\gamma_n = \alpha + j\beta$ is the complex propagation constant, α is the attenuation constant and β is the longitudinal propagation constant, respectively, as described earlier in this chapter. The Fourier coefficient $\psi_n(x)$ is called the n_{th} space harmonic. Hence, a wave propagating in a waveguide consists of an infinite number of non-orthogonal space harmonics that all travel with the same group velocity [28]. Therefore, the complex propagation constant of the n_{th} space harmonic is:

$$\gamma_n = (\beta + nK) - j\alpha \qquad 2.33$$

In a first-order grating, $\alpha > 0$ indicates reflection of light whereas for higher order gratings, it could also correspond to modes leaking into the substrate or superstrate [29].

Due to non-orthogonality, an exchange of power might occur between space harmonics. This exchange of power is called *mode coupling*. Interaction between modes can only occur if their propagation constant is related with Eq. 2.34 where p and q are integers corresponding to different guided modes and m is also an integer.

$$\beta_p + \beta_q = mK = m2\pi/\Lambda \qquad 2.34$$

Equation 2.34 is called the *resonant condition*. Mode coupling can be of two types, co-directional and contra-directional. In codirectional coupling the two modes have parallel group velocities and in contra-directional coupling the two wavevectors are in the opposite directions. The field distribution of interacting modes is highly modified near resonant condition. The attenuation constant α in Eq. 2.33 is a measure of the change in the amplitude for these coupled modes. As the waves deviate from resonant condition, their field distribution becomes more similar to when the grating is absent.

Floquet-Bloch method presents a complete solution to the electric and magnetic field distribution in any and all directions whether the light is deflected, transmitted or reflected. This method also gives solutions to both attenuation constant and longitudinal propagation constant, elements of complex propagation constant with a high accuracy. Therefore, Floquet-Bloch method is used in this work to precisely analyze the gratings.

2.8. Bragg Gratings

Gratings, in general, are periodic structures whose periods are comparable to that of optical wavelength. Gratings in optical waveguides are optical components used in optical integrated circuits as reflectors, mirrors and couplers. When light propagates through a medium and encounters a series of equally spaced perturbations, that medium serves as a Bragg grating. Periodic variation of the refractive index of the medium by using alternating material or a periodic boundary is used to create the Bragg gratings. Bragg gratings are used as mirrors for lasers in order to achieve single frequency operation and filter out the unwanted spectrum [30] or as out-couplers to couple out the light.

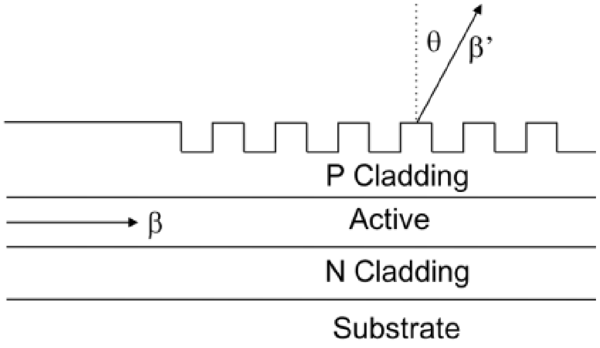

Figure 17. Schematic drawing of a waveguide structure with a grating etched on the top showing the light deflected at angle θ [29].

The angle that the out-coupled light makes with the normal, θ can be found from 2.35.

$$\sin^2\theta = \mathrm{n}_{\mathrm{eff}}^2 - 2\mathrm{n}_{\mathrm{eff}}\left(\frac{\lambda_0}{\Lambda}\right) + \left(\frac{\lambda_0}{\Lambda^2}\right) \qquad 2.35$$

When a beam of light (or any kind of wave) encounters an obstacle or opening or a periodic media, diffraction happens. A periodic media is one whose dielectric constant alternates between two values (indicating alternating materials) or in general is a periodic function of position (z) as described here:

$$\epsilon(x) = \epsilon(z+a), \quad \mu(x) = \mu(z+a) \qquad (2.36)$$

Consider the periodic medium in Figure 18 where Λ is the grating period (the spacing between the alternating material or periodic structure). Assuming the incident light is composed of parallel plane waves with identical wave vectors k, that are separated by Λ, the path difference the rays have to go through can be found from simple trigonometry to be $2\Lambda\sin\theta$ as shown in Figure 18 where θ is the angle of the incident beam with respect to the periodic medium's boundary.

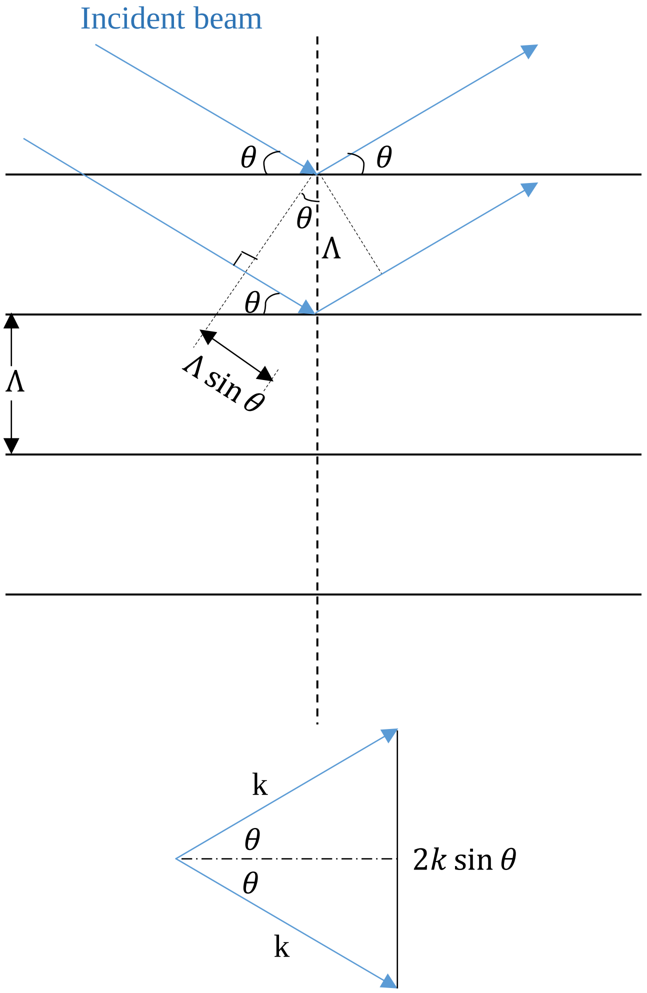

Figure 18 Scattering of monochromatic wave from a periodic medium

The interference between two rays could either be destructive or constructive. In case of constructive interference, the path difference between the two rays has to be an integer multiple of the incident light's wavelength in the medium, λ, as depicted in (2.37):

$$2\Lambda \sin\theta = m\lambda, \quad m = 1,2,3,\ldots \tag{2.37}$$

Equation (2.37) is called Bragg's law. Note that θ, the incident angle, can take any value, but in order for beam diffraction to happen, θ should be selected in a way that obeys Bragg's law. From the definition of wavevector $k = 2\pi/\lambda$ by replacing $\lambda = 2\pi/k$ and rearranging (2.37) a different form of Bragg's law is revealed, as described below:

$$2k \sin\theta = m\left(\frac{2\pi}{\Lambda}\right), \quad m = 1,2,3,\ldots \tag{2.38}$$

As explained in the bottom part of Figure 18, the left side of Eq. (2.38) is the change wavevector goes through when it is diffracted from the periodic medium. Therefore, in a way, Bragg's law can be interpreted as the conservation of momentum for a wave incident to the medium [31], [32].

Simplifying and rearranging Eq. (2.37) to find the Bragg angle produces the following:

$$\theta = \sin^{-1}\left(\frac{m\lambda}{2\Lambda}\right), \quad m = 1,2,3,.. \tag{2.39}$$

Where m is the diffraction order. Maximizing the reflected power would ideally set $\theta = 90°$, which leads to the first-order ($m = 1$) and second-order ($m = 2$) Bragg conditions as follows:

$$\theta = \sin^{-1}\left(\frac{\lambda}{2\Lambda}\right) = 0 \rightarrow \Lambda_{1st} = \lambda/2 \tag{2.40}$$

The second Bragg condition is as follows:

$$\theta = \sin^{-1}\left(\frac{\lambda}{\Lambda}\right) = 0 \rightarrow \Lambda_{2nd} = \lambda \tag{2.41}$$

Therefore, when designing a grating, choosing the grating period to be equal to $\lambda/2$ or λ guarantees the first or second Bragg condition to be met. To clarify, the notations used here are $\lambda = \lambda_0/n_{eff}$ for the wavelength of the light inside the media where λ_0 is the light wavelength in the air and n_{eff} is the effective index of the medium.

2.8.1. First-order Feedback Grating

The modes traveling through a grating waveguide can couple with each other either contra-directionally or co-directionally. A forward traveling mode, p, and a backward traveling mode, q, (or reflected/perturbed mode since solving for grating structures) can couple into each other. Since they travel in the opposite direction, this is a contra-directional coupling. The coupling coefficient, κ_{pq}, between these two modes can be found from Eq. below [18], [29]:

$$\kappa_{pq} = \frac{\omega\epsilon_0}{4} b_m(n_1^2 - n_2^2). \int_{-t_g}^{0} E_p^*(x)E_q(x)dx \qquad 2.42$$

Where ω is the angular frequency, ϵ_0 is the free space permittivity, b_m is the Furrier coefficient for the grating order, n_1 and n_2 are the refractive indices of the core and cladding, respectively, t_g is the grating depth, and E_p and E_q are the field associated with p and q modes, respectively.

There are two variable terms in this formula that dictate coupling coefficient. The term $(n_1^2 - n_2^2)$, the relative permittivity difference between the grating layer and the cladding layer is one of the terms to tweak to maximize coupling coefficient [33]. For this, choosing the suitable material for each layer is crucial since relative permittivity is native to the material. The second variable, the term inside the integral, describes the fraction of light that is confined to the grating region. Increasing the optical mode overlap increases the coupling strength. Therefore, increasing the light confinement inside the grating region is another key to have an effective grating coupler [34], [35].

Application of first-order gratings include in-plane reflection and transmission of light within waveguides. From the Coupled Mode Theory, reflected and transmitted power of a first-order grating with a length of L are as follows [31], [34].

$$R = \frac{|\kappa L|^2}{(\Delta\beta L/2)^2 + (sL)^2 \coth^2(sL)} \qquad 2.43$$

$$T = \frac{\gamma}{\gamma \cosh(\gamma L) - (\alpha - j\Delta\beta)\sinh(\gamma L)} \qquad 2.44$$

Where parameters s, γ and $\Delta\beta$ can be found from

$$\mathrm{s} = \left[|\kappa|^2 - \left(\frac{\Delta\beta}{2}\right)^2\right]^{1/2} \qquad 2.45$$

$$\gamma = [\chi^2 + (\alpha - j\Delta\beta)^2]^{1/2} \qquad 2.46$$

$$\Delta\beta = 2(\beta - \beta_0) \qquad 2.47$$

Although coupled mode theory provides an adequate solution to the first-order gratings, it is not precise enough to solve for higher order or deep gratings. This method along with Floquet-Bloch is used in [36] to analyze a first-order ECS grating.

2.8.2. Second-order Grating Out-couplers

Out-couplers are grating structures used to couple the light out of the waveguide plane in form of an external wave rather than in-plane coupling. Second-order grating out-couplers partially reflect the light and partially couple the light upwards (as shown in Figure 17) or downwards. The light coupled upwards can be combined with the downwards coupled light using a reflective coating. Therefore, the total out-coupled power can be found by adding the upwards and downwards light. If the wavelength is selected in a way that the substrate is transparent to it, the downwards out-coupled power can pass through and couple into another component or out of the device [37].

It is mathematically proved in [38] that second-order gratings can be used whether as out-couplers or as reflectors in optical waveguide devices. Mathematical calculations shows that the attenuation is zero at the exact second Bragg condition. The normalized attenuation constant for a second order grating nearly approaches zero at the exact second Bragg condition as shown in Figure 19 for every mode present.

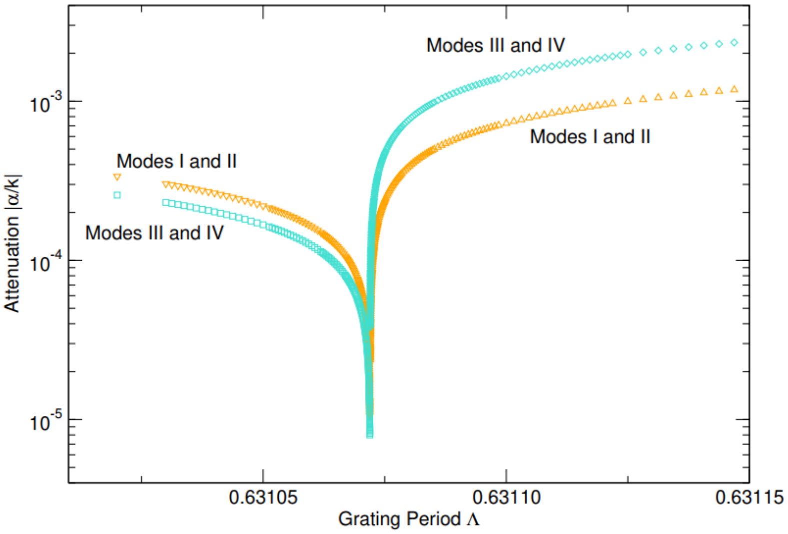

Figure 19. Absolute value of normalized attenuation constant as a function of grating period (y-axis is in log scale) [38].

This proves that for a lossless optical waveguide, two pairs of modes exist at the wavelength around second Bragg condition, each pair having identical attenuation constant. At second Bragg condition, the diffracted beams have shared the same period as the longitudinal propagation constant β which results in out-coupled beams to be nearly perpendicular to the direction of the waveguide.

Chapter 3

GENERIC SECOND-ORDER ECS OUT-COUPLER GRATINGS

3.1. Enhanced Coupling Strength Grating Structure With, and Without Liner

The concept of enhanced coupling strength grating structure or ECS structure was first introduced in [39]. This concept was initially developed in an attempt to achieve very short, efficient grating out-couplers in III-V waveguides after the demonstration of 80% efficient grating out-couplers in silicon photonic waveguides for ∼10 micrometer long gratings [40]. These grating couplers allow short, high-efficiency horizontal cavity lasers to be tested at the wafer-level and allow such surface-emitting lasers to share a common waveguide with other optical components such as modulators which makes it ideal for the proposed transceiver device. Further, these are CMOS compatible and can be fabricated using current process flows, decreasing production cost [41].

However, conventional III-V gratings used for distributed feedback (DFB) and distributed Bragg reflectors (DBR) or out-couplers typically require hundreds of micrometers in length to achieve efficiencies as high as grating couplers on Silicon on Isolator (SoI) [17], [42]. This paper addresses the use of ECS gratings for outcoupling power from III-V waveguides. Figure 20 shows the normalized modal profile for (a) Silicon photonic waveguide (b) conventional DFB grating, (c) conventional DBR out-coupler waveguide, (d) ECS with liner (ECSL) out-coupler waveguide, and (e) ECS non-liner (ECSNL) out-coupler waveguide. Each waveguide has the same core thickness (0.3 micrometers), same core index (3.5) and same grating depth.

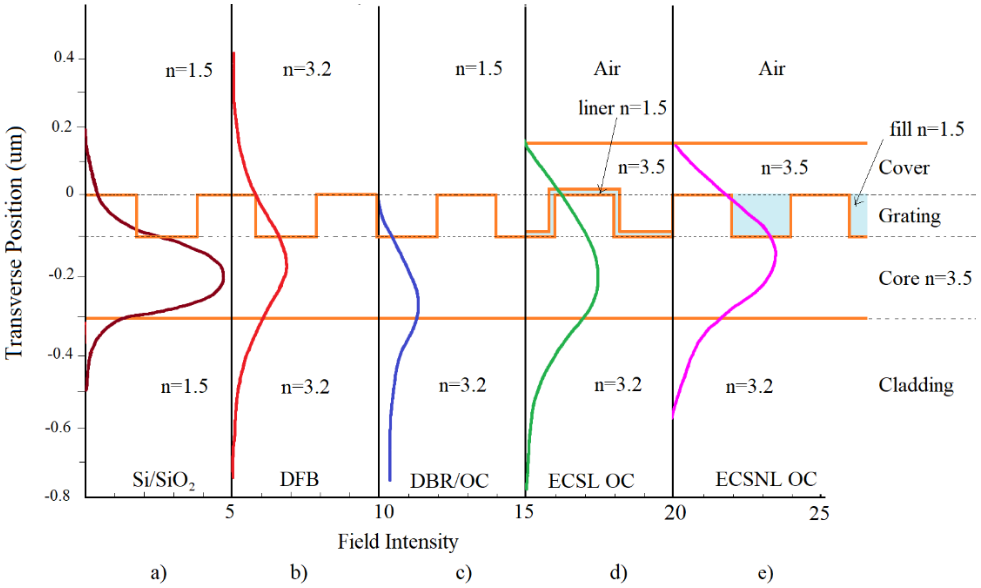

Figure 20. Calculated normalized intensity modal profiles for (a) Silicon photonic waveguide (b) DFB grating, (c) conventional DBR out-coupler waveguide, (d) ECS with liner out-coupler waveguide, and (e) ECS non-liner out-coupler waveguide. Each waveguide has the same core thickness (0.3 micrometers), same core index (3.5) and same grating depth [43].

This concept deploys a low index liner thickness to increase the refractive index difference at the grating boundary resulting in increasing the confinement factor and keeping the mode confined inside the waveguide. A high index cover layer was used on top of the grating layer to pull the mode up into the grating layer, as shown in Figure 20 (e) and (d) [44], [45]. Starting from this idea, proposed here are two new structures that deploy both schemes to aim for a high out-coupling grating structure, as shown in Figure 21.

One has a low index thin layer on top of the grating (liner layer) with a high index cover layer filling in the grooves and acting as a cover layer on top. This structure is called *Enhance Coupling Strength Liner* (ECSL) as shown in Figure 21 (a). The other has its grooves filled with a low index material with the same high index cover layer on top and is called *Enhanced Coupling Strength Non-Liner* (ECSNL), shown in Figure 21 (b). ECSL structure is deploying a thin film layer of low index material such as a spin-on-glass with an index of ~1.5. The cover layer of a high index material could be amorphous silicon with an index of ~3.5 deposited on top to pull the mode into the grating region.

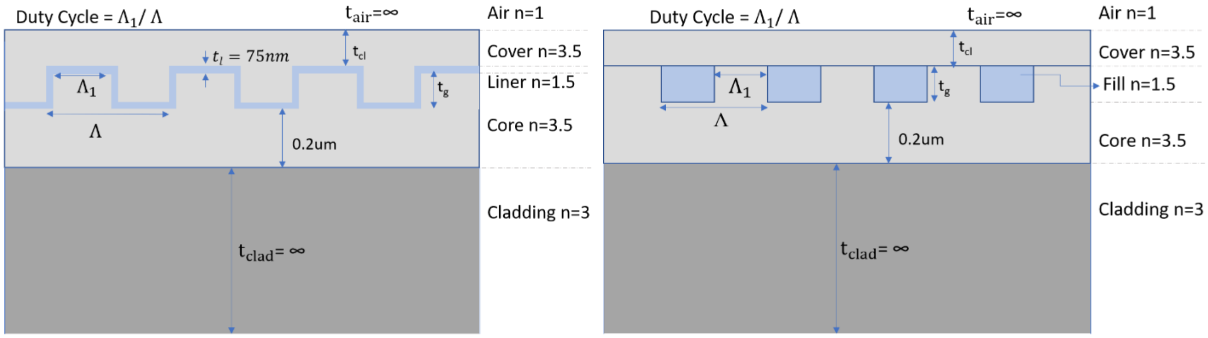

a) b)

Figure 21. Schematic structure of the enhanced coupling strength grating with (a) liner layer (ECSL) and (b) non-liner layer (ECSNL).

Figure 22 is a plot of the real and imaginary normalized complex effective indices β/k_0, and α/k_0 as a function of wavelength for different cover layer thicknesses for the ECSL and ECSNL structures for a duty cycle of 50%, grating depth of 0.1 µm, and an ECSL liner thickness of 75 nm. The solid light blue line in Figure 22 (b) corresponding to a cover layer thickness of zero has properties nearly the same as a conventional DBR grating since the grooves are filled with a low index material close to that of air.

In Figure 22 (a) and (b), attenuation approaches zero at the exact second Bragg condition at a wavelength of $\lambda{\sim}1.55\mu m$. The α/k_0 plots for ECSL and ECSNL in Figure 22 (a) and (b) show a 3 to 4 times improvement compared to the traditional DBR (the blue solid line in Figure 22 (b)).

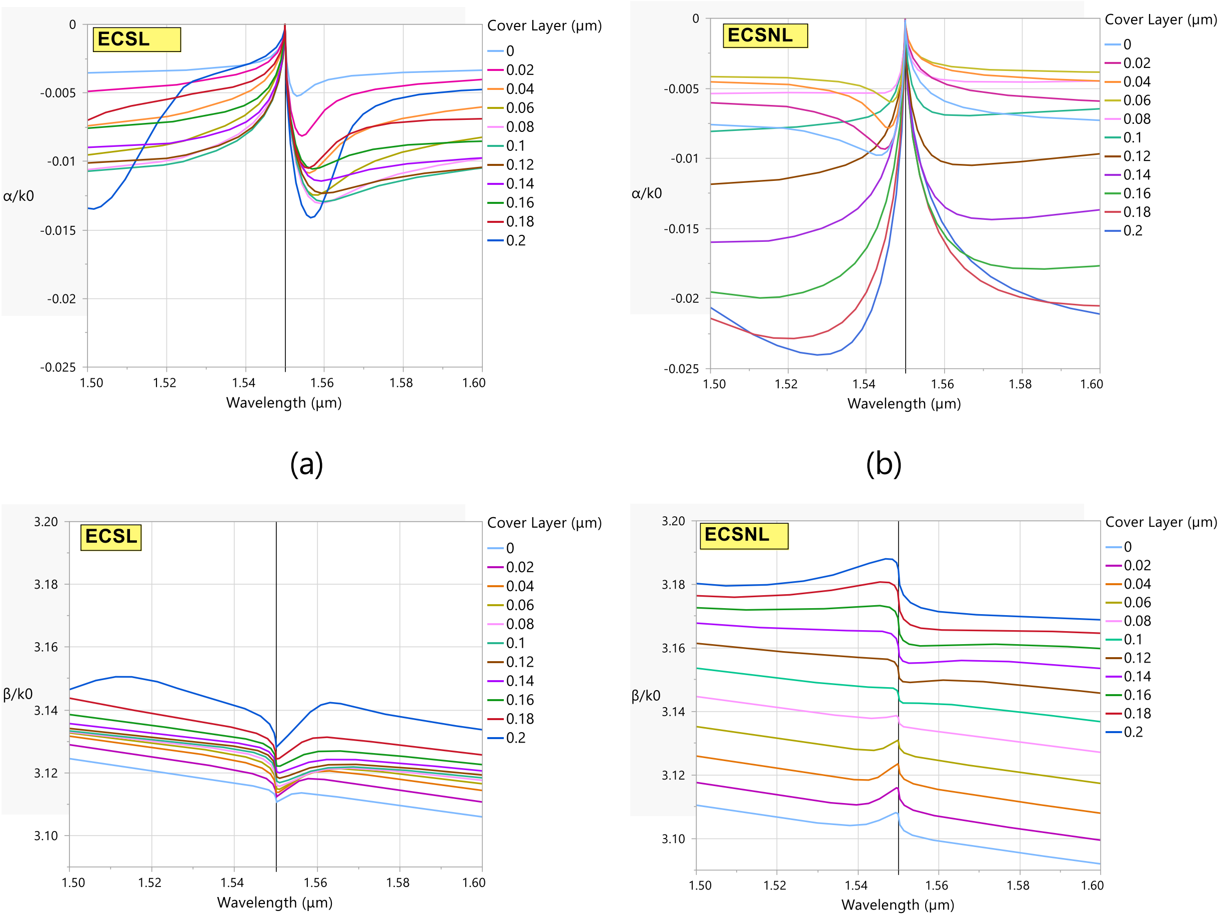

(a) (b)

(c) (d)

Figure 22. α/k_0 as a function of wavelength for different cover layers for (a) ECSL and (b) ECSNL and β/k_0 as a function of wavelength for (c) ECSL and (d) ECSNL for a fixed duty cycle of 50%. The liner thickness for the ECSL structure is $t_l = 75nm$.

The imaginary part of effective index (α/k_0) which is an indication of attenuation in the waveguide shown in Figure 22 (a) and (b) shows that both ECSL and ECSNL structures have significantly lower attenuation compared to the conventional DBR case shown in same graph with solid light blue line. Then a comparison between the attenuation constant of ECSL and ECNL structure illustrates that ECSNL in general has significantly lower attenuation compared to ECSL. In the next section, exploring the parameter space for the two structures is proposed. There are various parameters in this design that can be manipulated in order to maximize the out-coupled power near a certain operating wavelength including the liner thickness (t_l), grating duty cycle ($DC = \Lambda_1/\Lambda$), cover layer thickness (t_{cl}) and grating depth (t_g) [46].

3.2. Exploring Parameter Space for Generic 2nd Order Grating Out-couplers

Parameters shown in Figure 21 can be manipulated to achieve certain goals in designing the grating structure. The focus in this section is to design a structure that realizes high out-coupling and low reflectivity. Indices of refraction and thicknesses of each layer are indicated in Figure 21.

3.2.1. Liner Thickness

Before exploring other parameters, it is important to find the best liner thickness for the ECSL structure. The goal is to design a short, high efficiency out-coupler; therefore, simulations are done only for 10, 20 and 50μm long grating structures. Furthermore, the grating is designed to operate around a central frequency of 1.55μm therefore all simulations presented here include $1.55 \mp 0.05\mu m$.

Figure 23 shows the out-coupled power as a function of wavelength, when varying the liner thickness (t_l) for grating lengths 10µm, 20µm and 50µm. Increasing the liner thickness results in an increase in the out-coupled power regardless of the grating length. However, the numerical method used to calculate the power is susceptible to a larger error when increasing the grating length greater than 20µm. This issue will be fixed in future versions of the software.

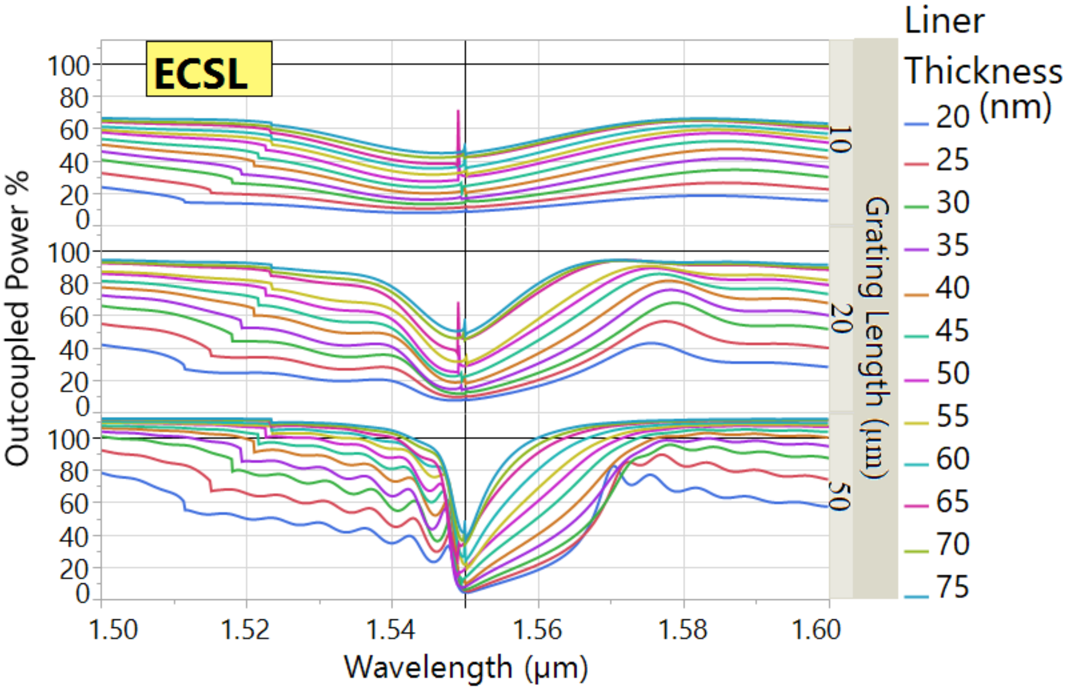

Figure 23. Out-coupled power as a function of wavelength varying liner thickness for ECSL at 50% duty cycle for different grating lengths.

For a 10µm long grating adding a 75nm liner layer on top of the grating results in a 178% increase in the maximum outcoupled power. Comparing the curves for different liner thicknesses one can observe that the out-coupled power increases by increasing the liner thickness. Therefore, the optimum liner thickness for the ECSL structure is 75nm as shown in Figure 23.

3.2.2. Duty Cycle

Shown in Figure 21, duty cycle is defined as the ratio between the length of the tooth, Λ_1, to the length of one cycle of grating (i.e., tooth plus the groove) or grating period, Λ as follows.

$$DC = \frac{\Lambda_1}{\Lambda} \tag{3.1}$$

Figure 24 shows the normalized attenuation constant and longitudinal propagation constant for different cover layers and different duty cycles. Due to the structural limitation in ECSL case, the duty cycle can only be swept from 5% to 55%. Any duty cycle bigger than 55% would fill the entire grooves and turn the ECSL structure into something very similar to ECSNL structure.

Increasing the cover layer thickness results in lower attenuation and higher propagation constants in both structures. Comparing the normalized attenuation and propagation constants in the two structures shows that ECSNL structure has lower attenuation peaks and generally higher propagation constants compared to ECSL structure. This makes ECSNL structure more suitable to be used as an outcoupler.

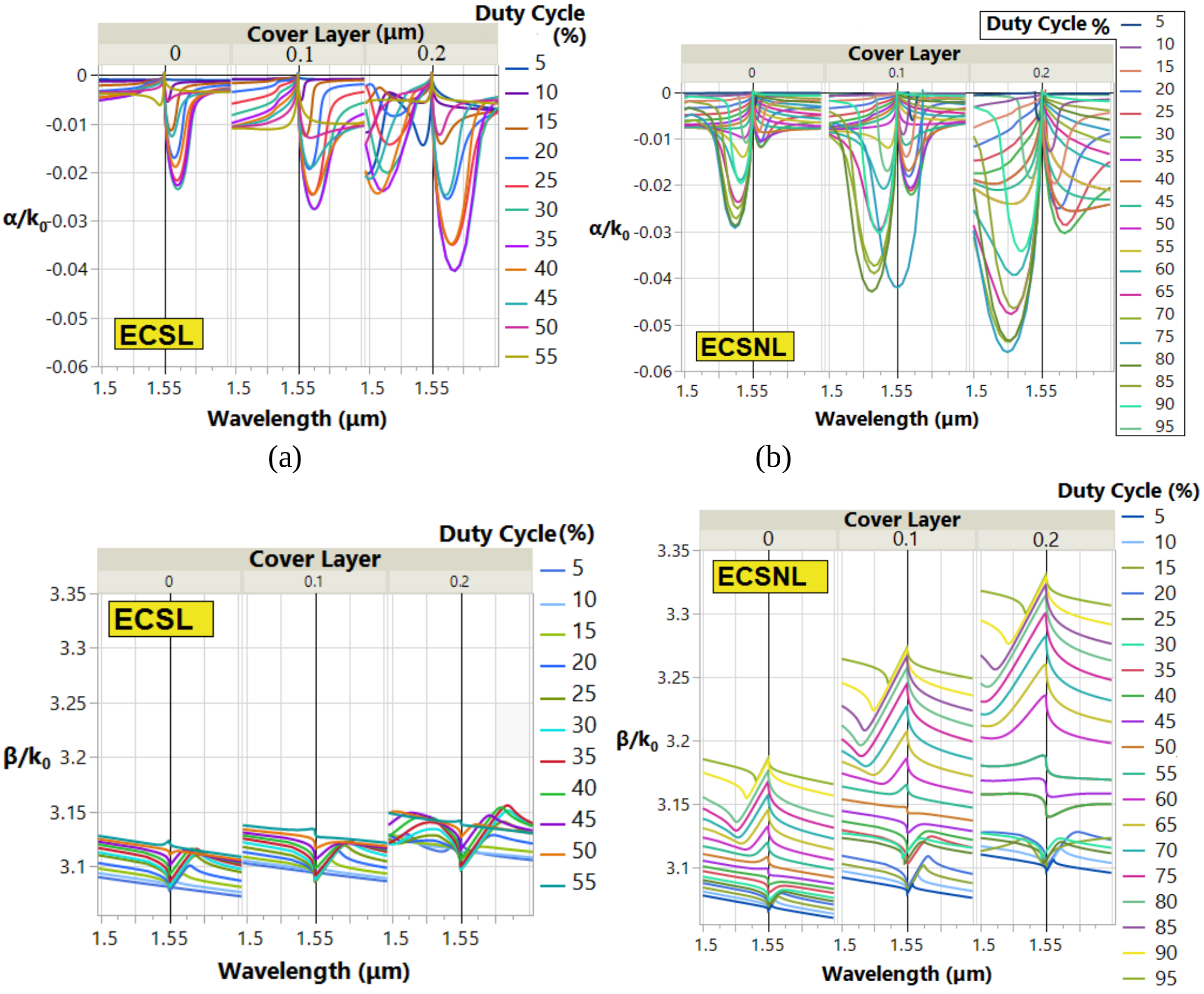

(a) (b)

(c) (d)

Figure 24. α/k_0 as a function of wavelength for (a) ECSL and (b) ECSNL and β/k as a function of wavelength for (c) ECSL and (d) ECSNL for different duty cycles for 0, 0.1, 0.2 µm cover layer

On the other hand, increasing the duty cycle does not necessarily result in an increase in the propagation constant. For ECSL structure, the attenuation constant decreases when increasing the duty cycle up to 35% from which onwards it starts going up. The propagation constant for ECSL follows a similar trend, it increases up until 35% duty cycle and then drops down from 35% to 55% duty cycle. Therefore, the optimum duty cycle for ECSL is 35%. For ECSNL structure, maximum propagation constant and minimum attenuation constant both occur at 50% duty cycle.

Figure 25 shows the total outcoupled power (up and down) for (a) ECSL structure (with 75nm liner) and (b) ECSNL structure for various duty cycles and grating lengths. In Figure 25 (b) the ECSNL case, a cover layer thickness of zero is essentially equivalent to a conventional grating structure. For cover layers of $0.1\mu m$ and $0.2\mu m$, the outcoupled power is significantly higher (2x and 3x) for both ECSL and ECSNL structures compared to the conventional grating structure. The outcoupled power follows the same trend as the normalized complex effective index shown in Figure 24 does, once again suggesting 35% DC and 50% DC as the optimized duty cycles for ECSL and ECSNL structures, respectively.

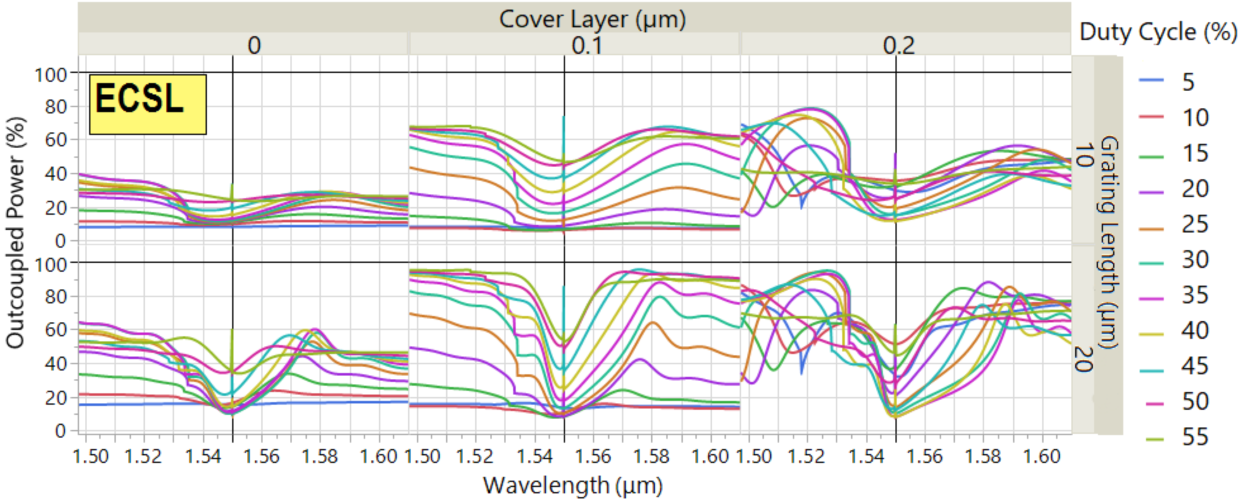

(a)

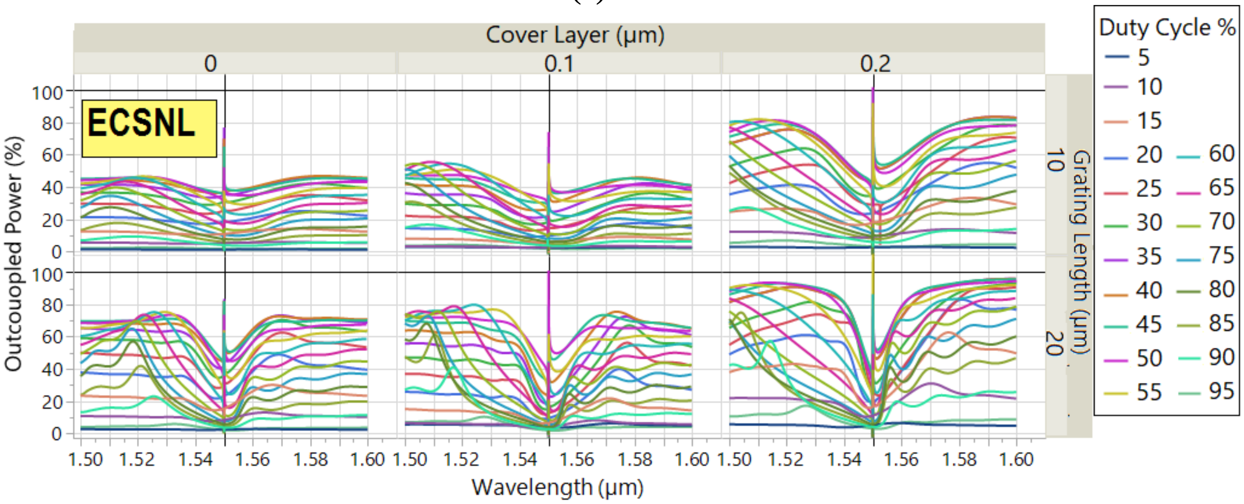

(b)

Figure 25. Outcoupled power as a function of wavelength when varying duty cycle for different lengths and cover layers for (a) ECSL and (b) ECSNL

Figure 26 shows a complete analysis of the maximum out-coupled power (solid lines) and reflected power (dashed lines) as a function of wavelength when considering different varieties of cover layers, grating length and ECS structures. Note that in case of ECSL structure, due to the geometry of the structure and presence of the liner layer, the duty cycle cannot pass 55% or else the grooves will be fully filled. Based on Figure 26, for ECSNL structure maximum out-coupling occurs at 50% duty cycle while the reflectivity is at its lowest at the same time. For ECSL, both out-coupling and reflectivity follow the same trend.

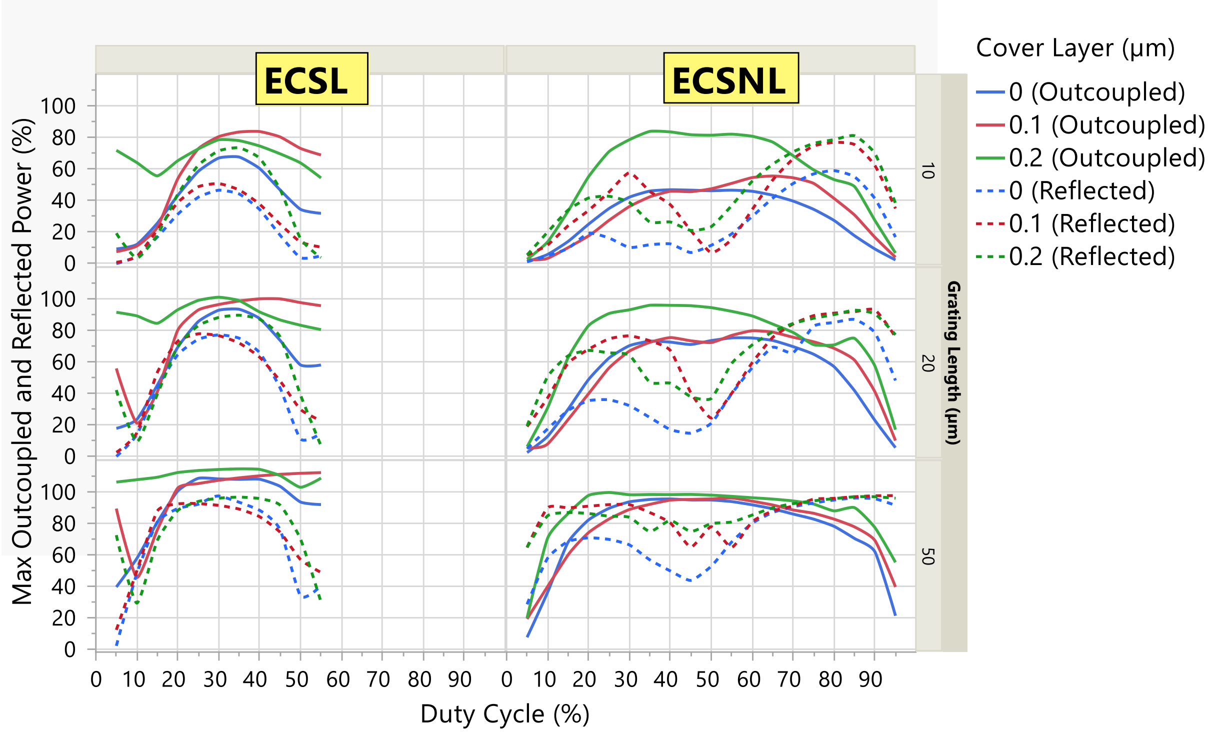

Figure 26. Maximum out-coupled power (solid lines) and reflected power (dashed lines) as a function of duty cycle for different grating lengths for different cover layer thicknesses for ECSL and ECSNL

3.2.3. Cover Layer Thickness

Effect of adding a high index cover layer for both ECSL and ECSNL structures is investigated in this section to compare with conventional grating structure and to find out the optimum cover layer thickness for each structure that enables highest out-coupling. Figure 27 shows the outcoupled power as a function of grating length for 10μm and 20μm long gratings with 50% duty cycle for ECSL and ECSNL structures. Cover layer of 0.18μm results in maximum outcoupled power in both cases. Figure 27 (b) where cover layer is zero is identical to a conventional grating and has the least outcoupled power compared to the curves corresponding to cover layers bigger than 0. In Figure 27 (a) for a 10µm long ECSL grating, outcoupled power is ~3 times larger than that of a conventional grating, increasing the outcoupling from 20% to 65%. In Figure 27 (b) for a 10µm long ECSNL grating, adding the cover layer results in ~4 times larger outcoupling increasing it from 20% to 80%.

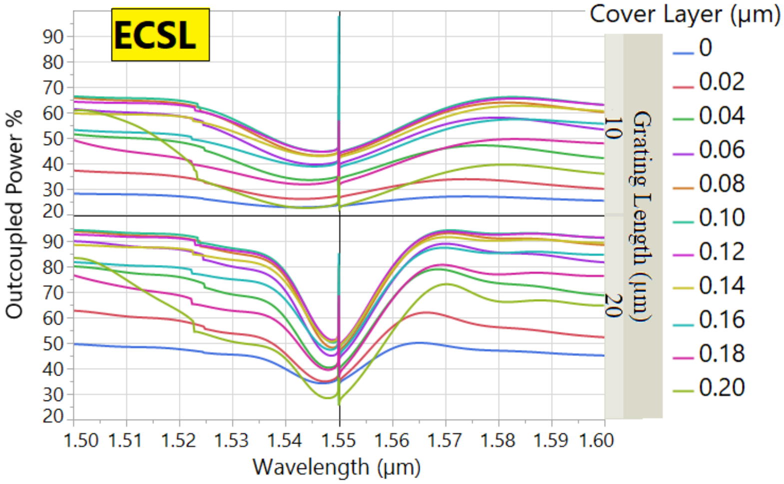

a)

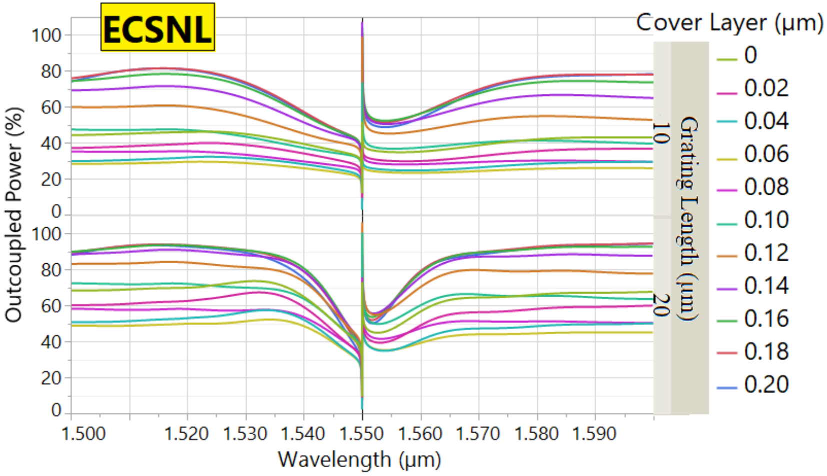

b)

Figure 27. Outcoupled power as a function of wavelength varying cover layer thickness for 10µm and 20µm long gratings with 50% duty cycle for (a) ECSL and (b) ECSNL structure.

Figure 28 is a plot of the maximum outcoupled power as a function of the thickness of the cover layer for both ECSL and ECSNL structures. The horizontal dashed lines show the out-coupled power of a conventional grating structure with same grating lengths. A cover layer of $0.08\mu m$ in the ECSL structure increases the maximum out-coupled power by 55% for a $10\mu m$ long grating. For the ECSNL case, a cover layer of 0.18 μm provides an increase of 88% in the out-coupling for a $10\mu m$ long grating. When increasing the grating length to $20\mu m$, a cover layer of $0.08\mu m$ for ECSL structure results in 34% increase in the outcoupled power and a cover layer of $0.18\mu m$ for ECSNL results in 30% increase in the outcoupled power compared to a conventional grating with the same length and layer compositions. Increasing the grating length beyond 50 microns results in decreasing performance improvement over conventional gratings. In the remaining figures, we only consider grating lengths up to 20 μm.

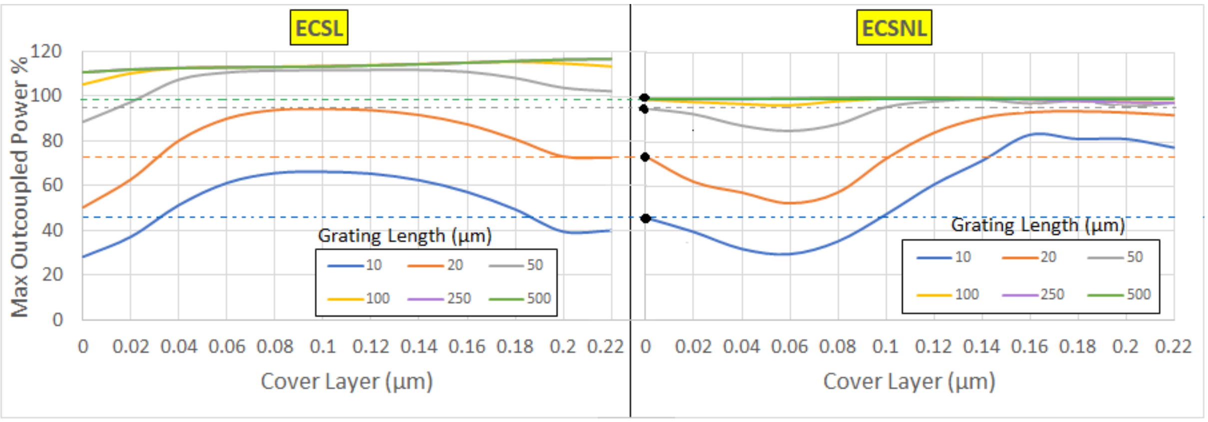

a) b)

Figure 28. Maximum Outcoupling as a function of cover layer thickness for 10-500µm grating length for 50% duty cycle for ECSL with 75nm liner thickness and ECSNL. Dashed lines indicate conventional gratings with same structure as ECSL and ECSNL with lengths color coded as indicated in legends.

3.2.4. Optimum Design for Generic ECS Gratings

Exploring the design variables for the two structures compared to conventional DBR structure leads to an optimum design for each that is presented in this section. Figure 29 shows the power distribution for a 10μm long grating as a function of wavelength for (a) traditional DBR, (b) ECSL with 75nm liner thickness and 0.1μm cover layer and (c) ECSNL with 0.18μm cover layer. The cover layer thickness and the liner thickness are selected to be at their optimum case producing best results for each case based on discussions in previous section.

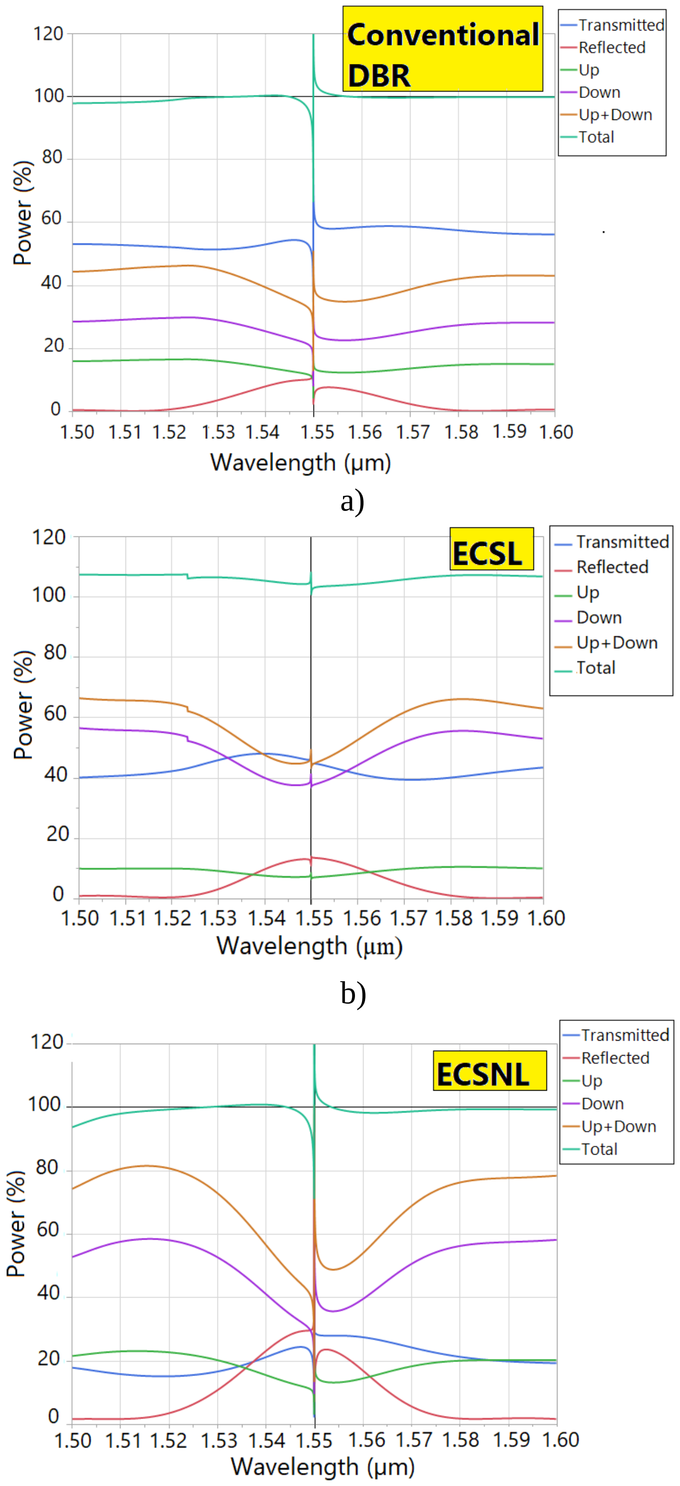

a)

b)

c)

Figure 29. Power distribution for a 10μm long grating as a function of wavelength for (a) conventional DBR, (b) ECSL with 0.1μm cover layer for 75nm liner thickness, and (c) ECSNL with 0.18μm cover layer

Figure 29 shows that ECSNL case produces the highest ratio of light coupled out of the waveguide which is ideal when designing an out-coupler. ECSL structure still shows advantages over the conventional grating by increasing the out-coupling from 45% to over 68%. Figure 29 (c) shows a maximum outcoupled power of 82% as opposed to 45% outcoupling that conventional gratings provide.

By introducing a low index liner layer and by filling the grooves of a traditional DBR as well as putting a high index cover layer on top, the conventional grating was improved to be used as an out-coupler by 51% and 82% for ECSL and ECSNL, respectively.

Figure 30 shows the field distribution in the grating region for the ECSL structure with $0.2\mu m$ cover layer thickness and a $0.75nm$ liner thickness.

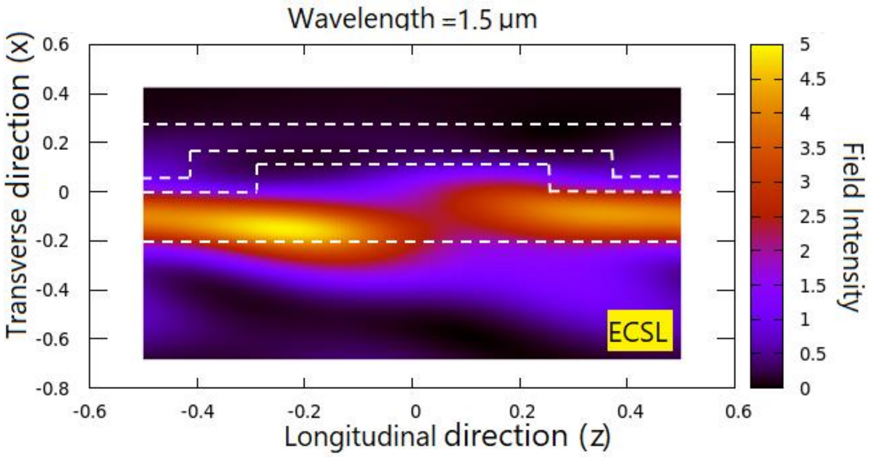
Wavelength =1.5 µm
Transverse direction (x)
0.6
0.4
0.2
0
-0.2
-0.4
-0.6
-0.8
Longitudinal direction (z)
-0.6
-0.4
-0.2
0
0.2
0.4
0.6
ECSL
Field Intensity
5
4.5
4
3.5
3
2.5
2
1.5
1
0.5
0

a)

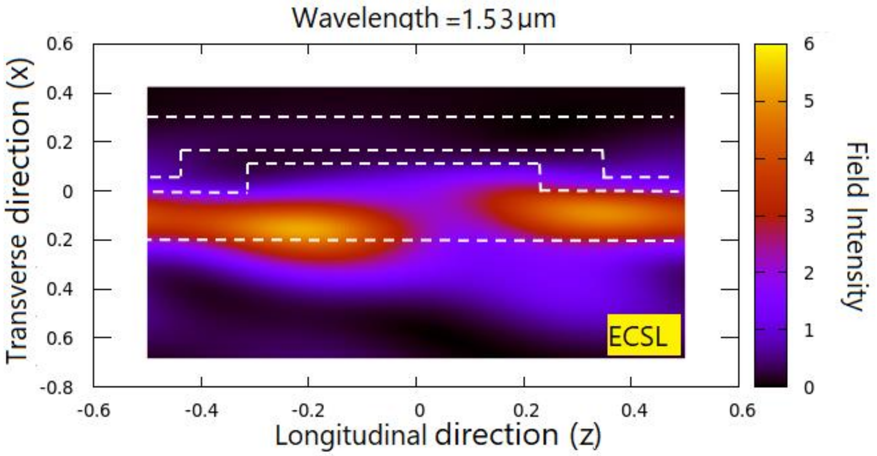
Wavelength =1.53 µm
Transverse direction (x)
0.6
0.4
0.2
0
0.2
0.4
0.6
-0.8
Longitudinal direction (z)
-0.6
-0.4
-0.2
0
0.2
0.4
0.6
ECSL
Field Intensity
6
5
4
3
2
1
0

b)

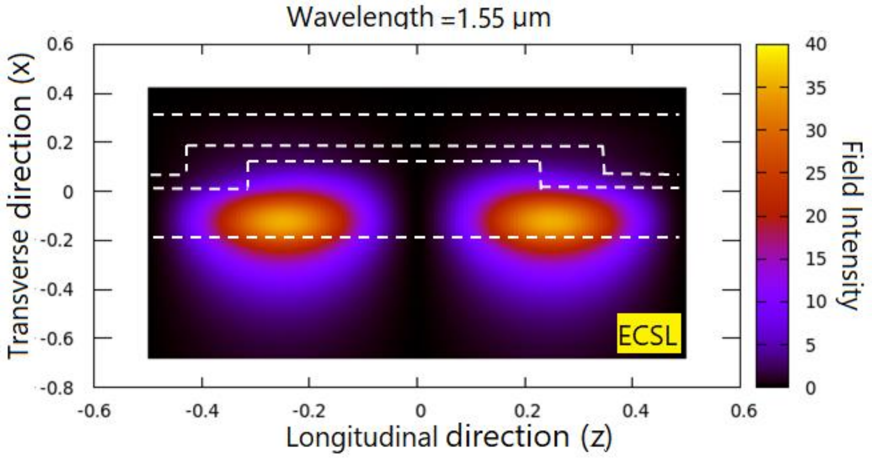
Wavelength =1.55 µm
Transverse direction (x)
0.6
0.4
0.2
0
-0.2
-0.4
-0.6
-0.8
Longitudinal direction (z)
-0.6
-0.4
-0.2
0
0.2
0.4
0.6
ECSL
Field Intensity
40
35
30
25
20
15
10
5
0

c)

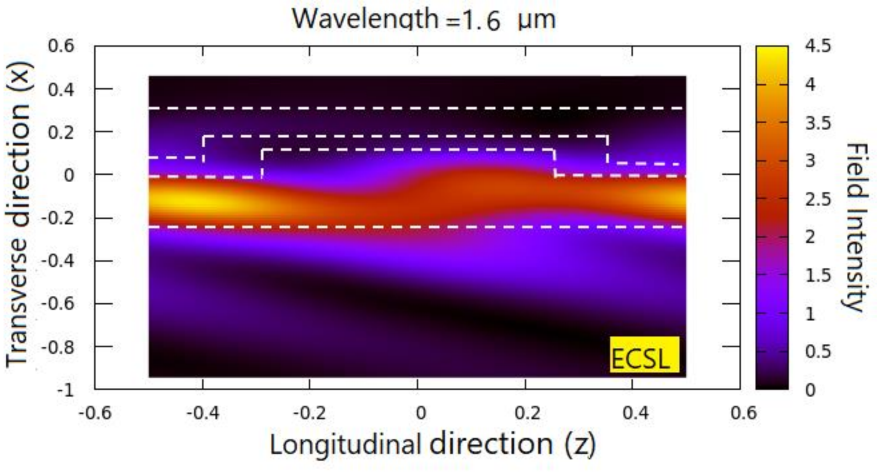

d)

Figure 30 Field intensity distribution in the grating region for ECSL structure with 0.2μm cover layer and 75nm liner thickness at wavelengths a) 1.5μm, b) 1.53µm c) 1.55µm and d) 1.6µm.

Figure 31 shows the field intensity for the ECSNL structure at (a) wavelengths 1.5µm where radiated power is 74% and reflected power is 2%, (b) wavelengths 1.53µm where radiated power is80% and reflected power is 5%, (c) wavelengths 1.55µm where radiated power is 65% and reflected power is 30% and (d) wavelength 1.6µm where radiated power is 79% and reflected power is 2%.

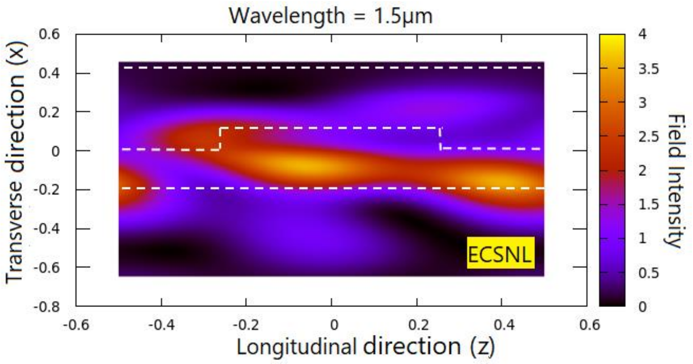

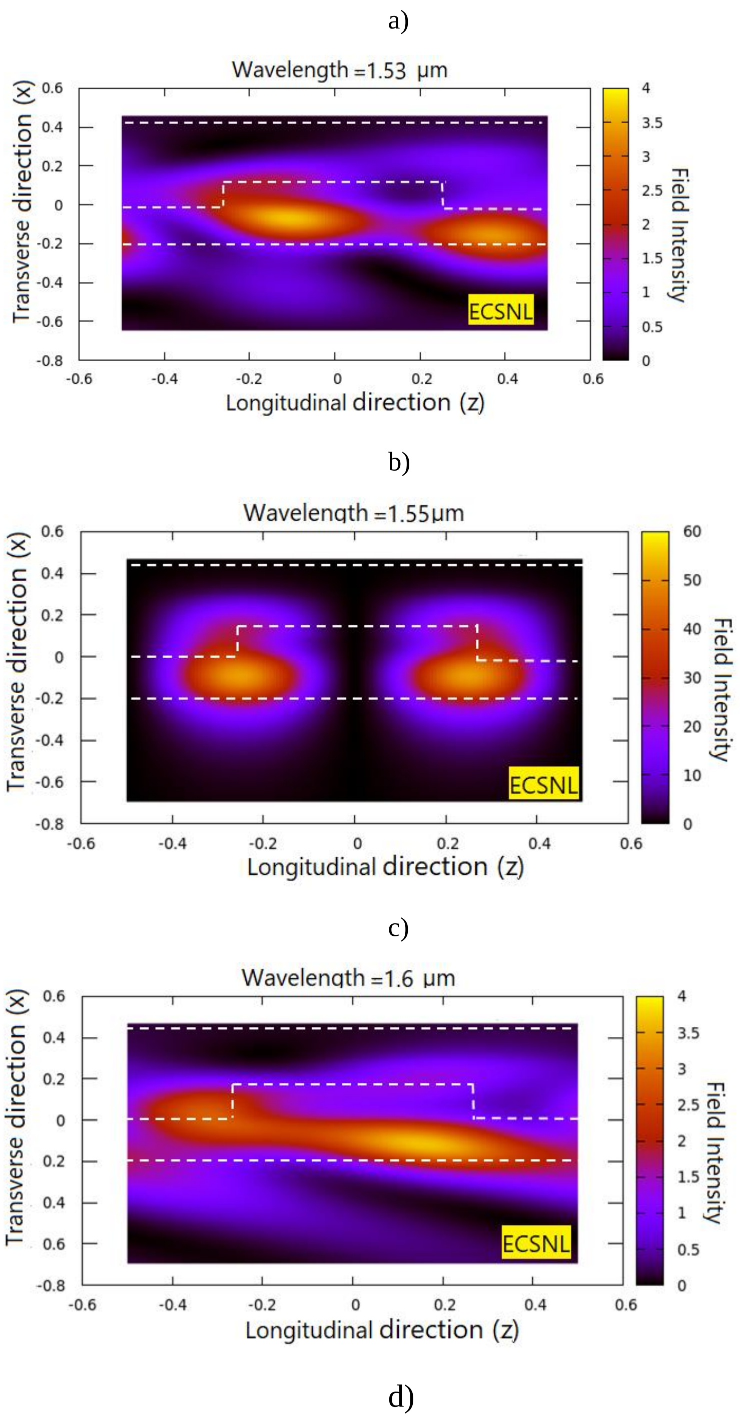

Figure 31. Field intensity distribution in transverse z and longitudinal x direction for ECSNL structure with 0.2um cover layer, 50% duty cycle and 0.4952µm grating period at wavelengths a) 1.5µm, b) 1.53µm c) 1.55µm and d) 1.60µm

3.3. Reflective Properties of Second-Order ECSL and ECSNL Gratings

Although first-order gratings are the most efficient in-plane reflectors, limitations on holography and conventional lithography are among reasons to consider the reflective properties of second- and higher-order gratings. Second-order gratings can be designed to maximize in-plane reflections and minimize outcoupled power [27].

Figure 32 shows the reflected power as a function of wavelength when varying the duty cycle for different cover layer thicknesses for (a) an ECSL structure and (b) an ECSNL structure. For many cases the maximum reflected power occurs away from the second Bragg wavelength of $1.55\mu m$. From left to right, cover layer increases which results in a larger reflected power over a wider range of spectrum both for ECSL and ECSNL. On the other hand, focusing on each of the graphs separately makes it apparent that increasing duty cycle does not necessarily increase the spectral width, rather for ECSNL it peaks around 85% and decreases again as duty cycle increases. For ECSL, reflected power reaches its maximum at 35% duty cycle.

Comparing the graphs for ECSL and ECSNL shows that ECSNL structure proposes a wider spectral width or higher reflectivity over a wider range of wavelengths which makes it a better candidate than ECSL when designing a DBR mirror that has to be integrated in a circuit with active components that have variable operating frequencies.

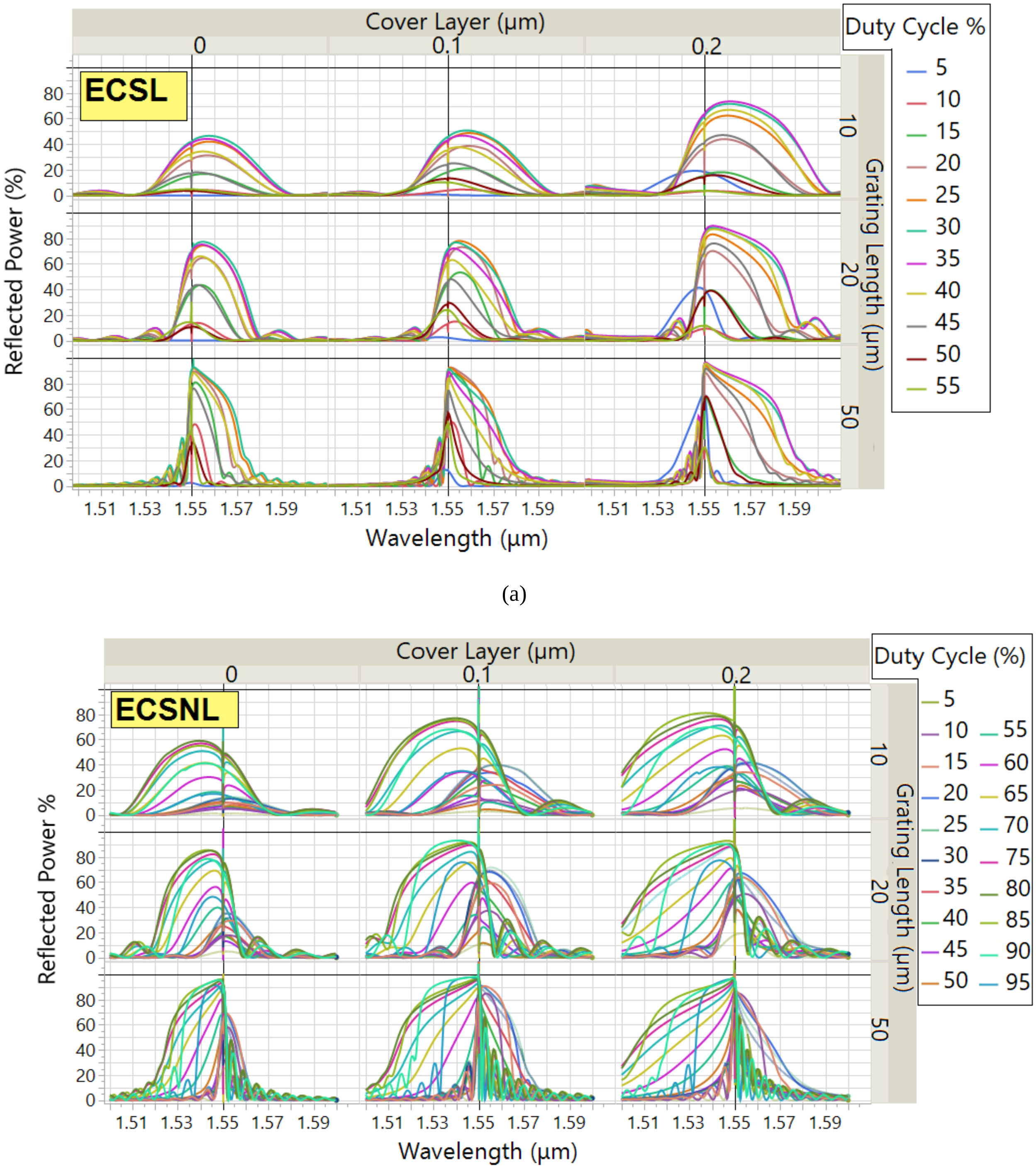

(a)

(b)

Figure 32. Reflected power as a function of wavelength and duty cycle for different lengths and cover layers for (a) ECSL and (b) ECSNL

Figure 33 shows the maximum reflected power near second Bragg wavelength for the ECSL and ECSNL structures. The blue line with no cover layer under ECSNL structure in Figure 33 represents the conventional DBR case. Comparing the three structures reveals that ECSL provides a higher maximum reflected power compared to that of conventional DBR. For ECSNL, cover layers greater than 0.1μm provide better reflectivity than that of a conventional DBR.

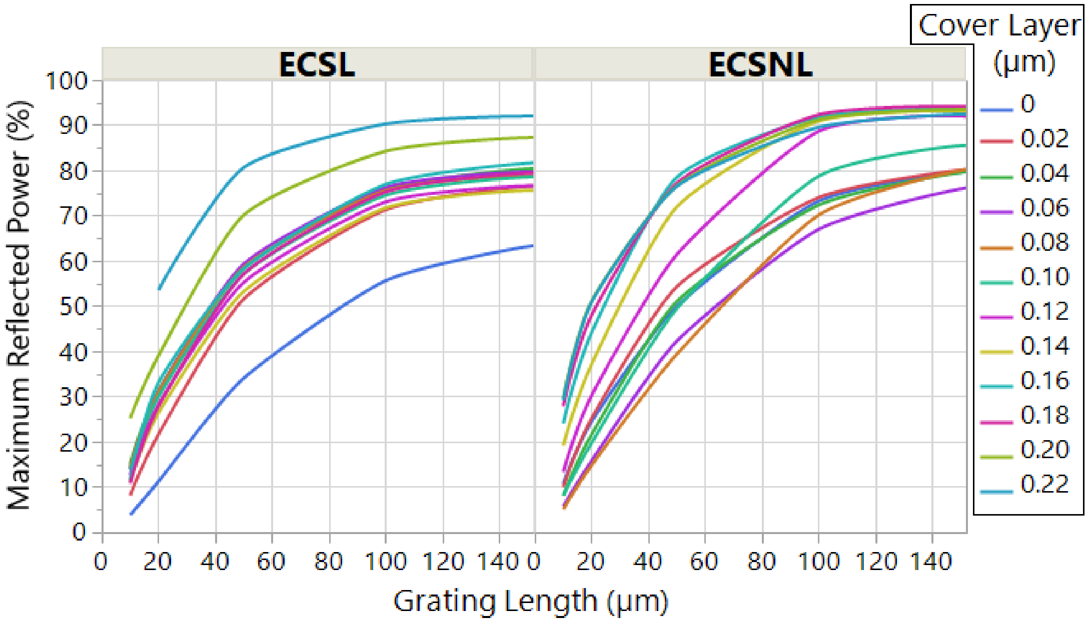

Figure 33 Maximum reflected power as a function of grating length for different cover layers for ECSL and ECSNL structure for 50% duty cycle

Figure 34 shows that longer gratings provide higher maximum reflectivity in both ECSL and ECSNL structures. In this case, the starting point of each curve in ECSNL represents the no cover case which is identical to a conventional DBR (marked with dashed lines). Comparing these starting points (or dashed lines) with the ECSL and ECSNL curves, indicates the advantage of proposed ECSL and ECSNL structure over conventional DBR gratings even in shorter gratings.

Another conclusion that can be drawn from Figure 33 is that increasing the cover layer thickness increases the reflectivity only up to a certain point. In the best case, ECSL offers %49 increase in maximum reflectivity for $0.2\mu m$ cover layer and $50\mu m$ grating length, while ECSNL offers %43 increase in maximum reflectivity for a cover layer of $0.16\mu m$ and grating length of $50\mu m$,. For shorter gratings such as $10\mu m$, ECSL and ECSNL provide 15% and 20% increase in the maximum reflected power, respectively.

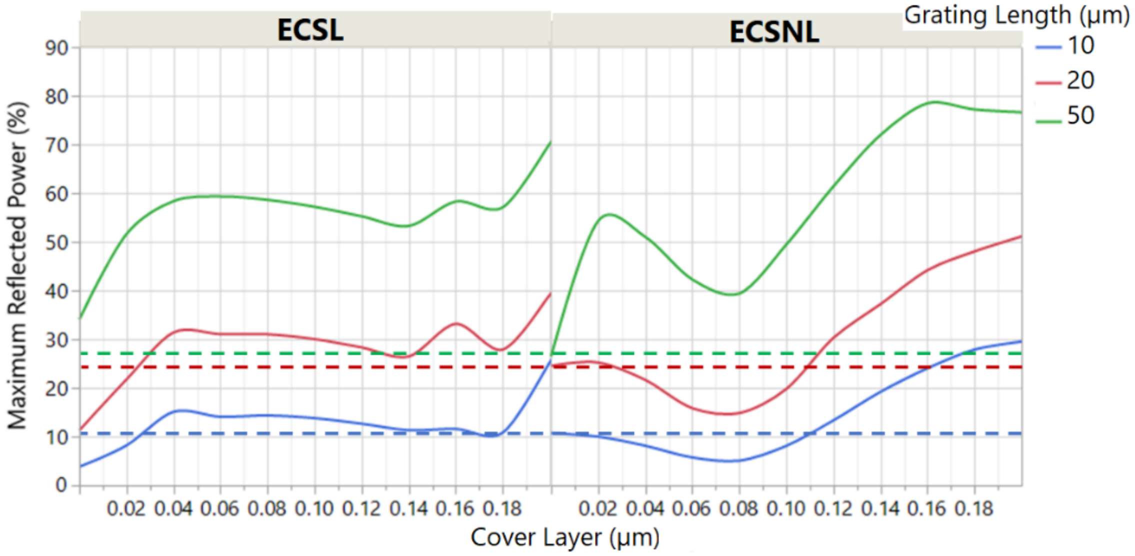

Figure 34. Maximum reflected power as a function of cover layer thickness for 10-50μm grating lengths for ECSL and ECSNL for 50% duty cycle for 75nm liner

The full width at half max (FWHM) is another important factor to evaluate performance of DBR reflectors, to ensure designing a mirror that works over a wide range of frequency. Figure 35 shows the reflectivity spectral width (FWHM) calculated from graphs shown in Figure 32 as a function of cover layer thickness for different grating lengths. Dashed lines indicate the FWHM of a conventional DBR that is color coded with the same length as indicated in the legend. The horizontal dashed lines indicating the FWHM of a conventional DBR with a $10\mu m$ length, shows that ECSL offers at least 20% more FWHM compared to a conventional DBR. However, in case of ECSNL, the FWHM is generally comparable or less than that of a conventional DBR for cover layers less than $0.2\mu m$, but increases after that.

For longer gratings, ECSL case offers almost the same amount of spectral bandwidth compared to a conventional DBR. ECSNL follows the same trend as we increase the grating length. This proves the advantage of ECSL structure over conventional DBRs when designing shorter gratings and advantage of ECSNL over conventional DBR gratings in certain cover layer thicknesses.

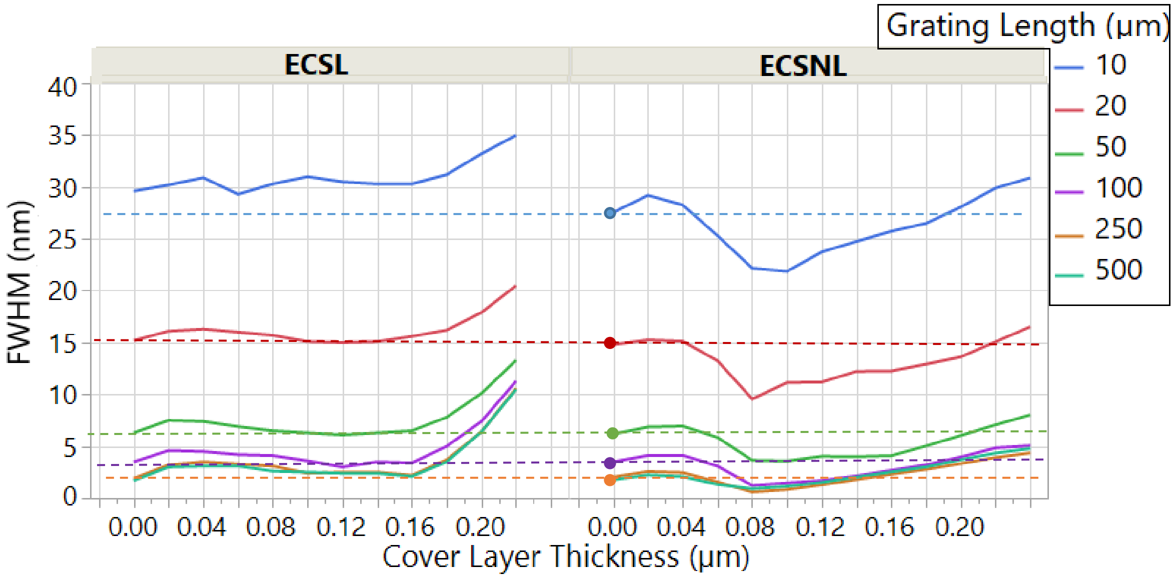

Figure 35. Reflectivity spectral width (FWHM) as a function of cover layer thickness for different grating lengths at 50% duty cycle. Dashed lines indicate FWHM of a conventional DBR with same layers and length.

3.4. First-Order ECSL and ECSNL Gratings

The two proposed structures ECSL and ECSNL are investigated near first order Bragg condition in [36] and [47]. The outcomes are briefly presented in this section since the author of this dissertation has helped with some of the simulations in that work. Similar to the work done at second-order Bragg condition, Floquet-Bloch theory is used to determine the proportion constant and power distributions. Figure 36 shows the reflected power as a function of wavelength when varying the liner thickness. Maximum reflectivity for 45nm and above shows less than a 2% increase, therefore 45nm liner thickness is deployed for the rest of the simulations.

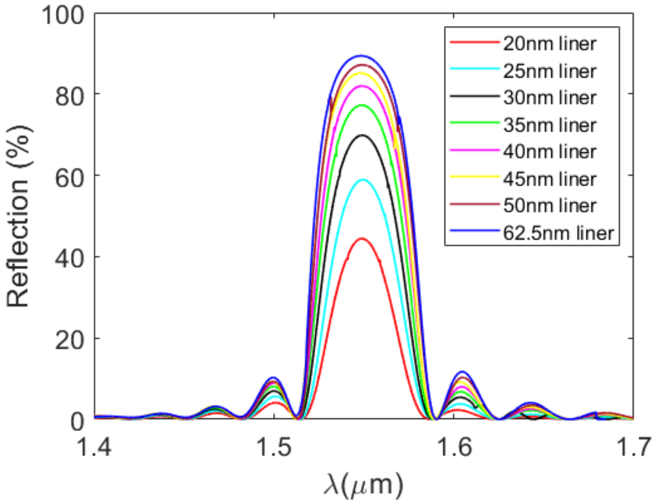

Figure 36. Reflectivity as a function of wavelength for different liner thicknesses (nm) in the ECSL grating structure [36], [47].

Figure 37 shows the normalized longitudinal propagation constant β/k_0 as a function of wavelength for a) ECSL with 25nm liner thickness, c) ECSL with 45nm liner thickness, and e) ECSNL when varying cover layer thicknesses. The attenuation constant reaches to its minimum at the first order condition at 1.55μm. Increasing the cover layer thickness. For ECSL structure with a 25nm and 45nm cover layer thickness, the peak happens at 100nm cover layer and 200nm cover layer thicknesses respectively. For the ECSNL structure, a cover layer of 220nm results in maximum attenuation. For first order gratings, the coupling coefficient κ is equal to the minimum of α, therefore the structure with highest maximum attenuation constant is desired.

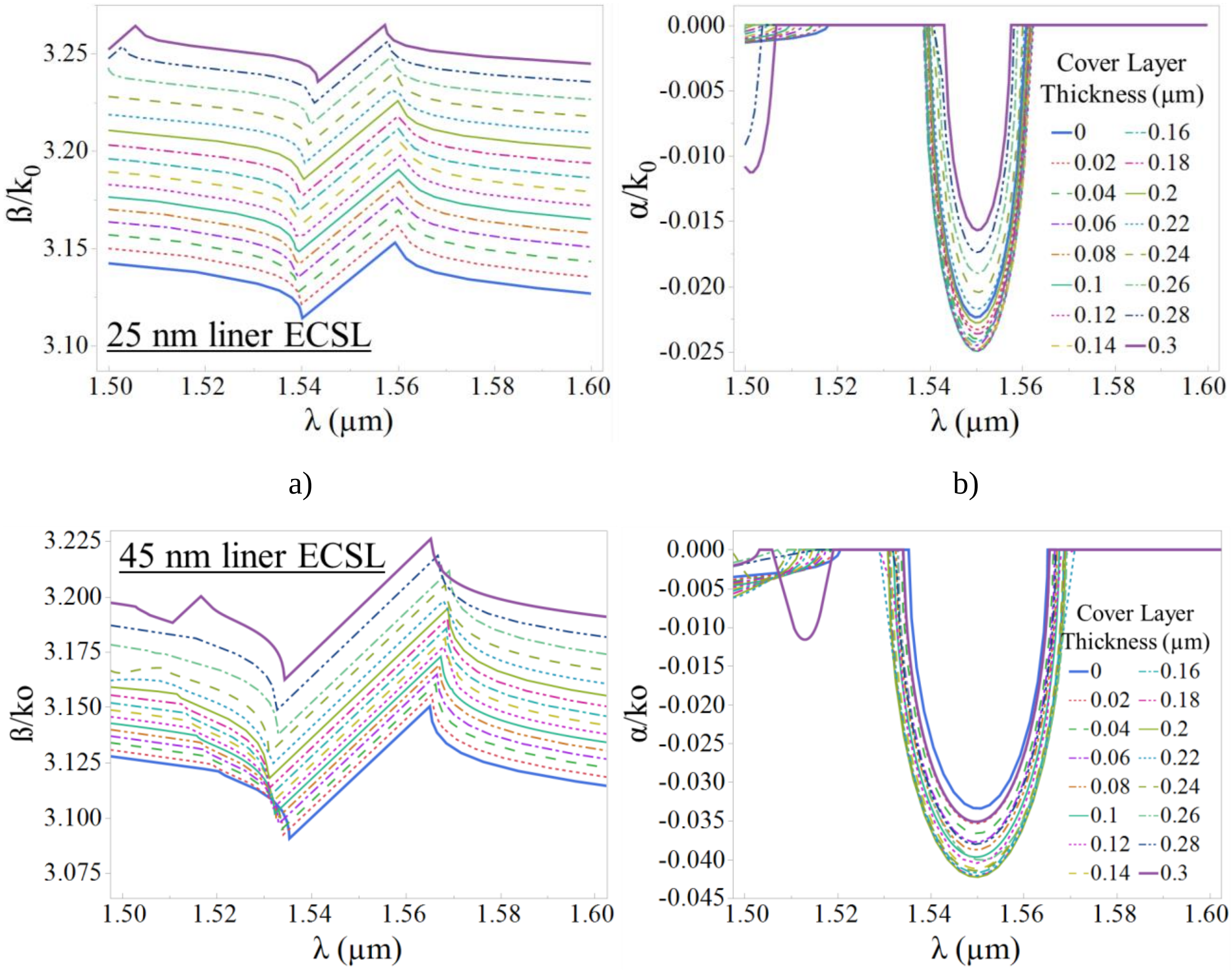

a) b)

c) d)

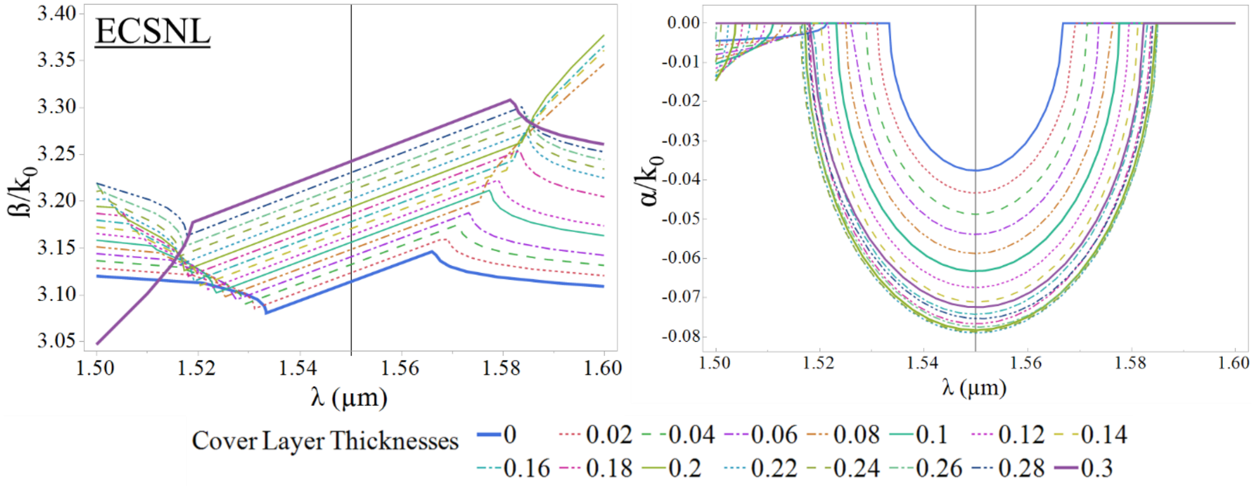

e) f)

Figure 37. Normalized longitudinal propagation constant, β/k_0 and normalized attenuation constant α/k_0, as a function of wavelength for ECSL with 25nm and 45 nm liner layer thickness and ECSNL for different cover layer thicknesses [36], [47].

Figure 38 (a) shows the maximum reflectivity as a function of cover layer thickness for different grating lengths for ECSL structure with 25nm and 45nm liner thickness as well as for ECSNL structure. Dashed lines indicate the conventional structure corresponding to each case. Increasing the cover layer thickness substantially increases the maximum reflectivity for the ECSNL structure even for short gratings. For both cases of ECSL, maximum reflectivity reaches its peak around 0.1μm cover layer and decreases when further increasing the cover layer thickness. For ECSNL structure, 0.22μm is the optimum cover layer thickness which is doubled the amount of reflectivity a similar conventional DBR produces.

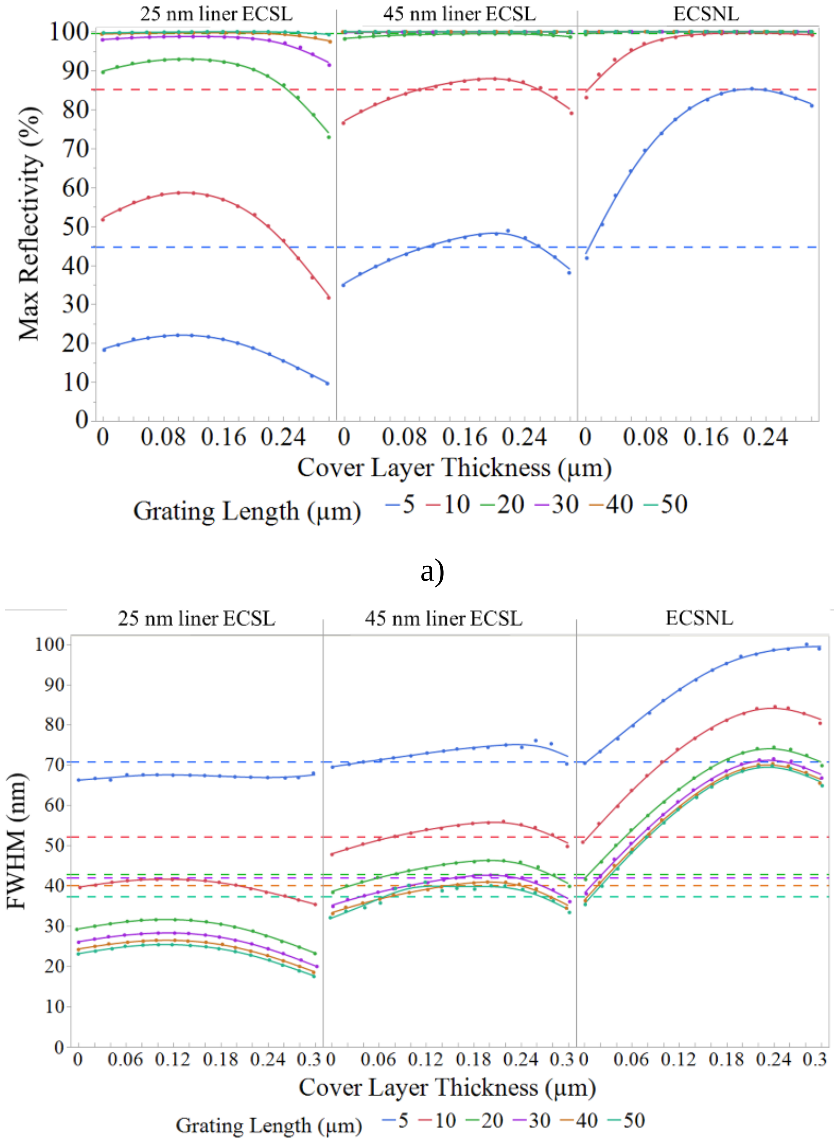

a)

b)

Figure 38. Maximum reflectivity and reflectivity spectrum as a function of cover layer thickness for different grating length ECSL structure with a liner thickness of 25 nm and 45 nm and for ECSNL structure [36], [47].

Chapter 4

LASER-EAM TRANSCEIVER DEVICE

The idea behind the proposed optical transceiver device is to have a fast, efficient laser-EAM module that is not sensitive to temperature change and functions at a single frequency. An ideal laser for this purpose is a DBR laser. DBR lasers are tunable single-mode lasers with Bragg gratings as their mirrors. The EAM is designed to be tunable with the laser (since they share the same epi). The lasing frequency of the laser changes with temperature, making it possible for both devices to operate with high efficiency around the same frequency. However, this device's passive components i.e., the grating mirrors and out-coupler do now follow the same rule. The grating's reflectivity/out-coupling is fixed over a specific wavelength spectrum. Which makes it challenging to design a device that works over a wide range of temperatures. To tackle this issue, the gratings were designed to have a high reflectivity/out-coupling over a wide range of wavelengths. In other words, to have a high reflectivity/out-coupling spectral width.

Figure 39 shows a sketch of the laser-EAM device. This device consists of two active components, a laser, and electro-absorption modulator and the passive components including a back DBR reflector mirror, a front DBR reflector mirror, a grating out-coupler, and two optional photodiodes at the two ends to convert the optical output to an electric signal and vice versa to be used in an integrated circuit. All of which are connected to each other through a common waveguide that carries the light. The out-coupler makes it possible to feed the light into an optical fiber to transfer the signal into the short haul. Designing the device to work at the wavelength 1550nm makes it compatible with the current fiber optics networks.

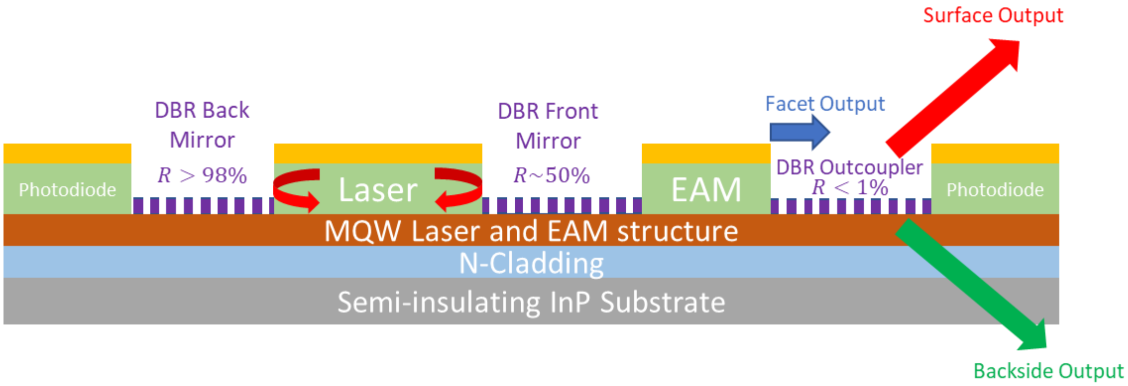

Figure 39. Schematic graph of the cross-section of the laser-EAM structure from a side view

In order for the light to be amplified in the laser cavity, the laser's back mirror needs to be of the highest reflectivity. However, the front mirror must be reflective enough to satisfy the lasing condition but non-reflective enough to let the intensified light pass through the laser structure as shown in Figure 39. On the other hand, the grating out-coupler is designed to have minimum reflectivity and maximum out-coupling.

In the following section, an enhanced coupling strength grating structure is analyzed and optimized to be used for the laser-EAM device. Grating depth, grating location and cover layers are varied to maximize the out-coupled power of a simplified structure. The result of this optimization is used as an estimate to simulate and find the characteristics of the complete epi design.

4.1. Epitaxial Structure

Choosing the right growth method and epitaxial stack is the first fundamental step in making semiconductor devices. Molecular beam epitaxy (MBE) and metalorganic chemical vapor deposition (MOCVD) are the two common methods to grow epitaxial layers for compound semiconductor devices and photonic integrated circuits. MBE method has some advantages over MOCVD. MBE method is an example of thin film deposition, meaning ultra-thin layers of desired layer grow one atomic layer at a time on the substrate. This gives an extremely high level of control over the thickness, composition, doping and quality of the epi stack. In MBE method the substrate is heated up and bombarded with gaseous atoms or molecules of the crystal a designer is trying to create. Upon landing the molecule on the substrate, it condenses and builds up slowly and systematically in ultrathin layers [48]. This process takes place in an ultra-high vacuum (UHV, extremely low pressure) which eliminates the chance of contamination and makes this method very precise. This could be one drawback of MBE method, since it requires a UHV medium it is more difficult and costly to make. Besides, MOCVD has the advantage of being cheaper.

For this device an indium-phosphide (InP) substrate is selected because it has a direct bandgap and is commonly used in integrated photonic devices and optoelectronic circuits. InP-based lasers operate in a longer wavelength regime compared to gallium arsenide (GaAs) based devices which makes them ideal to work with optical fibers that have the lowest attenuation in wavelengths between 1510-1600nm. For this project, everything is designed to work at 1550nm wavelength at room temperature. InP wafers with a diameter of 3” and a thickness of 600μm was used as a substrate and the epi growth was designed according to the desired characteristics for the device and was ordered from IntelliEpi.

To design the transceiver device, it is necessary to have an active region designed to produce high gain and efficient electro-absorption, while the passive region (waveguides) need to have low losses and to provide the desired amount of outcoupled, transmitted and reflected light. Furthermore, the coupling loss between the active region and passive region should be minimized. This can be achieved by using multiple quantum well devices as the active region. For InP the lasing wavelength changes with a rate of 5A/C.

In designing the laser structure, a complete modal analysis has to be performed to find the effective index, confinement factors for all layers, modal gain, beam divergence and the threshold current. The first step is to choose the right epi stack that would enable the designer to achieve the design requirements for every element of the transceiver device. Table 1 exhibits the 11-QW epi stack designed at 1550nm wavelength. This table includes the refractive index of each layer with up to 5 decimal point accuracy calculated at 1550nm wavelength using the Waveguide-3 program. The index for the quantum well and barriers is calculated at three different y values to provide a more accurate index which means when visualizing the quantum well indices, the top of the quantum wells gradually decrease and then drop to the barrier level as shown in some of the figures in the next section.

Table 1 shows the structure that is shared between the laser, modulator and dummy ridges once ridges are defined. Extra layers of amorphous silicon, nitride and spin-on-glass are later deposited to construct each element. In designing the epi stack the InP buffer layer must be thick enough to provide optical confinement for the beam throughout the device. 3-inch, 600μm thick InP wafers are used as substrate and each layer is designed to be lattice matched with the previous layer beneath to reduce the strain.

Table 1. Complete epi stack for 11QW structure used for NASA Phase I at 1550nm

Layer Name	Material	Repeat	Thickness (Å)	Thickness (um)	Type	Index start	Index End
Sacrificial	InP		500	0.05			
	In(x)Ga(1-x)As		1224.8	0.12248	P		3.50423
InGaAsP	In(x)Ga(1-x)As(1-z)P(z)		612.4	0.06124	P		3.23169
	InP		1000	0.1	P	3.14108	3.12139
	InP		5124	0.5124	P		3.15845
	InP		4286.8	0.42868	P		3.16159
	InP		50	0.005	P		3.15845
	In(x)Ga(1-x)As(1-z)P(z)		100	0.01	P		3.27128
	InP		**50**	0.005	P		3.15845
	InP		**600**	0.06	P		3.16159
	InP		**50**	0.005	P		3.15636
3 InAlGaAs Sub Layer Digital Grading	In(x)Al(y)Ga(1-x-y)As		122.5	0.01225	P	3.24994	3.27018
3 InAlGaAs Sub Layer Digital Grading	In(x)Al(y)Ga(1-x-y)As		122.5	0.01225	P	3.37056	3.28373
2 InAlGaAs Sub Layer Digital Alloy	In(x)Al(y)Ga(1-x-y)As		898.8	0.08988	P	3.41304	3.41341
2 InAlGaAs Sub Layer Digital Alloy	In(x)Al(y)Ga(1-x-y)As		269.5	0.02695	P	3.41479	3.41327
2 InAlGaAs Sub Layer Digital Alloy	In(x)Al(y)Ga(1-x-y)As		36.7	0.00367	UID		3.415
3 InAlGaAs Sub Layer Digital Grading	In(x)Al(y)Ga(1-x-y)As		100	0.01	UID	3.50647	3.45124
Barrier	In(x)Al(y)Ga(1-x-y)As		49.9	0.00499	UID		3.3858
QW	In(x)Al(y)Ga(1-x-y)As	11	100	0.01	UID		3.58104
Barrier	In(x)Al(y)Ga(1-x-y)As		49.9	0.00499	UID		3.3858
3 InAlGaAs Sub Layer Digital Grading	In(x)Al(y)Ga(1-x-y)As		150	0.015	UID	3.39623	3.50279
2 InAlGaAs Sub Layer Digital Alloy	In(x)Al(y)Ga(1-x-y)As		55	0.0055	UID		3.36821
2 InAlGaAs Sub Layer Digital Alloy	In(x)Al(y)Ga(1-x-y)As		100	0.01	N	3.36042	3.36483
3 InAlGaAs Sub Layer Digital Grading	In(x)Al(y)Ga(1-x-y)As		100	0.01	N	3.26852	3.31771
	In(x)Al(y)Ga(1-x-y)As		100	0.01	N		3.23355
3 InAlGaAs Sub Layer Digital Grading	In(x)Al(y)Ga(1-x-y)As		100	0.01	N	3.26138	3.24557
	InP		10000	1	N		3.16044

4.2. Complete Epi Stack Simulation Results

In the previous section it was proved that a structure similar to ECSNL can produce maximum out-coupling compared to a conventional grating. Using these results gives a good starting point that can be used as initial guess when simulating a more complicated grating that is composed of the 11-QW structure epi-stack shown in Table 1.

When designing the gratings with the full epi stack, in an attempt to get the most accurate results, the filling and cover layer were both chosen based on the real material that was at hand to be used to fabricate the devices. Spin-on-Glass (SOG) from Futurrex called *Intermediate Coating IC1-200 (SOG)* was used as the low index material. SOG makes a good candidate since it is often applied to smoothen surface topology and to fill narrow trenches in surface topology. The refractive index of this material is related to the wavelength with Eq. (4.1). Maximum recommended film thickness of IC1-200 is 0.5µm according to the datasheet which is far more than the thickness used to fill the grooves here (0.1µm).

$$n(\lambda) = A + B/\lambda^2 + C/\lambda^4 \tag{4.1}$$

Where λ is wavelength in microns and the constants A, B and C are called Cauchy Coefficients and for IC1 type material can be found from Table 2. At wavelength 1.55µm this formula results in refractive index of 1.424.

Table 2. Cauchy Coefficients for SOG IC1 type material [49].

	A	B (µm²)	C (µm⁴)

IC1-200 (no bake)	1.4222	0.00461	-7.508 x 10^{-5}

As for the high index cover layer, a layer of amorphous silicon is used with a refractive index of 3.5289 which falls close to the estimate used in previous calculations.

The remaining factors that need to be explored to design an optimum grating structure are to decide at which layer to etch the gratings, and to find how deep to etch the gratings, the grating depth, t_g. Since the grating layer is going to be etched down into an already set epi stack, the gratings can be at different layers for each component in an integrated device based on the requirements for each device. That being said, in designing the front and back DBR grating mirrors shown in Figure 39, the goal is to get high reflectivity whereas for designing the outcoupler shown in Figure 39. Here, the focus is to maximize the outcoupled power and minimize the reflectivity. In the following section, different layers at which the grating is placed is explored by comparing the α/k_0 or $\alpha\Lambda$ and β/k_0 or $\beta\Lambda$ as a function of $k_0\Lambda$, as well as power distribution as a function of wavelength to conclude how deep and where the grating should be etched at.

4.2.1. Exploring Location of the First-order DBR Gratings

In this section, eight cases are explored where the grating is placed at different layers with different depths to find out the optimum result to be used for the DBR front and back mirror grating. Previously, it was shown that the first Bragg condition is more suitable for reflectors, therefore the structures in this section are all designed around first Bragg condition where grating period $\Lambda_{1st} = \lambda_0/2n_{eff}$.

Figure 40 shows the index of refraction and mode intensity across the space for the epi structure proposed (referred to as DoE structure). This would indicate Case 1 where there is no grating etched in the structure yet, so this is what the mode sees when it travels in the waveguide connected to the grating before it enters the grating. The layer numbering used in this section are as indicated.

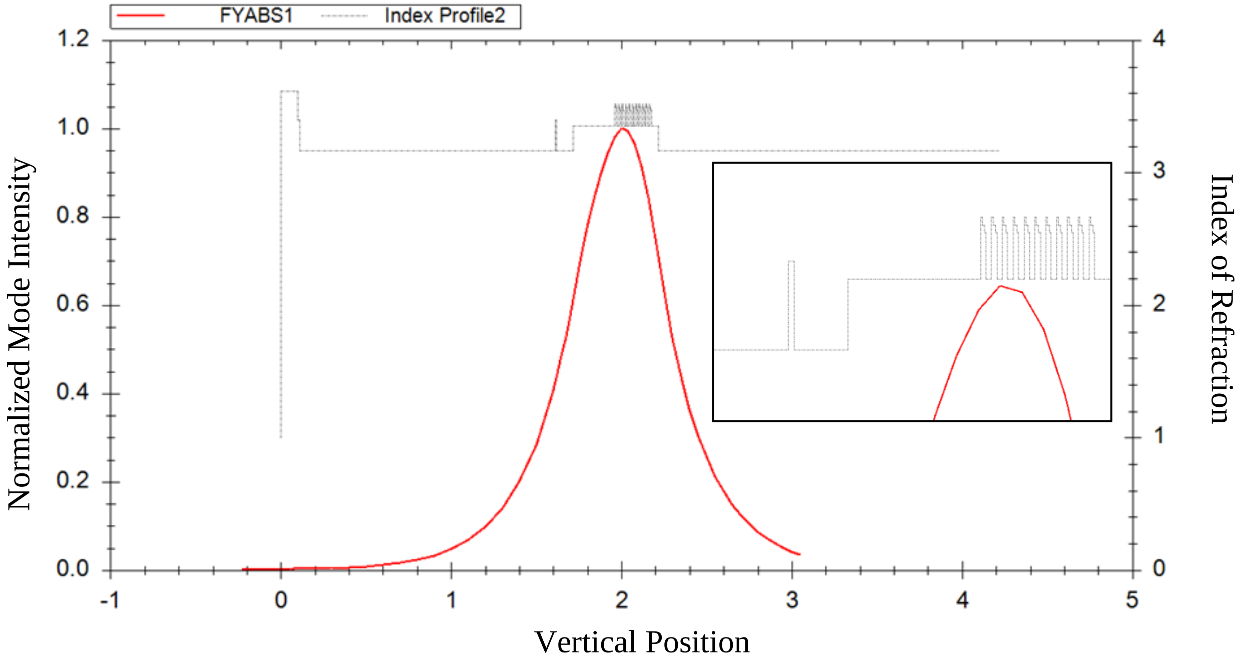

Figure 40. Index and mode propagation as a function of space for the full epi stack before etching the grating (case 1). The top of the mode is blown up to see better.

Before deploying the concept of ECS, in an attempt to find the best layer to put the gratings on, six different cases are explored for a conventional DBR grating starting by putting the grating in layer 12 with the grating depth at 25nm, 50nm, 74nm and100nm as shown in Figure 41. To simplify the problem, the z-axis (vertical position) origin is assumed to be at the center of the grating structure.

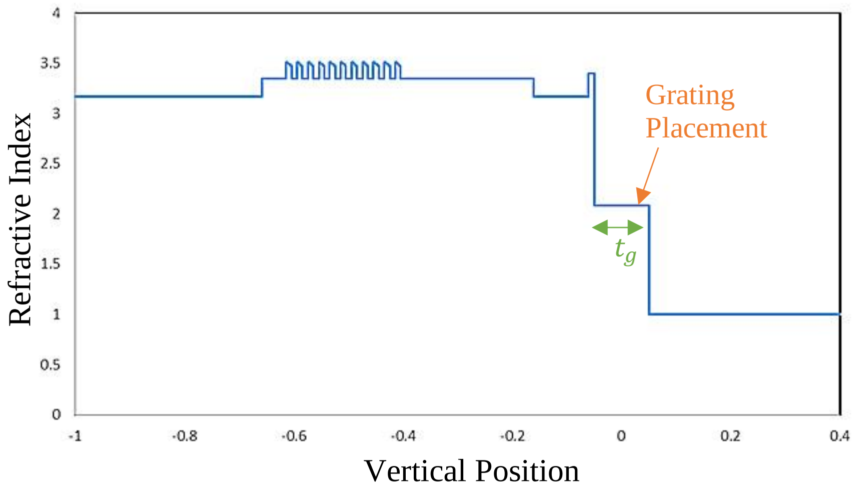

Figure 41. Case 2 where grating is placed in layer 12 and grating depth, t_g varies.

Simulation of Case 2 results in maximum reflected power of $P_R = 52.4\%$ within a spectral width of $\Delta\lambda = 4\ nm$ for Case 2 (a), $P_R = 41.2\%$ within a spectral width of $\Delta\lambda = 3.75\ nm$ for Case 2 (b), $P_R = 26\%$ within a spectral width of $\Delta\lambda = 3.47\ nm$ for Case 2 (c), and $P_R = 9.09\%$ within a spectral width of $\Delta\lambda = 3.23\ nm$ for Case 2 (d) as shown n Figure 42. Normalized real and imaginary part of attenuation constant or $\alpha\Lambda$ and $\beta\Lambda$ is shown in Figure 43 for Case 2 for different t_g values.

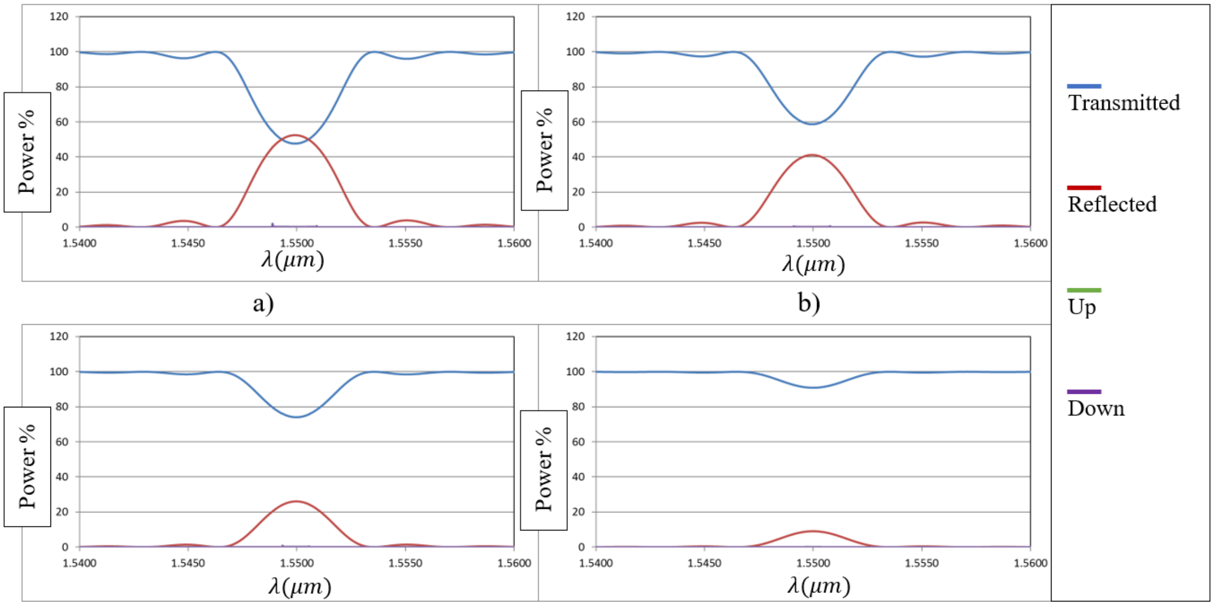

a) b) c) d)

Figure 42. Normalized power distribution as a function of wavelength at grating depths of a) $t_g = 100\ nm$, b) $t_g = 75\ nm$, c) $t_g = 50\ nm$, and d) $t_g = 25 nm$.

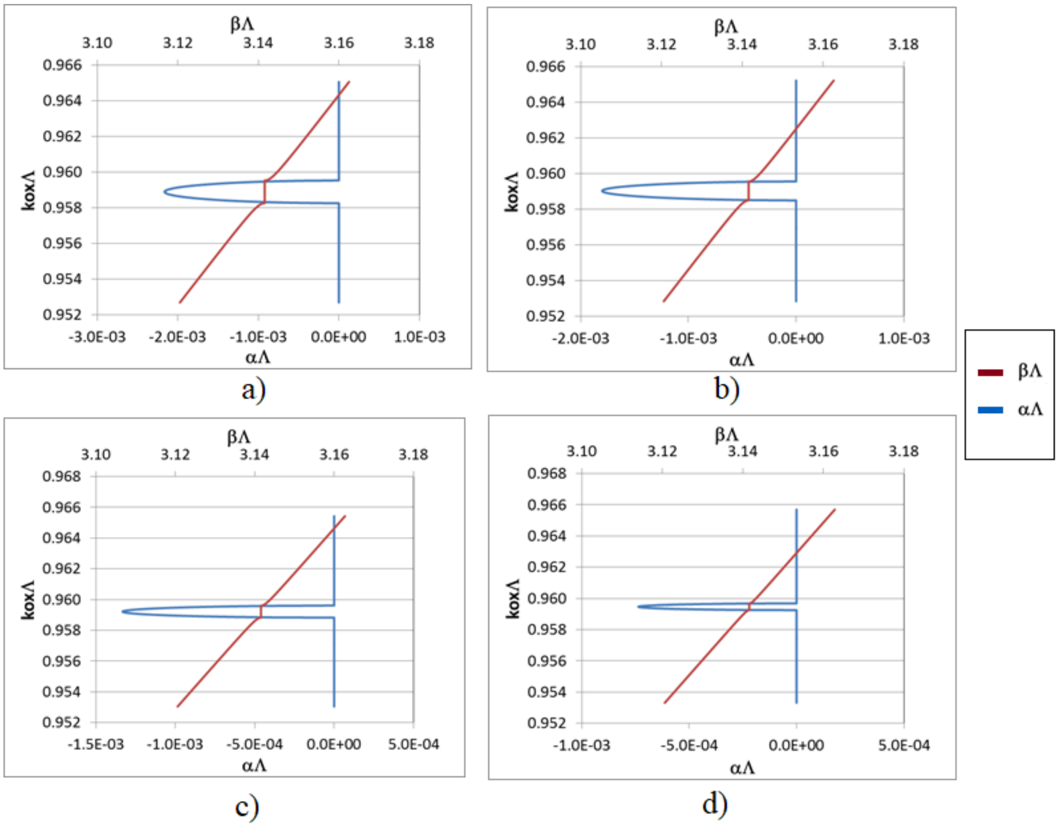

Figure 43. Normalized attenuation, $\alpha\Lambda$, and normalized real part of the longitudinal propagation constant, $\beta\Lambda$, as a function of normalized reciprocal wavelength, $k_0\Lambda$, for Case 2 when a) $t_g = 100nm$, b) $t_g = 75nm$, c) $t_g = 50\ nm$ and d) $t_g = 25nm$.

Next, Case 3 is defined where the grating is placed in layer 13 and etched down to the depth of t_g. Figure 44 shows the power distribution for this case when a) t_g =100nm, b) t_g=75nm, c) t_g =50nm and d) t_g=25nm. Figure 45 indicates the normalized attenuation constant and propagation constant for each of these cases as a function of normalized reciprocal wavelength.

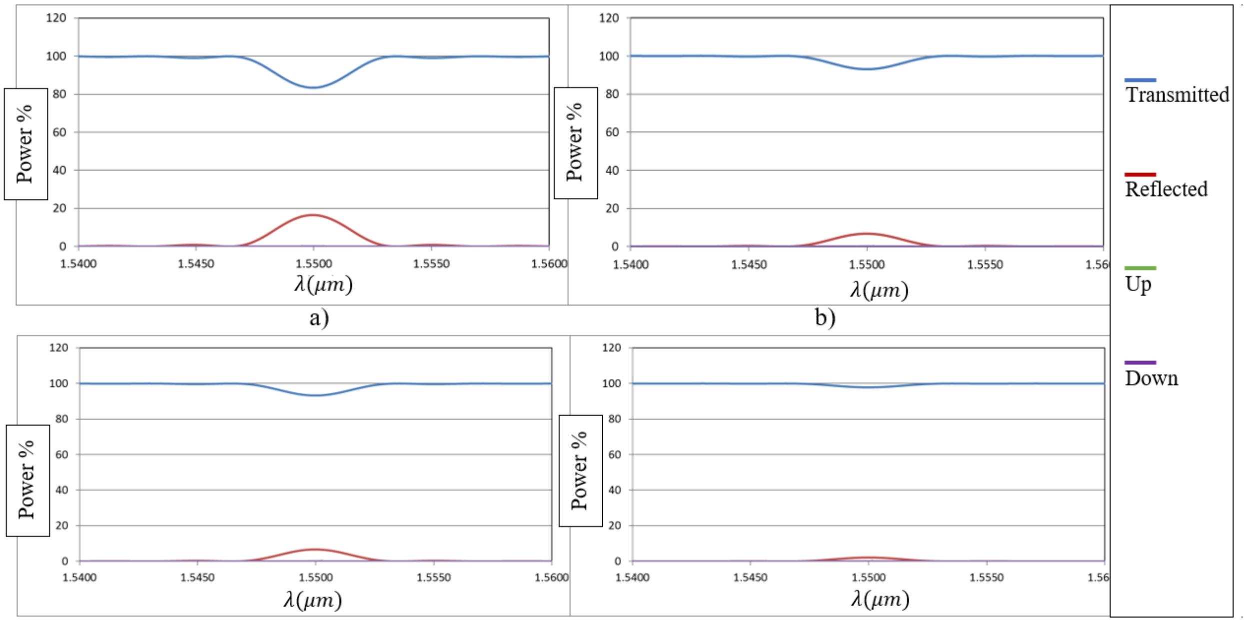

a)

b)

c)

d)

Figure 44. Power distribution as a function of wavelength for Case 3 with a) $t_g = 100nm$, b) $t_g = 75nm$, c) $t_g = 50nm$ and d) $t_g = 25nm$.

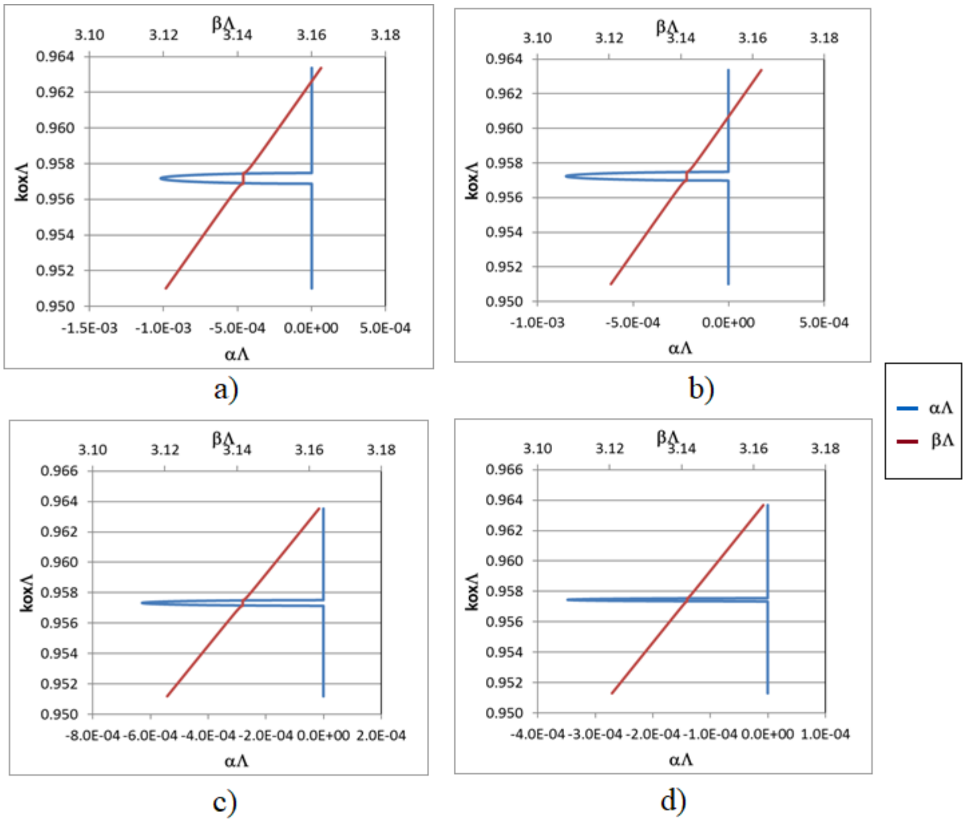

Figure 45. Normalized attenuation, $\alpha\Lambda$, and normalized real part of the longitudinal propagation constant, $\beta\Lambda$, as a function of normalized reciprocal wavelength, $k_0\Lambda$, for Case 3 when a) $t_g = 100nm$, b) $t_g = 75nm$, c) $t_g = 50\ nm$ and d) $t_g = 25nm.$

Placing the grating at layer 9 is investigated in Case 4. Power distribution as a function of wavelength and normalized attenuation and propagation constant as a function of grating period are shown for different grating depths in Figure 46 and Figure 47, respectively. A drastic improvement is observed both in maximum reflected power and the reflectivity spectral width which makes layer 9 more suitable for location of the grating. Reflected power goes up to 100% when a 100nm cover layer is applied which makes this design more suitable to be used as a back reflector for a DBR laser where maximizing the reflected power is the goal.

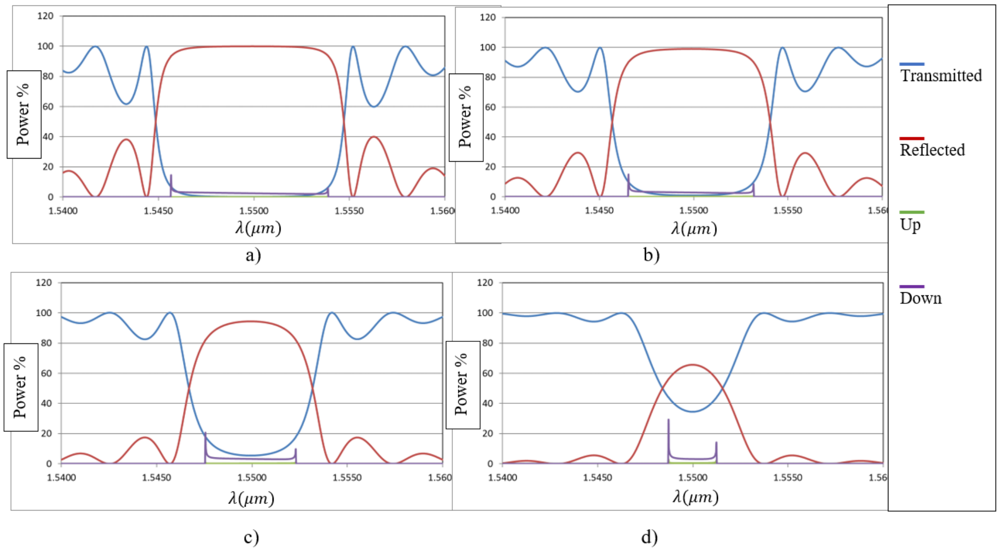

Figure 46. Power distribution as a function of wavelength for Case 4 with a) $t_g = 100nm$, b) $t_g = 75nm$, c) $t_g = 50nm$ and d) $t_g = 25nm$.

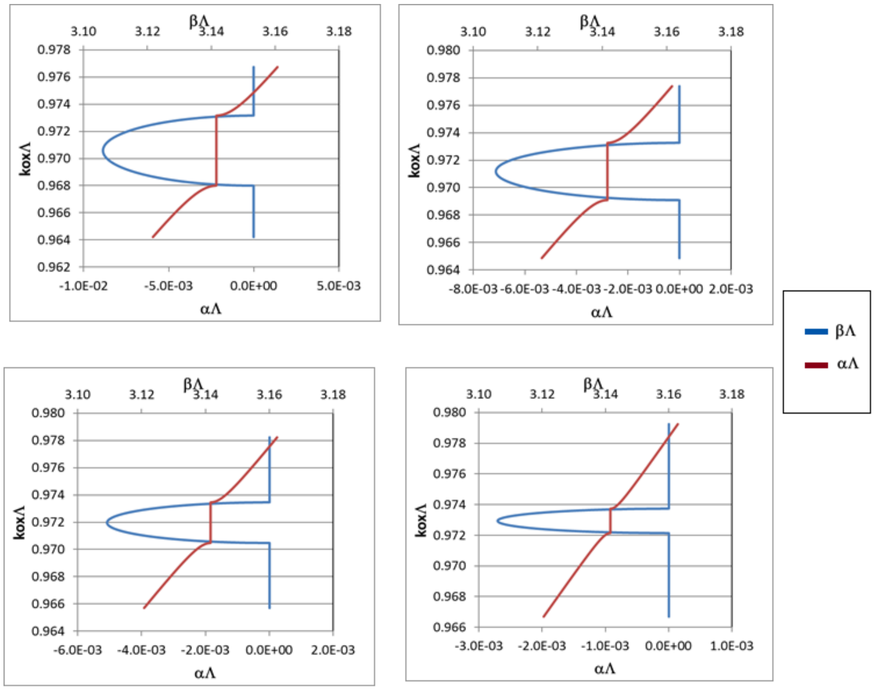

Figure 47. Normalized attenuation, $\alpha\Lambda$, and normalized real part of the longitudinal propagation constant, $\beta\Lambda$, as a function of normalized reciprocal wavelength, $k_0\Lambda$, for Case 4 when a) $t_g = 100nm$, b) $t_g = 75nm$, c) $t_g = 50\ nm$ and d) $t_g = 25nm$

Next is Case 5 where grating is placed in layer 8. Figure 48 shows the power distribution as a function of wavelength for this structure for different grating depths. This case also provides high reflectivity over an even a larger span of wavelength compared to Case 4.

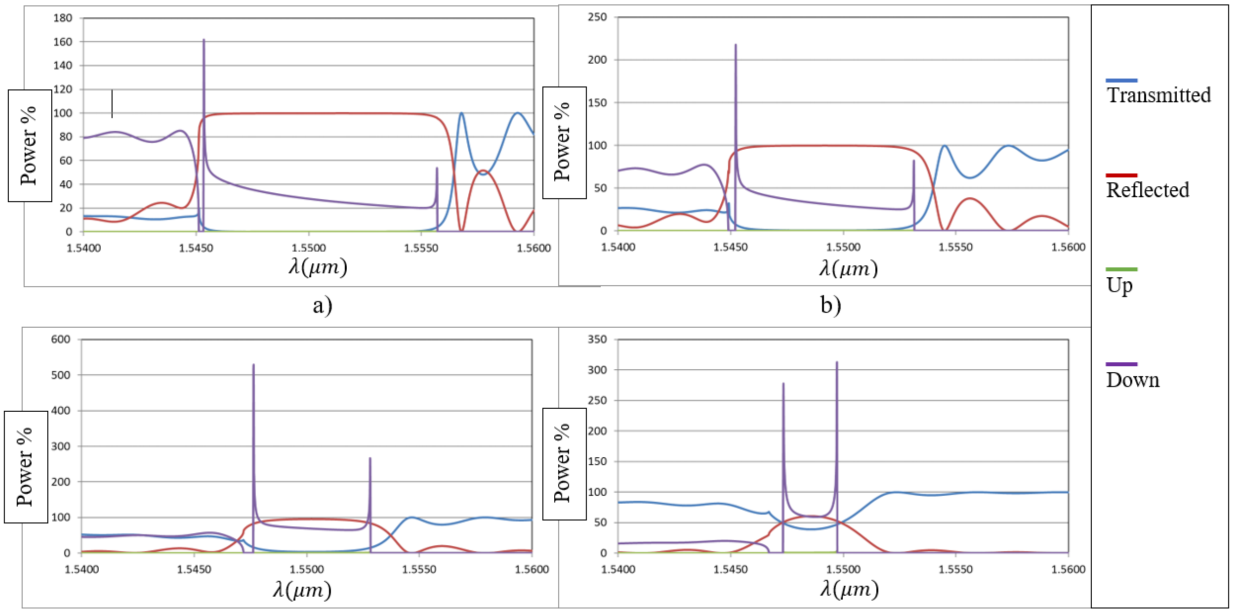

a) b) c) d)

Figure 48. Power distribution as a function of wavelength for Case 5 with a) $t_g = 100nm$, b) $t_g = 75nm$, c) $t_g = 50nm$ and d) $t_g = 25nm$.

Figure 49 shows the normalized attenuation constant and the real part of longitudinal propagation constant as a function of normalized grating period for Case 5 for different grating depths.

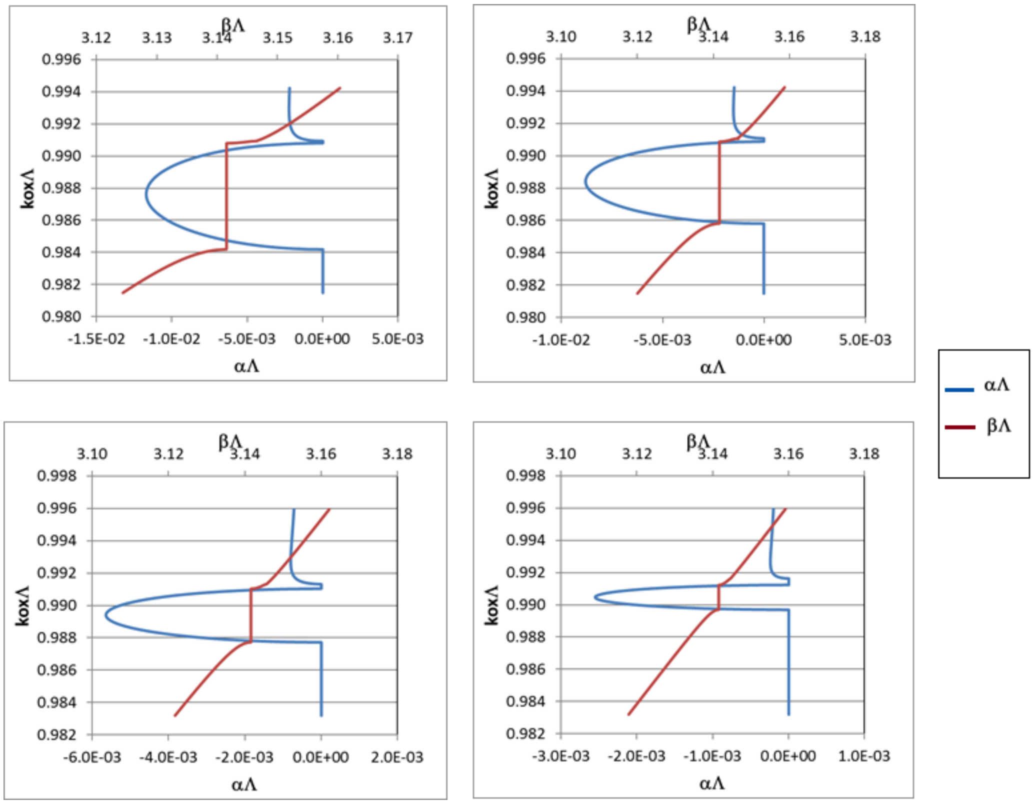

Figure 49. Normalized attenuation, $\alpha\Lambda$, and normalized real part of the longitudinal propagation constant, $\beta\Lambda$, as a function of normalized reciprocal wavelength, $k_0\Lambda$, for Case 5 when a) $t_g = 100nm$, b) $t_g = 75nm$, c) $t_g = 50\ nm$ and d) $t_g = 25nm$

The grating is placed on layer 10 where the top InP layers are etched away and the grating goes into the InGaAsP layer in Case 6. Placing the grating in layer 10 results in up to 80% reflected power which is desired for a front mirror of a DBR laser where reflectivity should be high enough to ensure lasing at the central wavelength while enabling the resonated light to pass through the front side of the laser into the waveguide and next component.

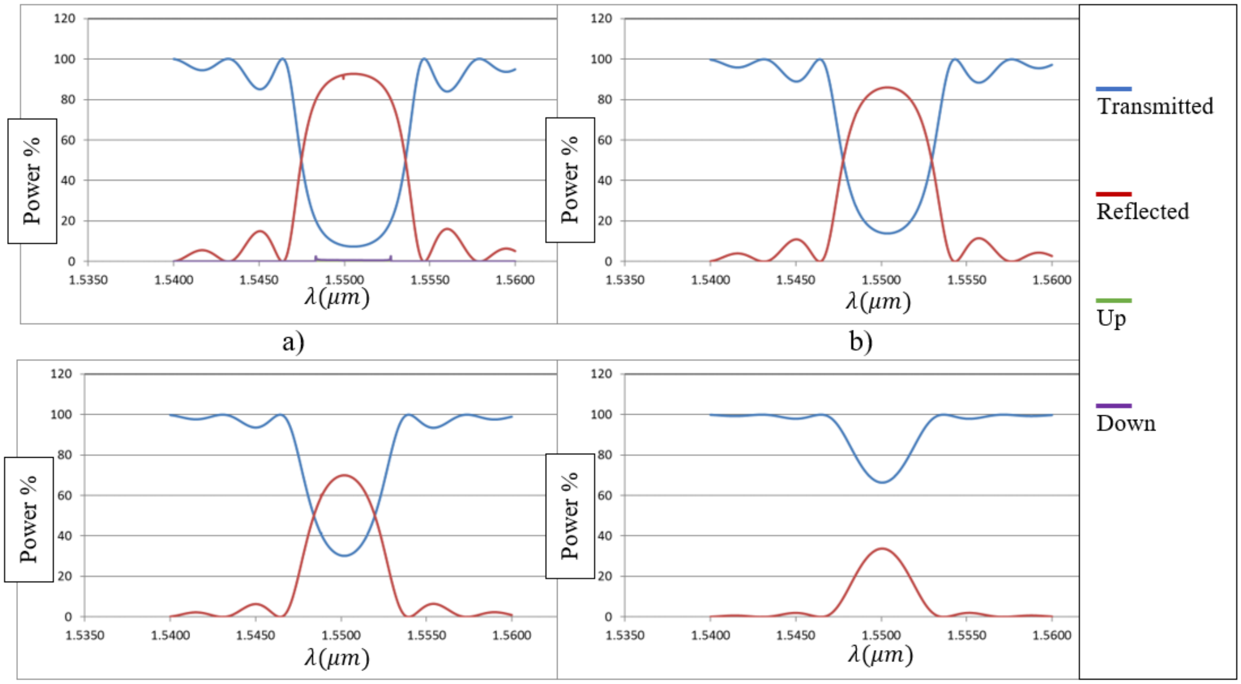

a) b) c) d)

Figure 50. Power distribution as a function of wavelength for Case 6 with a) $t_g = 100nm$, b) $t_g = 75nm$, c) $t_g = 50nm$ and d) $t_g = 25nm$.

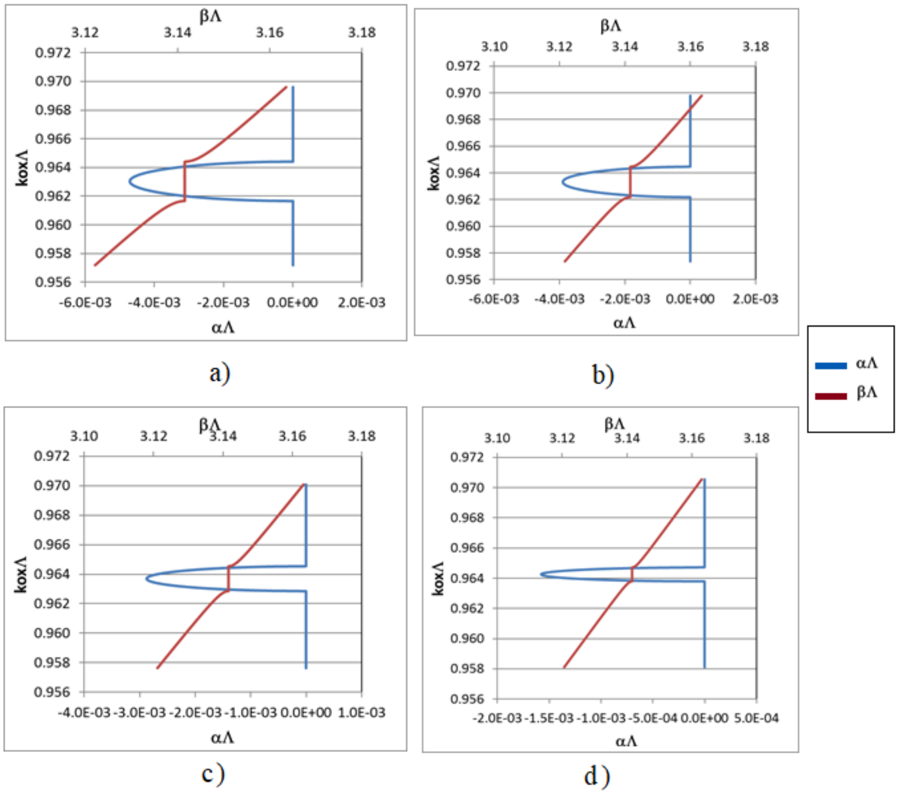

Figure 51. Normalized attenuation, $\alpha\Lambda$, and normalized real part of the longitudinal propagation constant, $\beta\Lambda$, as a function of normalized reciprocal wavelength, $k_0\Lambda$, for Case 6 when a) $t_g = 100nm$, b) $t_g = 75nm$, c) $t_g = 50\ nm$ and d) $t_g = 25nm$

Table 3 and Figure 52 show the comparison between the maximum reflected power provided by the grating for each case as well as the reflectivity spectral bandwidth ($\Delta\lambda$ in nm) for each case for different grating depths of 25, 50, 75 and 100nm. In all cases, a grating depth of 100nm provides the highest out-coupling as well as the maximum reflectivity spectral width. Comparing the results from each case indicates that case 5 provides maximum reflected power. However, it is preferred not to put the grating into the quantum well regions. Therefore, Case 6 is selected as the best design for this purpose.

Table 3. Spectral width and reflected power for different grating depths for Cases 2 - 6

	$\Delta\lambda\ (nm)$				Reflected Power %			
$t_g (nm)$	**25**	**50**	**75**	**100**	**25**	**50**	**75**	**100**
Case 2	3.23	3.47	3.75	4.00	9.09	26.0	41.2	52.4
Case 3	3.15	3.21	3.27	3.34	2.15	6.78	11.9	16.6
Case 4	4.42	6.58	8.39	9.86	65.6	94.5	99.0	99.8
Case 5	4.05	6.66	9.18	11.4	60.8	96.2	99.8	100
Case 6	3.60	4.56	5.48	6.22	33.7	69.9	86.1	92.7

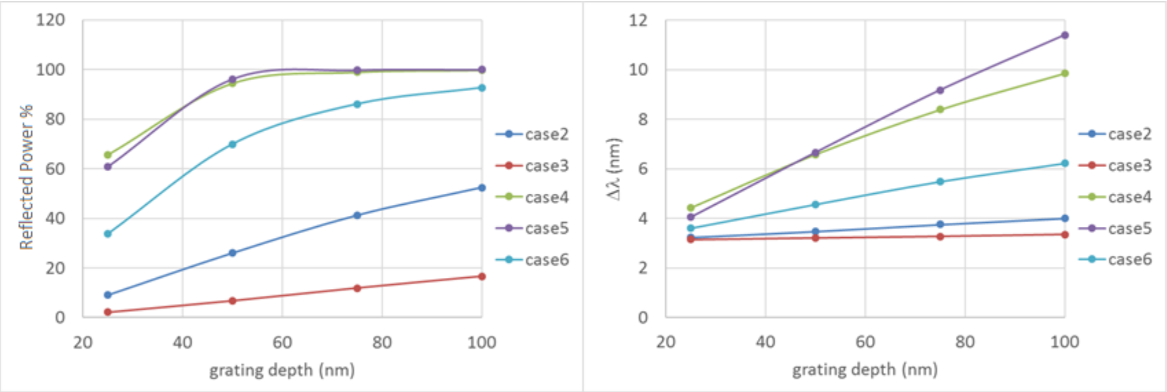

a)

b)

Figure 52. Reflected power and spectral width ($\Delta\lambda$) as a function of grating depth for Cases 2-6

In order to enhance the reflectivity of this case, the concept of ECSNL is used where the grooves are filled with spin-on-glass (SOG) with low index material and amorphous silicon as cover layer.

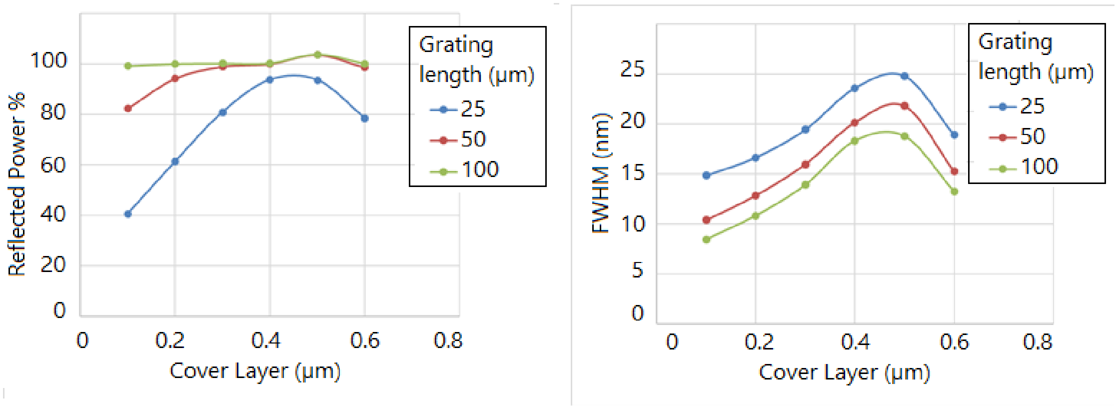

a) b)

Figure 53. Maximum a) reflected power and b) reflectivity spectral width as a function of cover layer for grating lengths 25µm, 50µm and 100µm for a grating with 0.1µm depth.

Another case is when the grating design is the same as enhanced Case 6 is when grating is placed in layer 9, called Case 8. Figure 54 shows the maximum reflected power and spectral width for this case for cover layers 0.2µm and 0,3µm for different grating depths. In this case a deeper grating is desired as opposed to the shallower grating presented in Case 6.

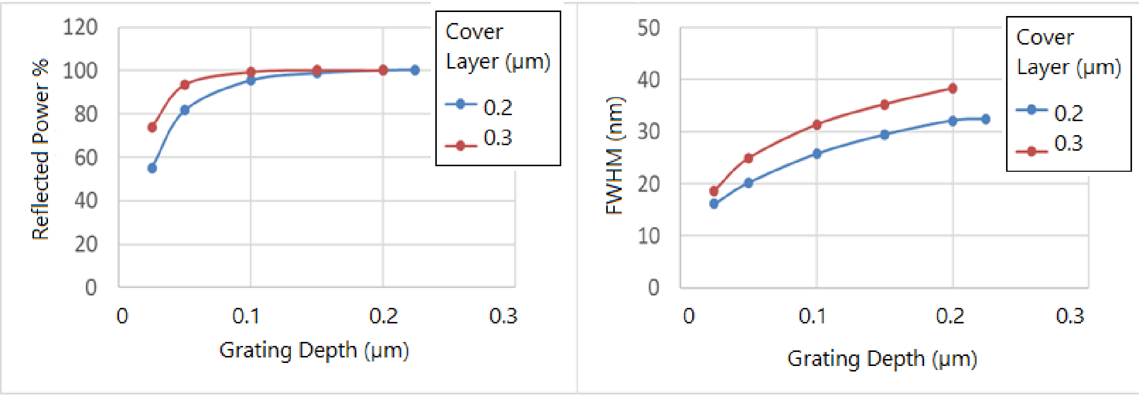

Figure 54. Maximum a) reflected power and b) reflectivity spectral width as a function of grating depth for different cover layer thicknesses for a 25µm long grating for Case 8.

As for the cover layer thickness, once using a 0.2µm deep grating, increasing the cover layer increases the reflected power and spectral width to a certain point until it reaches ~0.4µm cover layer and afterwards it drops as shown in Figure 55.

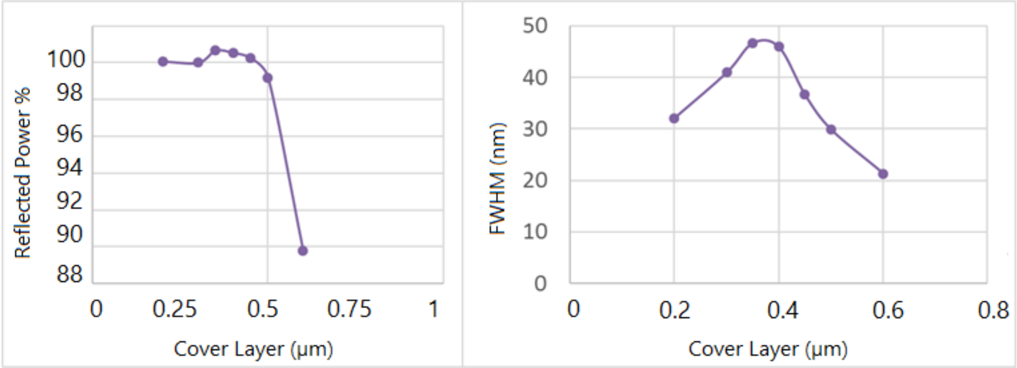

Figure 55. Maximum a) reflected power and b) reflectivity spectral width as a function of cover layer thickness for a grating with 0.2µm grating depth and 25µm grating length for Case 8

A combination of Case 6 and Case 8 was selected for fabrication of this device while using different lengths to achieve certain reflectivity for front and back mirrors of the DBR laser which will be presented in the next chapter.

4.2.2. Exploring Location of the Second-order Grating Out-coupler

The grating out-coupler needs high out-coupled power as opposed to high reflection for the mirrors which is achieved at second Bragg condition. This means the grating period Λ_{2nd} should be designed in a way that it satisfies the second Bragg condition ($\Lambda_{2nd} = \lambda_0/n_{eff}$). In the previous section, the optimized simplified structure was explored to achieve high out-coupling which showed an ECSNL-like structure where grooves are filled with SOG, cover layer is ~0.2µm and duty cycle is 50% gives the highest out-coupling. That said, using the same structure, the placement of the grating layer is explored here for the full epi stack shown in Table 1.

Figure 56 shows the power distribution and real and imaginary part of the propagation constant as a function of wavelength for Case 1 when grating is placed in layer 12, cover layer is set at 0.19µm, grating depth is 0.1µm and grating length is 10µm. Maximum out-coupled power in this case is 61%.

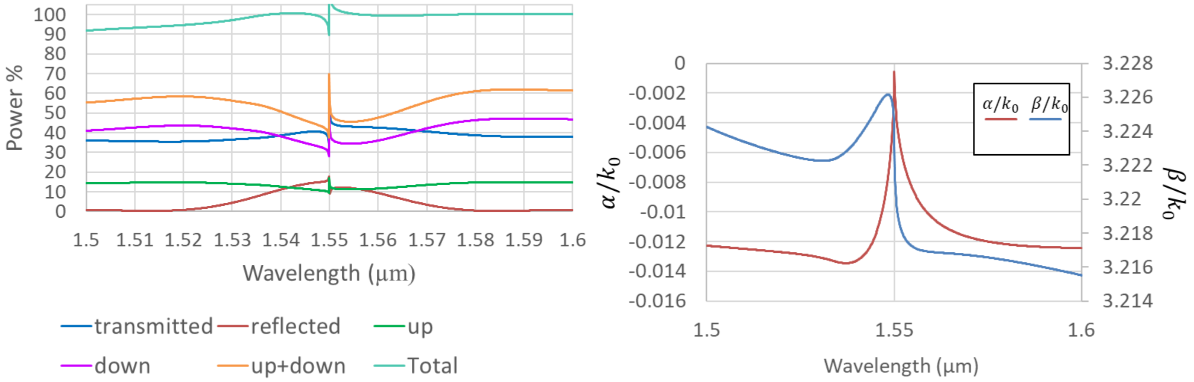

a) b)

Figure 56. Case 1 when the grating is placed in layer 12: a) Power distribution and b) normalized attenuation constants as a function of wavelength, for 0.1um grating depth, 0.19µm cover layer thickness and 10µm grating length

In Case 2, the grating is etched into layer 13 while the rest of the parameters are the same as described for Case 1. Figure 57 shows the power distribution and normalized attenuation constant as a function of wavelength for Case 2. In this case, maximum out-coupled power is 61.9%.

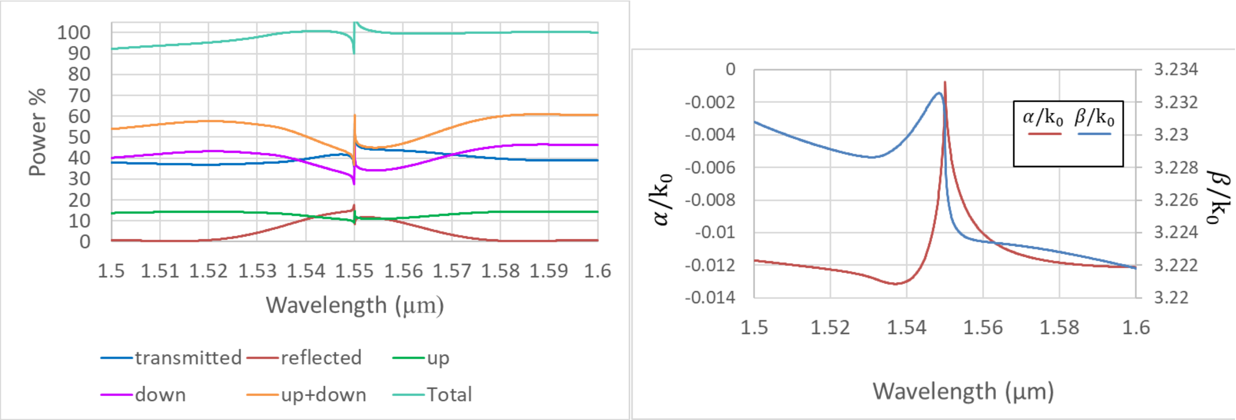

a) b)

Figure 57. Case 2 when the grating is placed in layer 13: a) Power distribution and b) normalized attenuation constants as a function of wavelength, for 0.1um grating depth, 0.19µm cover layer thickness and 10µm grating length

Next is Case 3 where the grating is placed in layer 14. Figure 58 shows the power distribution and normalized attenuation constants as a function of wavelength for Case 3. maximum out-coupled power in this case is 62.01%.

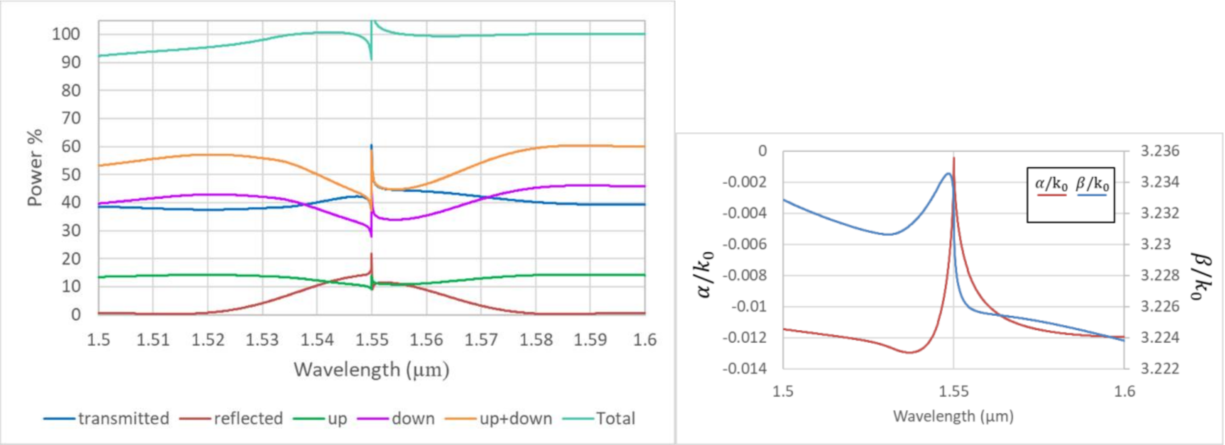

a) b)

Figure 58: Case 3 when the grating is placed in layer 14: a) Power distribution and b) normalized attenuation constants as a function of wavelength, for 0.1um grating depth, 0.19µm cover layer thickness and 10µm grating length

Placing the grating in layer 14, Case 4 results in power distribution and attenuation constant shown in Figure 59. The maximum out-coupled power in this case is 57.75% with the minimum for normalized attenuation constant showing a value of -0.012.

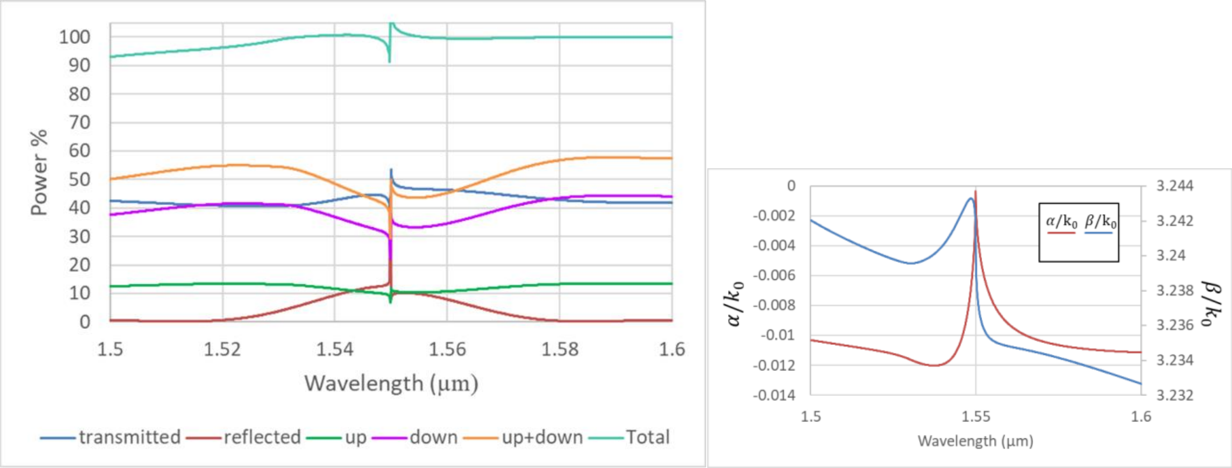

a) b)

Figure 59. Case 4 when the grating is placed in layer 15: a) Power distribution and b) normalized attenuation constants as a function of wavelength, for 0.1um grating depth, 0.19μm cover layer thickness and 10μm grating length

Next is Case 5 where the grating is placed in layer 16. Figure 60 shows the power distribution and the normalized attenuation constant as a function of wavelength where maximum out-coupled power is 49.16%.

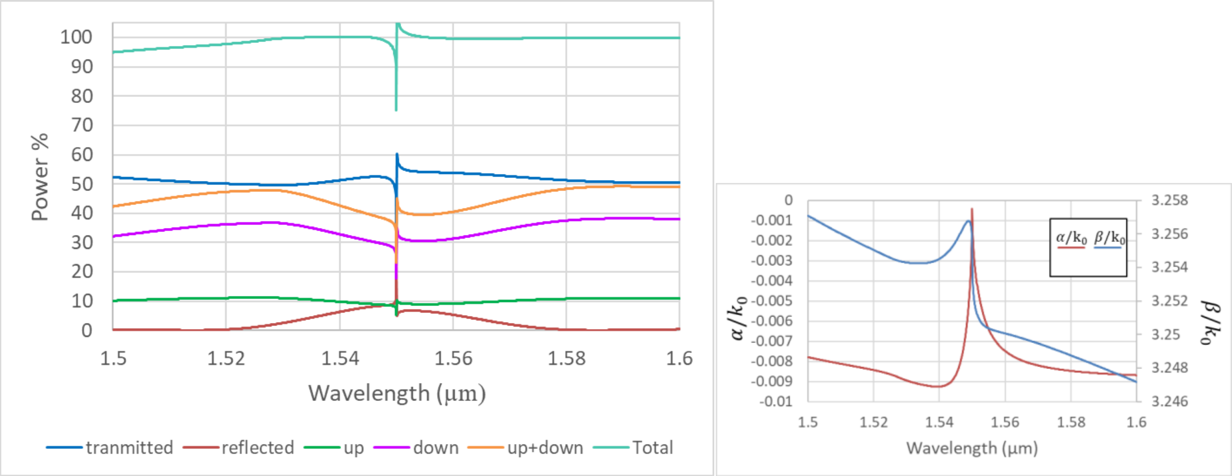

a) b)

Figure 60. Case 5 when the grating is placed in layer 16: a) Power distribution and b) normalized attenuation constants as a function of wavelength, for 0.1um grating depth, 0.19µm cover layer thickness and 10µm grating length

Next is Case 6 where grating is placed in layer 17. Figure 61 shows the power distribution and the normalized attenuation constant as a function of wavelength for this case where maximum out-coupled power is shown to be 38.1%.

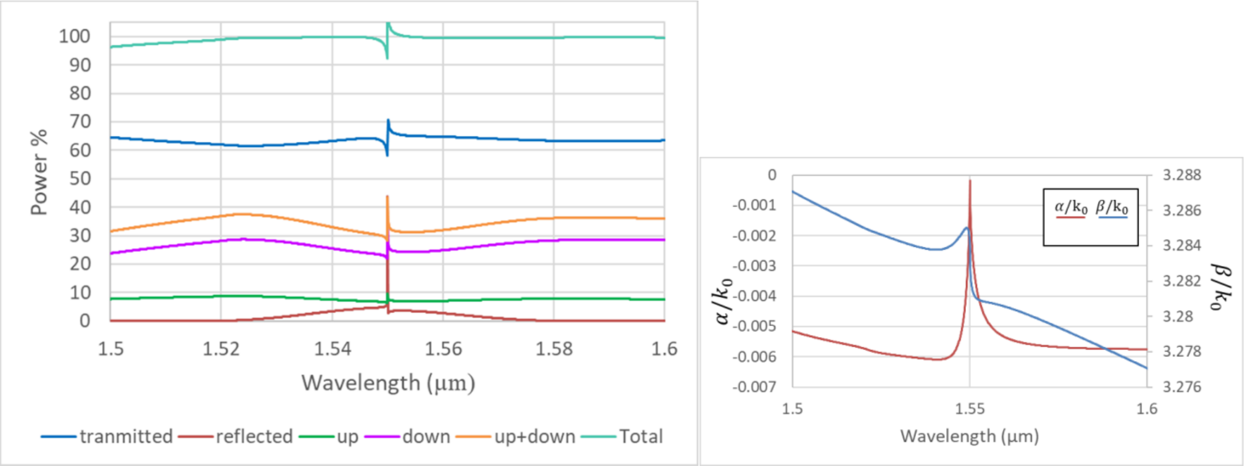

Figure 61. Case 6 when the grating is placed in layer 17: a) Power distribution and b) normalized attenuation constant as a function of wavelength, for 0.1um grating depth, 0.19µm cover layer thickness and 10µm grating length

Figure 62 compares the out-coupled power as a function of wavelength for different cases over a 100nm span of wavelength for a grating with 0.19µm cover layer, 50% duty cycle and 10µm long. The spike in the central frequency 1.55µm is due to numerical analysis restrictions and is not considered when comparing the maximum out-coupled power. Case 3 produces the maximum out-coupled power overall and it reaches 62.01% at its peak. This is ~35% more than the out-coupling a conventional grating with similar layers produces at 10µm length.

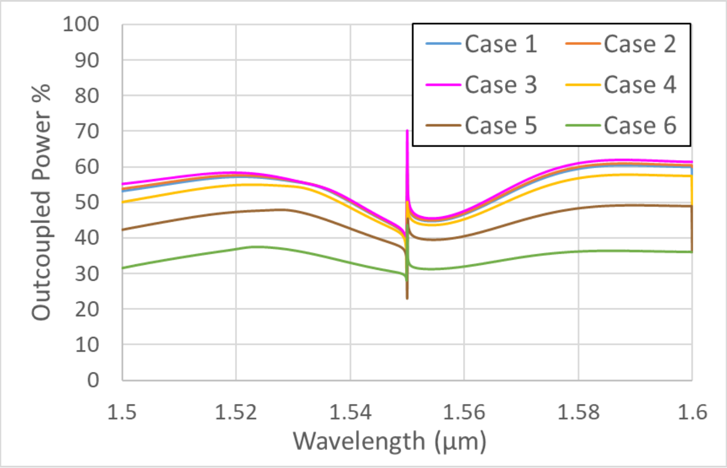

Figure 62. Out-coupled power as a function of wavelength for different cases where grating sits on different layers for grating length of 10µm and cover layer of 0.19µm and 50% duty cycle.

Figure 63 (a) shows that the attenuation constant for Case 3 is at its lowest which makes it more desirable to be used as a second-order grating out-coupler.

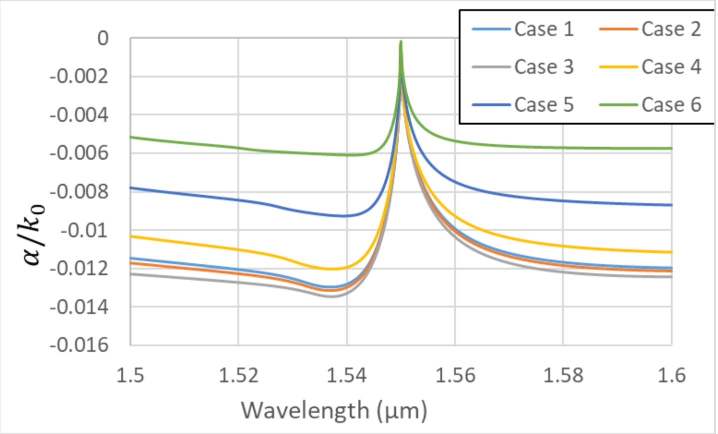

Figure 63. Attenuation constant as a function of wavelength for different cases where grating sits on different layers for grating length of 10µm and cover layer of 0.19µm and 50% duty cycle

Maximum out-coupled power each case produces is shown in Figure 64 shows the maximum out-coupled power each case produces.

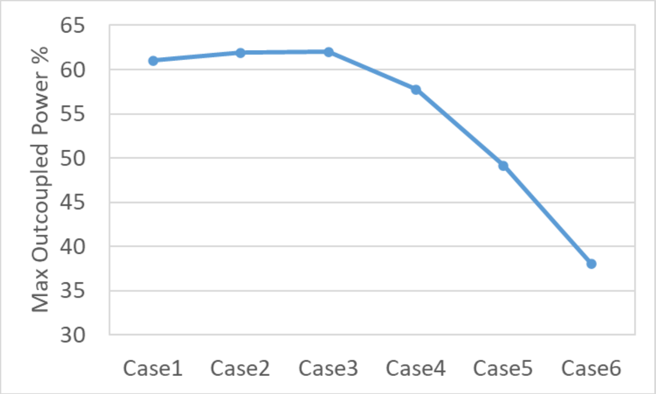

Figure 64. Maximum out-coupled power for different cases indicating different placement of grating. In all cases, the grating depth is 0.1µm, grating length is 10µm, duty cycle is 50% and cover layer is 0.19µm.

A comparison between Case 3 structure defined above and a conventional DBR with the same epi layers and structure (basically Case 3 without the filled grooves and no cover layer) is shown in Figure 65 where the bottom of the grating is placed on top of layer 14 and length of the grating is 10µm. Adding the low index SOG fill and 0.19um cover layer improves the out-coupled power by 115%.

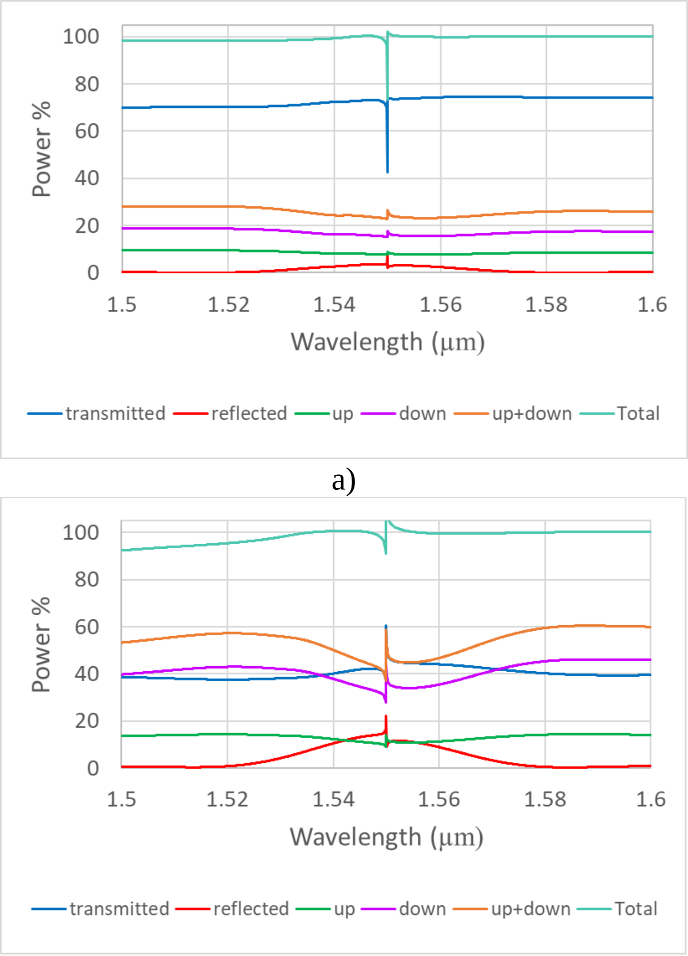

a)

b)

Figure 65. Power distribution for 10µm long, 0.1µm deep grating on layer 33 for a) conventional grating out-coupler and b) ECSNL out-coupler that has grooves filled with SOG topped with a 0.19µm cover layer.

Case 3 indicates the best layer to put the grating on which produces up to 62% out-coupled power for a 10µm long grating. Increasing the grating length to 15µm, 20µm, 50µm and 100µm, increases the out-coupled power up to 75.2%, 84.3%, 98.7% and 100%, respectively as shown in Figure 66.

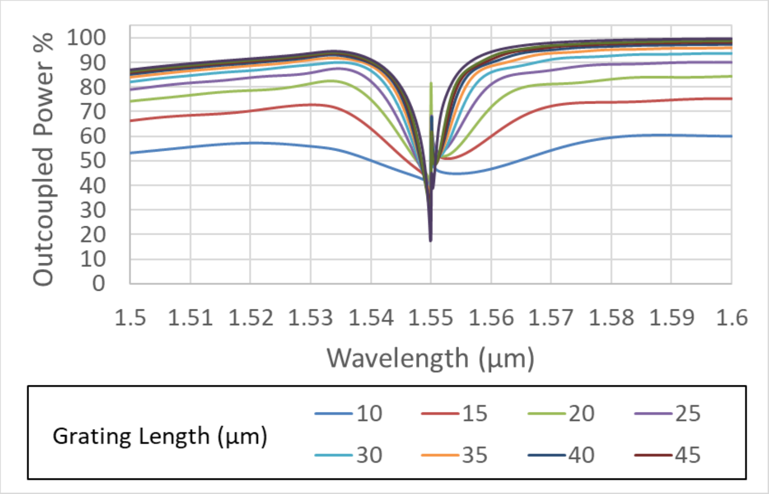

Figure 66. Out-coupled power for Case 3 with different grating lengths as a function of wavelength

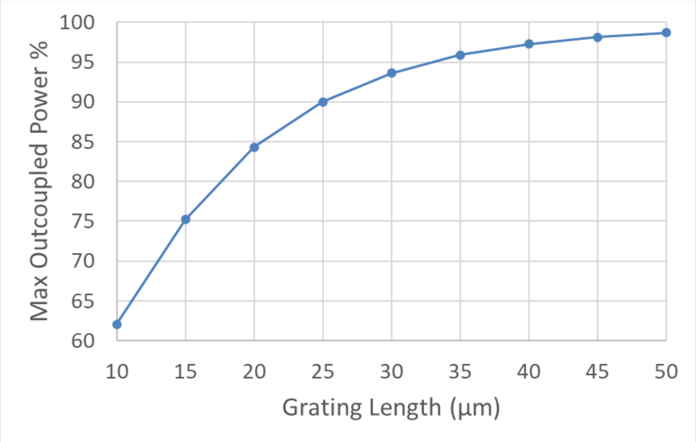

Figure 67. Maximum out-coupled power as a function of grating length for case 3

By increasing the grating length only to 26µm, the maximum power coupled out of this grating structure goes up to 90% as shown in Figure 67. This is ideal for an out-coupler that gives over

90% of output power while still long enough to not compromise the beam divergence. Beam divergence has a reverse relationship with the length of the out-coupler. For a 10µm long, 62% of the light can be coupled out. From 26µm to 50µm the outcoupling ranges from 90% close to 100% which is ideal for many different applications.

4.3. Experimental Results

4.3.1. Broad Area Laser Experimental Results

Figure 68 shows the broad area laser experimental results that were run on a 500µm long laser with the same epi stack as the one used for the Laser-EAM device at 1310nm. The LIV curve indicates a threshold current of 0.75A after which the voltage abruptly changes. From Eq. (2.23) and using the green curve indicating L-I curve, the external differential quantum efficiency can be found $\eta_d = 2\Delta P/\Delta I = 0.151W/A$.

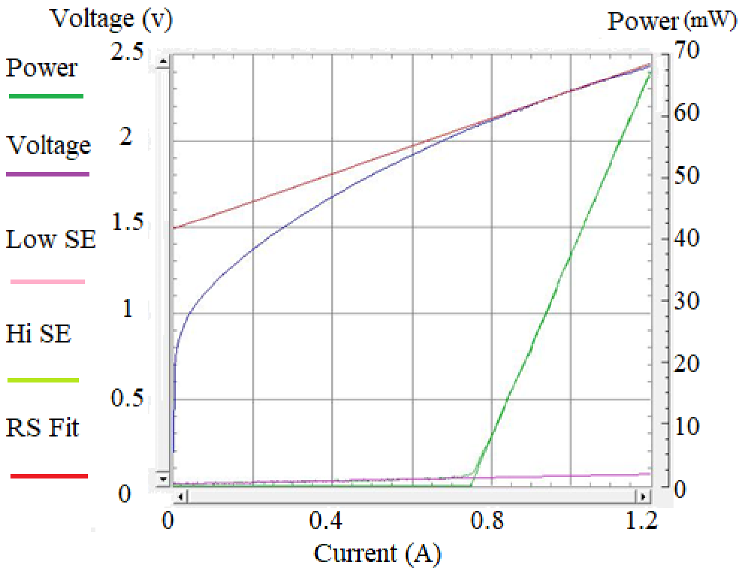

Figure 68. Optical power and voltage as a function of drive current (LIV curve) for a 100 µm wide as-cleaved 11 quantum well broad area laser with a length of 500 µm

Several lengths of BA Lasers were tested and the threshold current density as well as the threshold gain is reported in Table 4 using equations (2.23) and (2.24).

Table 4. Data analysis for broad area lasers

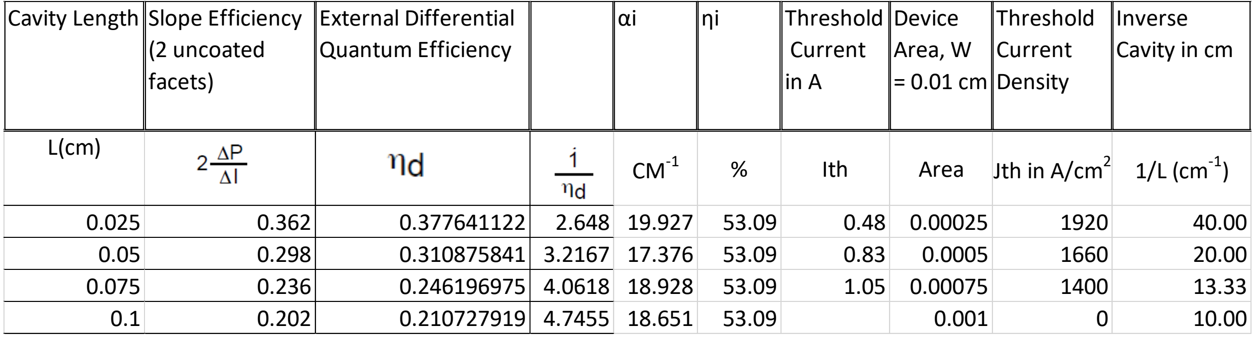

Cavity Length	Slope Efficiency (2 uncoated facets)	External Differential Quantum Efficiency		αi	ηi	Threshold Current in A	Device Area, W = 0.01 cm	Threshold Current Density	Inverse Cavity in cm
L(cm)	$2\frac{\Delta P}{\Delta I}$	η_d	$\frac{1}{\eta_d}$	CM^{-1}	%	Ith	Area	Jth in A/cm^2	1/L (cm^{-1})
0.025	0.362	0.377641122	2.648	19.927	53.09	0.48	0.00025	1920	40.00
0.05	0.298	0.310875841	3.2167	17.376	53.09	0.83	0.0005	1660	20.00
0.075	0.236	0.246196975	4.0618	18.928	53.09	1.05	0.00075	1400	13.33
0.1	0.202	0.210727919	4.7455	18.651	53.09		0.001	0	10.00

Threshold current density is decreasing the longer the laser gets as expected. However, due to the thin metal layer on top, uniform current was not applied along the longer wavelength and the decrease is less than expected. In future works the metal stack should be thick enough to ensure uniformity of applied current. Table 5 shows the threshold gain calculated using Eq. (2.22) for different laser length when R_1 and R_2 the front and back mirrors were set at low values of 0.9, 0.6 and high values of 0.99, 0.8 reflectivity respectively. Data was calculated for each laser length separately since internal loss η_i is different in each case. Maximum threshold gain is achieved when $R_1 = 0.9$ and $R_2 = 0.6$ for each case.

Table 5. Threshold gain for different laser length for different reflectivities

	40µm long ridge	100µm long ridge	80µm long ridge	175µm long ridge	
g_{th} for 250µm laser	96.95073743	50.73677697	58.43910371	37.53278827	R1lowR2low
	60.99047837	36.35267335	40.45897419	29.31330048	R1lowR2high
	85.03696495	45.97126798	52.48221748	34.80964027	R1highR2low
	49.0767059	31.58716436	34.50208795	26.59015249	R1highR2high
	40µm long ridge	100µm long ridge	80µm long ridge	175µm long ridge	
g_{th} for 500µm laser	94.39970743	48.18574697	55.88807371	34.98175827	R1lowR2low
	58.43944837	33.80164335	37.90794419	26.76227048	R1lowR2high
	82.48593495	43.42023798	49.93118748	32.25861027	R1highR2low
	46.5256759	29.03613436	31.95105795	24.03912249	R1highR2high
	40µm long ridge	100µm long ridge	80µm long ridge	175µm long ridge	
g_{th} for 750µm laser	95.95089743	49.73693697	57.43926371	36.53294827	R1lowR2low
	59.99063837	35.35283335	39.45913419	28.31346048	R1lowR2high
	84.03712495	44.97142798	51.48237748	33.80980027	R1highR2low
	48.0768659	30.58732436	33.50224795	25.59031249	R1highR2high
	40µm long ridge	100µm long ridge	80µm long ridge	175µm long ridge	
g_{th} for 1000µm laser	95.67459743	49.46063697	57.16296371	36.25664827	R1lowR2low
	59.71433837	35.07653335	39.18283419	28.03716048	R1lowR2high
	83.76082495	44.69512798	51.20607748	33.53350027	R1highR2low
	47.8005659	30.31102436	33.22594795	25.31401249	R1highR2high

The optical spectrum of a laser is a function of the characteristics of the gain media and usually have multiple peaks over a range of spectrum [19]. Using an optical spectrum analyzer, the pulse measurement at room temperature showed that 11-QW broad area has a central frequency at 1290.98nm as shown in Figure 69. This central frequency is temperature sensitive. In order to analyze the frequency shift due to change of temperature, this measurement must be done at different temperatures which is a future work to do.

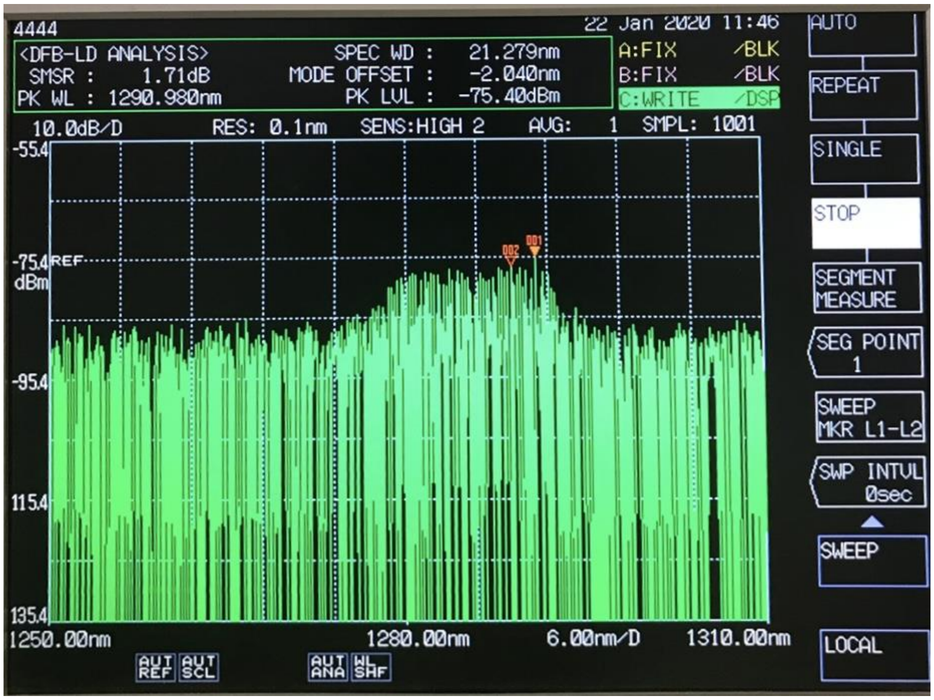

Figure 69. Pulsed measurement for a 500µm long broad-area laser around wavelength ~1.3µm at room temperature.

4.3.2. DC Test Results

Upon finishing the fabrication of the devices and cleaving them, DC test was performed on the lasers both in forward and reverse bias regime to get the I-V curves for each case to determine the series resistance, reverse leakage, turn-on point and the breakdown voltage. The differential series resistance of the laser can be determined from the derivative of the applied voltage vs current. Figure 70 shows the I-V curve of a cleaved 150µm long ridge laser when connected in series with 8kΩ resistor in forward and reverse bias.

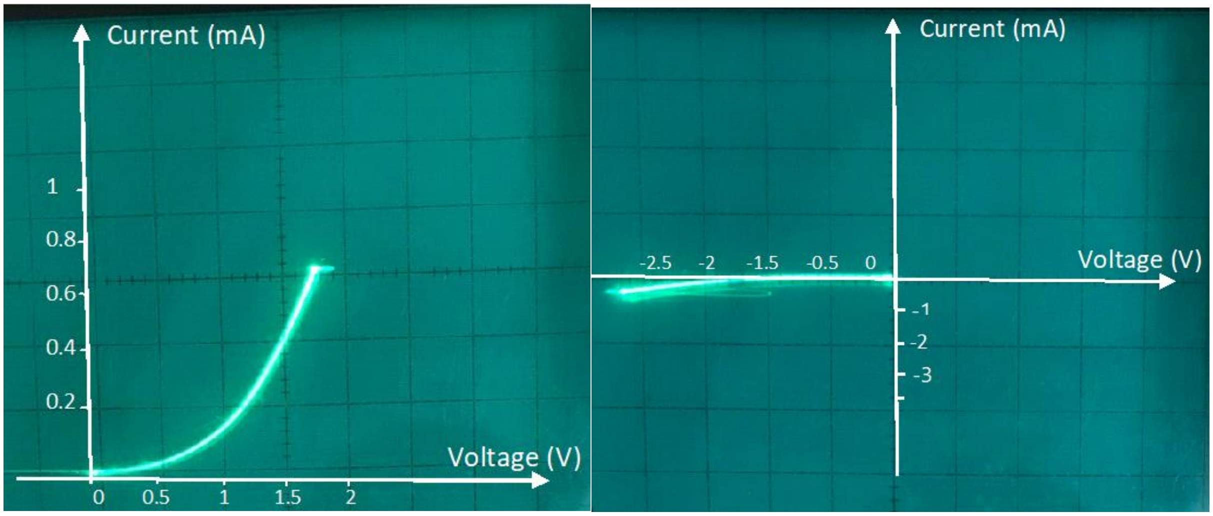

a) b)

Figure 70. I-V curve of a cleaved 150µm long ridge laser with 8kΩ series resistor in a) forward and b) reverse bias

Figure 71 shows the I-V curve of the same laser when it is in series with a 2kΩ resistor.

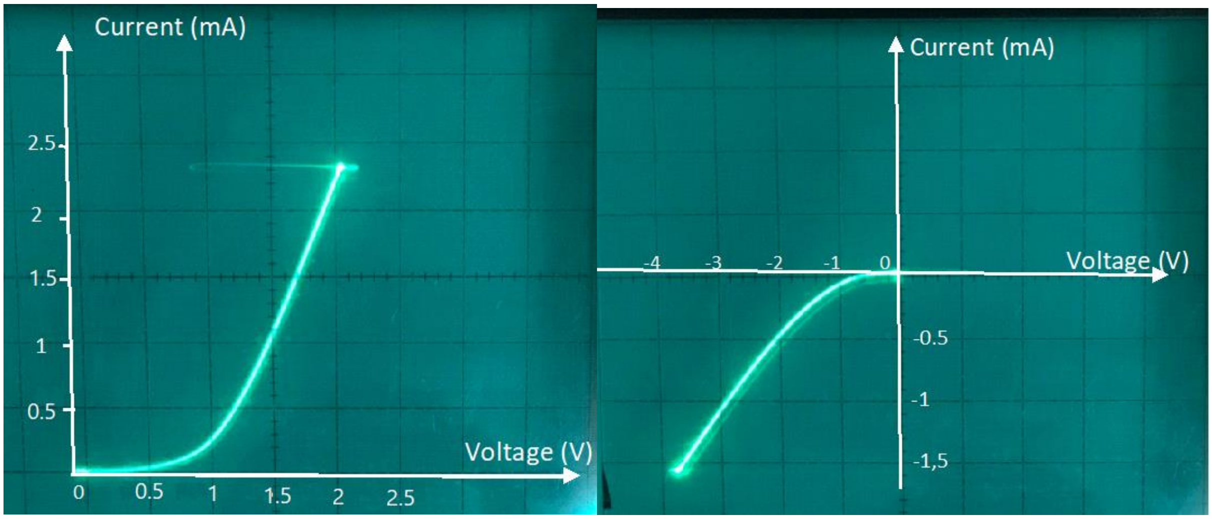

a) b)

Figure 71. I-V curve of a 150µm ridge guide laser in forward bias with a series resistor of 2kΩ

Figure 72 shows the same laser when 6.5V voltage is applied to the p-contact pad and is attached to a series resistance of 0.5kΩ.

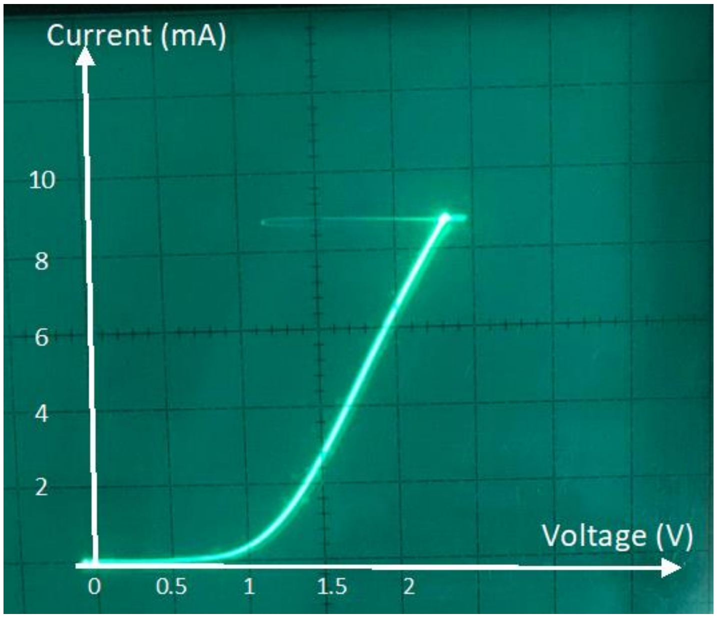

Figure 72. I-V curve of a forward biased 150μm cleaved ridge guide laser with a 6.5V applied voltage and a series resitance of 0.5kΩ

Chapter 5

MASK DESIGN, FABRICATION AND PROCESSES

5.1. Mask Design

The first step in designing a mask is discerning the smallest feature size needed in the structure. Based on that, a parameter called the database unit is selected. The design outlined here required a quarter micron of accuracy; therefore, the database unit was chosen to be 0.25μm. Then starting from the lowest level, a designer begins designing the unit cell that needs to be repeated all across the mask. A designer can define different cells on the same level to be repeated as often as they wish. For this project KLayout mask design software is used. KLayout provides an option to define different levels of hierarchy in a “cells” column as shown in Figure 73. To make the process of design easier, a designer must begin with the first layer that has to be patterned on the epitaxial structure. In this case the first step is to define the InP ridges. To do so, a designer starts by defining a layer by right clicking on the right panel shown in Figure 73. Then a designer chooses a name and layer number. Only then they are able to start with designing the pattern. After selecting the layer on the right panel, a designer chooses the “box” icon on the top panel and draws a box. Double clicking on this box item, enables the designer to edit the size of the box as well as the precise location. If the designer needs to delete part of the pattern, for instance if they want a hollow rectangle inside the defined box, they have to change the icon “add” on the top panel to “erase”.

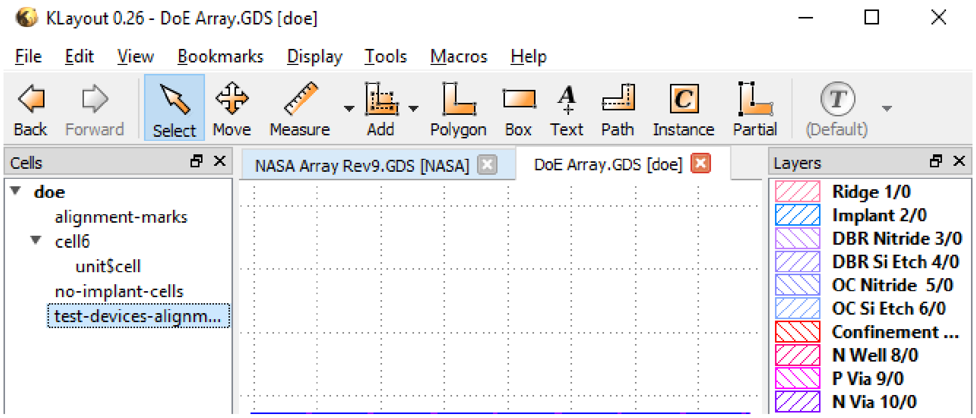

Figure 73 KLayout mask designer user interface

Afterwards, the design is continued for each mask layer step by step until the design of an entire cell is finished as shown in Figure 74. As shown, this includes the laser-EAM ridges, DBR grating front and back mirrors and grating out-coupler with corresponding layers defined for each component.

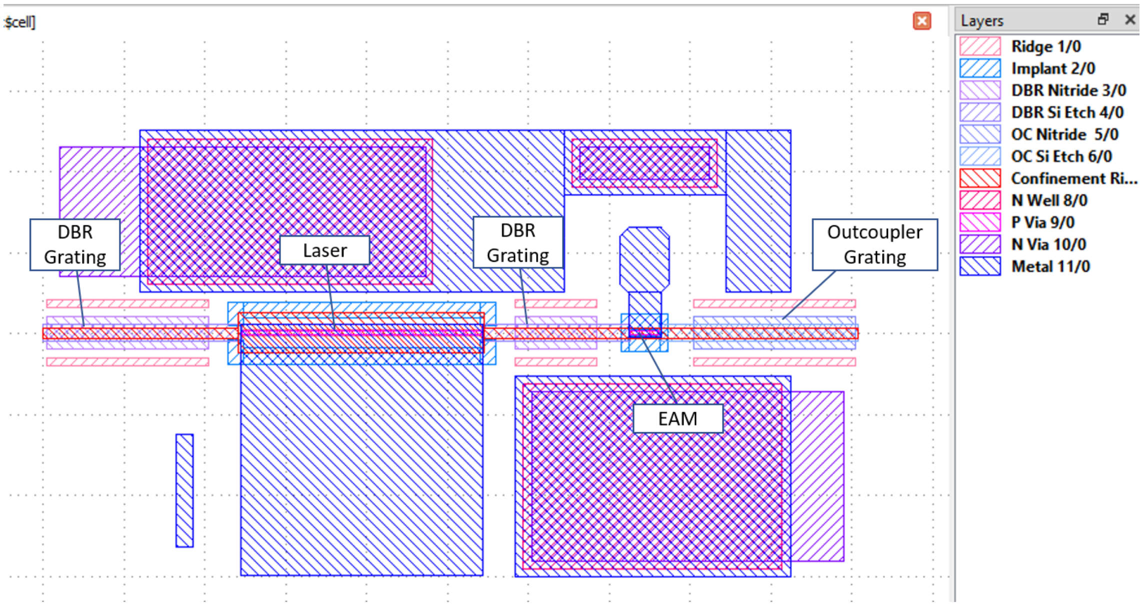

Figure 74. Elements of the integrated laser/modulator design

This mask set includes 11 mask layers. Often, especially when developing and testing a new design, it is desirable to have a "rainbow" mask to alter some parameters in each cell in order to have a variety of different designs to test.

The rainbow structures used were to vary the laser length, EAM length, DBR mirrors length and the ridge width as shown in Table 6.

Table 6. Different rainbow designs used for the DoE project

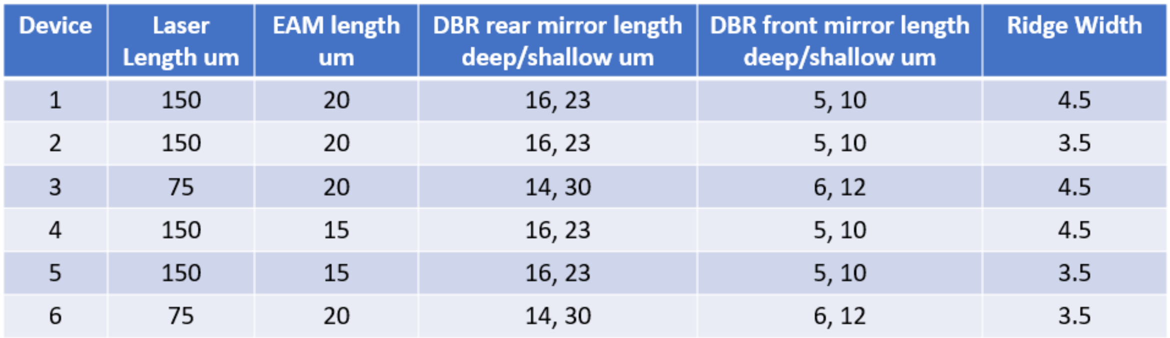

Device	Laser Length um	EAM length um	DBR rear mirror length deep/shallow um	DBR front mirror length deep/shallow um	Ridge Width
1	150	20	16, 23	5, 10	4.5
2	150	20	16, 23	5, 10	3.5
3	75	20	14, 30	6, 12	4.5
4	150	15	16, 23	5, 10	4.5
5	150	15	16, 23	5, 10	3.5
6	75	20	14, 30	6, 12	3.5

Once all the variations of rainbow structures are defined within the cell, it was decided to add several more structures with only lasers or EAMs for easy cleaving and testing purposes as well as some process monitors on top of each cell to be used to monitor the quality of process at each step and at the end to see how well the fabrication process is implemented. Figure 75 shows the unit cell that includes all the above-mentioned variations.

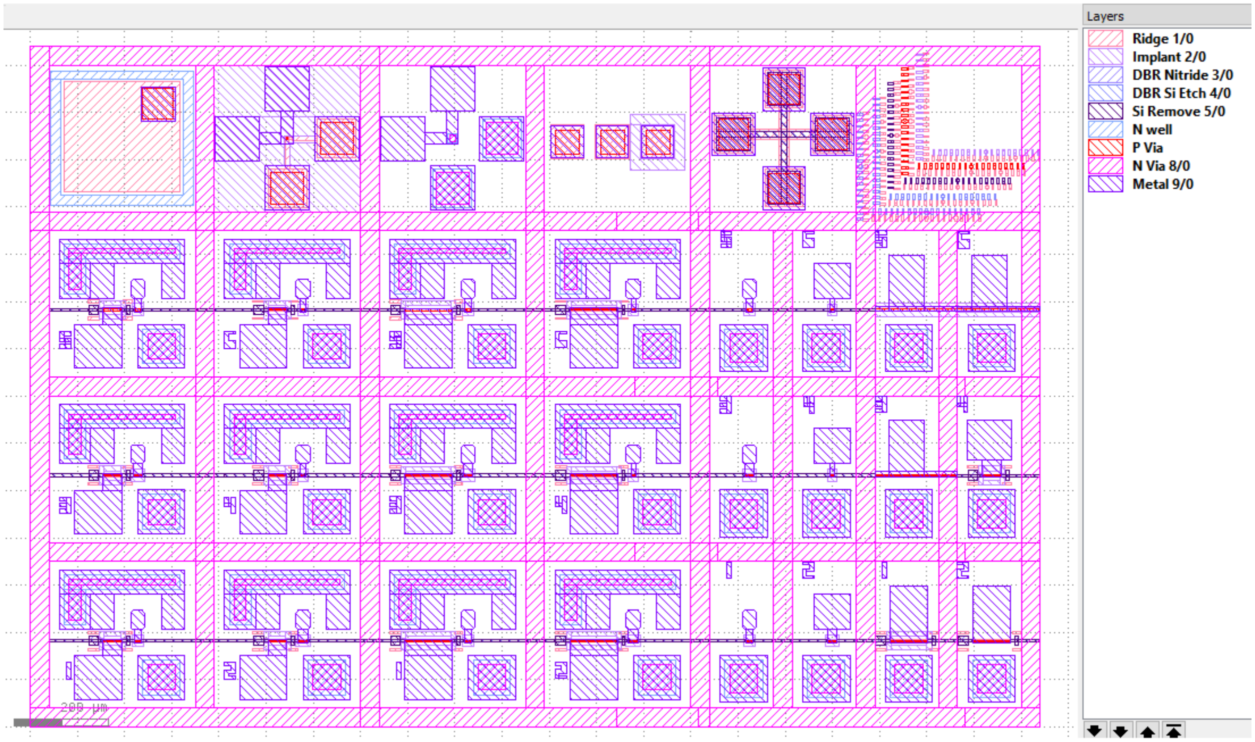

Figure 75. Unit cell including 12 sets of Laser-EAM cells, 6 Laser-only cells and 6 EAM-only cells on the right and process monitors and vernier on the top row.

Once the design of all variations is done, it can be defined as a cell in KLayout to be repeated on a higher hierarchy as shown in Figure 76.

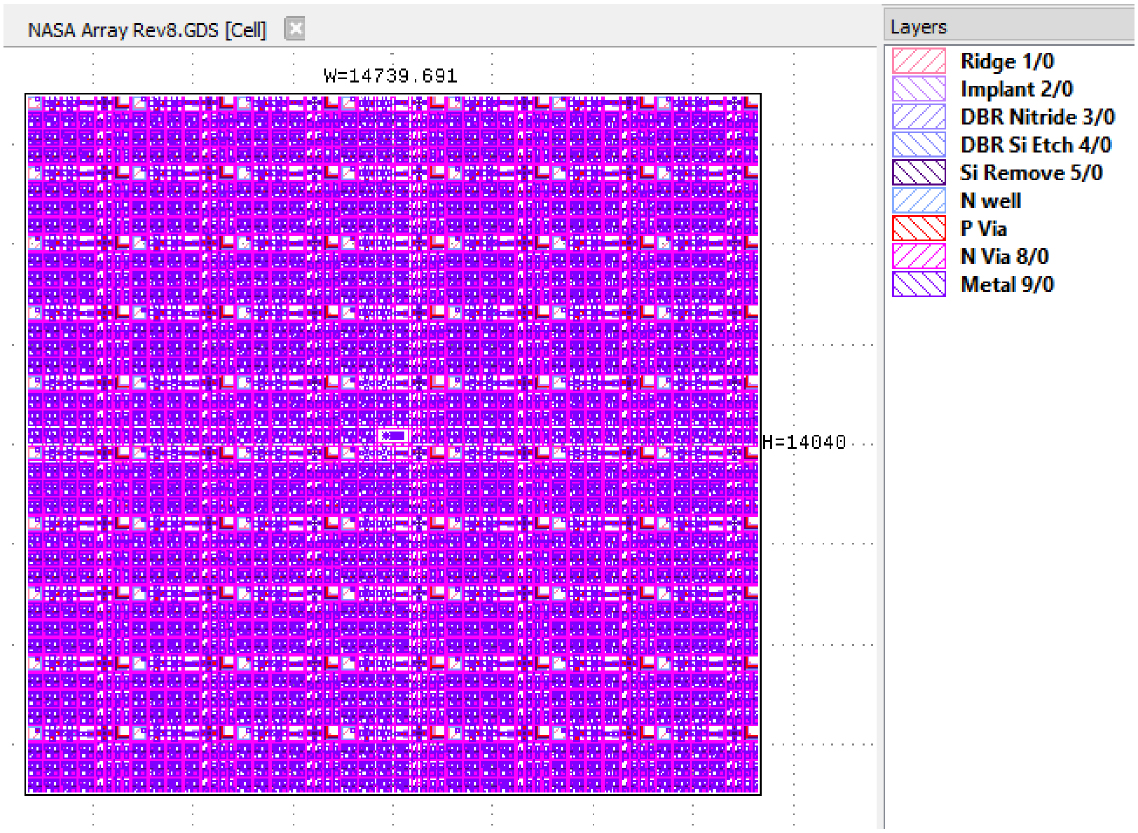

Figure 76. Step and repeat cell (dimensions in micron)

In the next section the process monitors are discussed to explain the purpose of each structure as well as its design.

5.1.1 Process Monitors

Process monitors are structures designed within active dies to monitor the effectiveness and quality of each layer or process step including the isolation provided by the implant layer and the resistance each layer undergoes as well as the quality of the contacts. There are certain standard structures that are used widely in semiconductor industry among which three types of them were chosen to be used in this project. The first structure is called *Cross-Bridge Kelvin Resistor* (CBKR) shown in Figure 77 that is used to evaluate the metal to semiconductor contact.

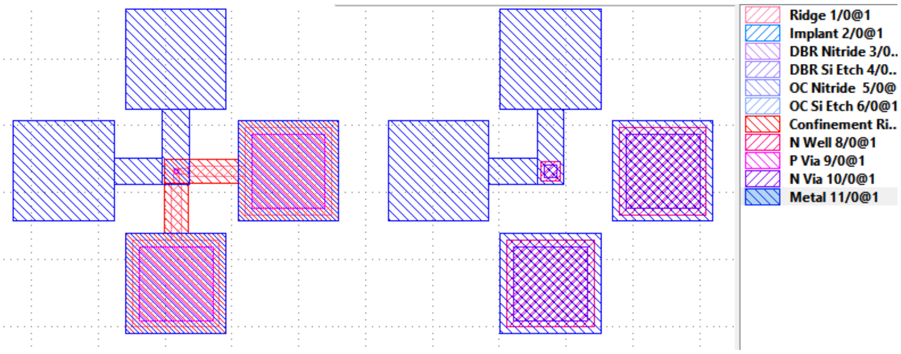

a) b)

Figure 77 Test structures for measuring a) p-contact resistance b) n-contact resistance Cross-Bridge Kelvin Resistor test structure

When performing Cross Bridge test Ohm's law is used by applying a current to the probe 1 structure and read the voltage across probe 2 and 4 as shown in Figure 78. The specific contact resistance $\rho_c = R_c . A$ where A is the contact area. The measured R_k is the sum of contact resistance and the resistance due to the current flow around the contact in the overlap region. The specific contact ρ_c can be extracted from Eq. (5.1) where R_{sh} is the sheet resistance of the underlying layer.

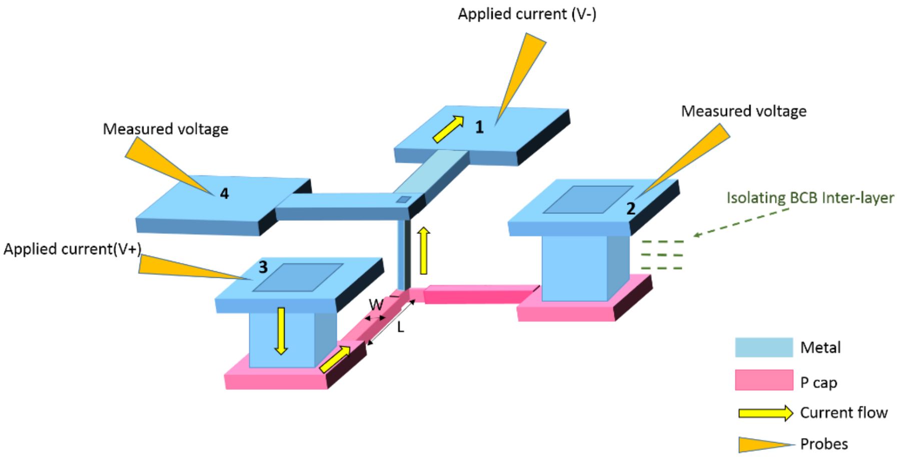

Figure 78 Cross bridge test steup for measuring n and p- contact resistance.

Figure 79 shows the same structure with dimensions defined as parameters used in Eq. (5.1) for resistance R_k. This formula indicates the relationship between the sheet resistance (Ω) to resistance where ρ_c is the specific contact resistance with a unit of (Ω-cm^2).

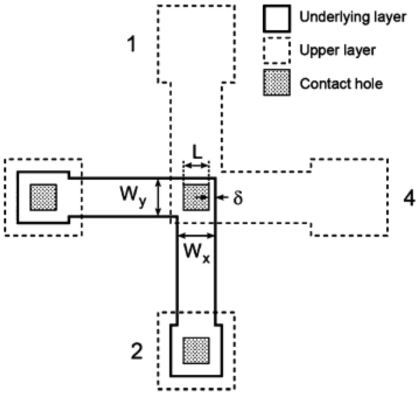

Figure 79 Four terminal CBKR structure with geometry parameters definition [50]

$$R_k = \frac{\rho_c}{A} + \frac{4R_{sh}\delta^2}{3W_xW_y}\left[1 + \frac{\delta}{2(W_x - \delta)}\right] \tag{5.1}$$

A modified curve tracer at SMU was used to perform this test. The stage was used to ground the n-contact since the top n-metal deposition was skipped for this phase. Table 7 and Table 8 show the calculated along with experimental results of the cross-bridge test for p-contact and n-contact, respectively. The p specific contact resistance turned out to be as expected for one out of the two wafer pieces that was at hand (1.75E-08 Ω-cm^2). However, the n-contact specific resistance was too high for the same wafers which was expected.

Table 7. Cross-Bridge test results for p-contact for wafer 1 and 2

	Width (cm)	Area (cm^2)	Expected ρ_c(Ω-cm^2)	Expected Resistance (Ω)	Applied current (A)	Expected voltage (V)	Measured Voltage (V)	Resistance (Ω)	ρ_c(Ω-cm^2)
Wafer1	2.5E-04	6.25E-08	5.00E-08	8.00E-01	1.00E-02	8.00E-03	6.0E-1	6.00E+01	3.75E-06
Wafer 2	2.5E-04	6.25E-08	5.00E-08	8.00E-01	1.00E-02	8.00E-03	2.80E-03	2.80E-01	1.75E-08

Table 8. Cross-Bridge test results for n-contact for wafer 1 and 2

	Width (cm)	Area (cm^2)	Expected ρ_c(Ω-cm^2)	Expected Resistance (Ω)	Applied current (A)	Expected voltage (V)	Measured Voltage (V)	Resistance (Ω)	ρ_c(Ω-cm^2)
Wafer1	1.00E-03	1.00E-06	1.00E-07	1.00E-01	1.00E-02	0.1	1.00E-02	2	2.00E+01
Wafer 2	1.00E-03	1.00E-06	1.00E-07	1.00E-01	1.00E-02	0.1	9.5	1	9.50E+02

Figure 80 shows the implant and isolation test structure used to characterize the contact resistance of the p-metal layer as well as the isolation provided by the implant. The four-point-probe method used in the previous process monitor requires 4 contacts to calculate the sheet resistance while reducing the effect of contact resistance. However, contact resistance is also an essential factor when analyzing electronic properties of CMOS devices to have a better understanding of how the device performance is affected by it. Contact resistance can be found by different measurement techniques. One of the most used techniques is the standard transferred length method (TLM) that uses a multiple of squares spaced out as shown in Figure 80.

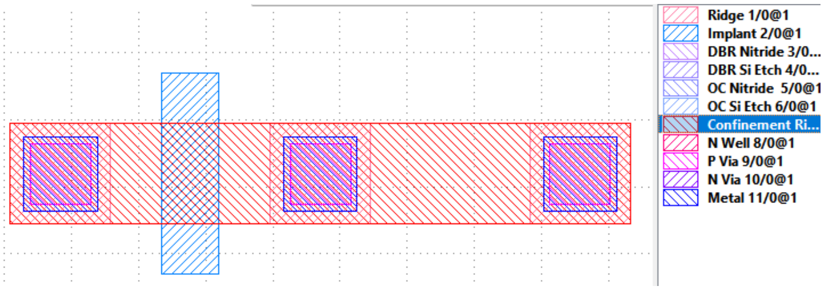

a)

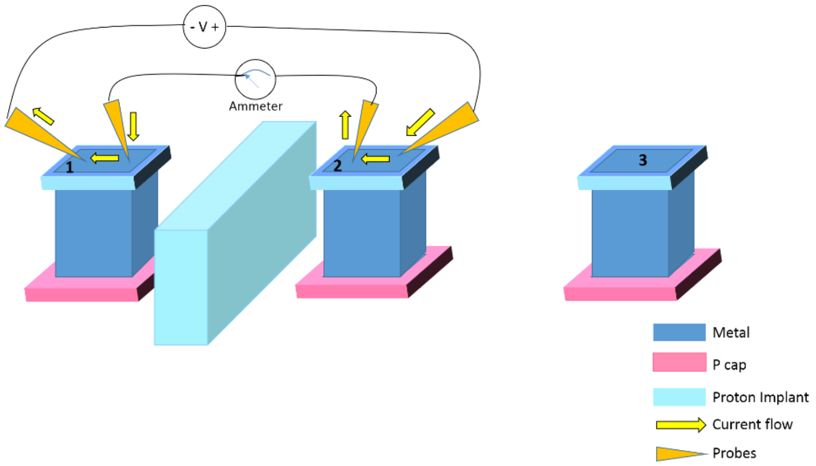

b)

Figure 80. a) process monitor structure used for measuring contact resistance, sheet resistance and testing the implant isolation and b) isolation test setup

Photodiode process monitor is designed as a big device, easy to probe to obtain the forward bias and reverse bias I-V curves for a diode, as shown in **Error! Reference source not found.**. A 3-D model of the photodiode and sketch of the test setup is shown in Figure 81. This test was performed at SMU using a modified curve tracer. Despite what is shown in Figure 81 where the n-contact pad is defined on the top, the n-metal deposition was skipped therefore n-contact was probed from the stage to the substrate. Figure 82 shows the I-V curves of the photodiode when it was (a) forward biased and (b) reverse biased.

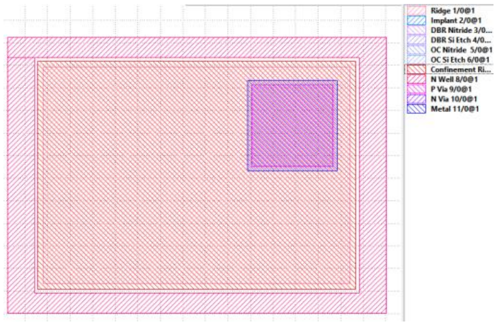

a)

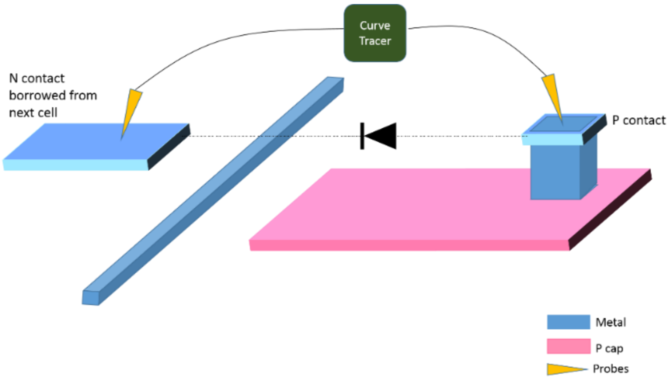

b)

Figure 81 a) Photodiode structure in the mask and b) I-V curve setup for the photodiode process monitor.

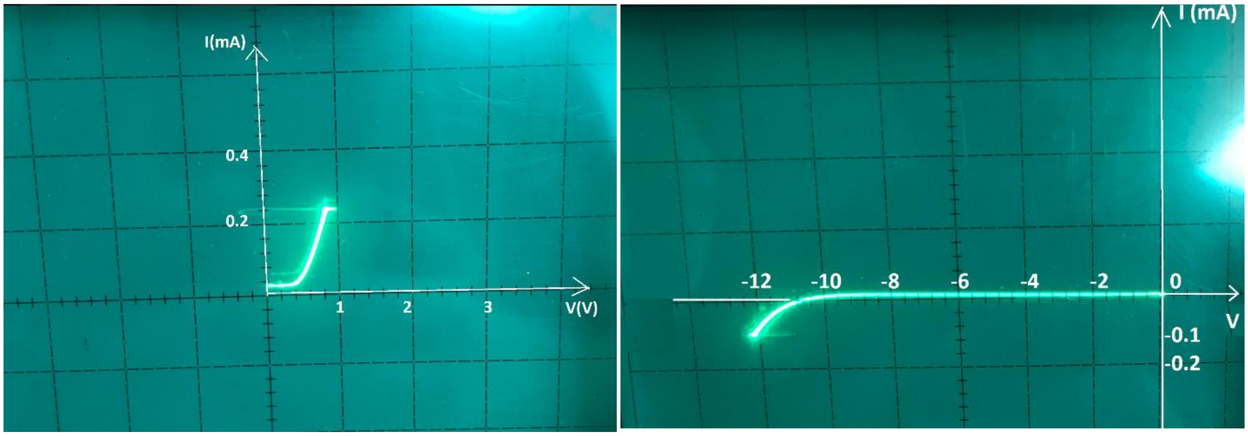

a) b)

Figure 82 I-V curves of a photodiode in a) forward bias and b) reverse bias

The I-V curves of the photodiode shows a break-down voltage of -11V when in reverse bias and a froward bias threshold voltage of 0.2V. The DC test results in general did not come out as satisfactory due to process issues. However, these results were used to modify the process steps to ensure better performance for the next phase of the project.

5.2 Fabrication and Processes

Process flow for 1310 project funded by DOE was done partially at SMU clean room and UCSB nanofabrication cleanroom. First step was to cleave 3” wafers into quarter pieces followed by depositing a sheet of silicon nitride everywhere on the wafer using PECVD system in Figure 83. The silicon nitride layer with a target thickness of 1200 Å was selected to be deposited under these conditions: He = 250sccm, N_2=500sccm, SiH_4=50sccm, under pressure of 600mTorr, and with a 70W RF.

Figure 83 PECVD system at SMU cleanroom

5.2.1. Ridges

After putting down the nitride layer, the next step was photolithography for the first mask layer, Ridge as shown in Figure 84. The purpose of putting dummy ridges where the gratings will sit later is to smoothen the photoresist around the grating when it comes to patterning the grating using holography method.

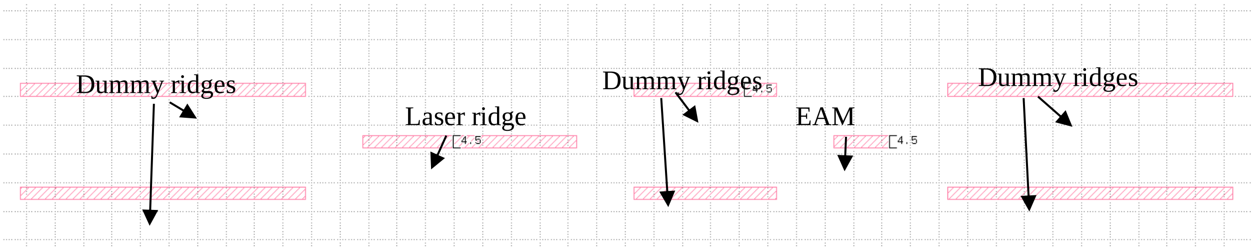

Figure 84. First mask layer, Ridge, to define laser, EAM and dummy ridges

The width of the ridge is alternating between $3.5\mu m$ and $4\mu m$ which makes the choice of photoresist very critical. A target thickness of $1.35\mu m$ for the photoresist was selected in order to achieve this. Shipley resists S1813 was spun at 4500 RPM for 30 seconds followed by 60 seconds of soft bake at $100°C$. Usually when processing quarter piece wafers, one will end up with extra photoresist on the edges which has to be carefully removed using a q-tip soaked with acetone.

Next, an MJB3 Karl Suss mask aligner was used to align the flat to one of the flat lines on the mask and expose for 13 seconds at 194 Watts through the mask. Then wafer pieces were developed in AZ MF-26A developer for 45 seconds were rinsed with DI water and blow dried with nitrogen. At this point patterning the first mask was completed and an inspection was required to make sure the wafer was completely developed and the ridges came out clearly. After this step, an oxygen ash was required at 500 mT, 100 W, for 1 minute to make sure the surface is free from any organic material including leftover photoresist.

Next, the silicon nitride was removed from the ridges while it remained everywhere else. The Oxford RIE system was used to etch the SiN layer under these conditions: CF_4/O_2, 190 mT, 100W. The etch time was 15-16 minutes. After that a microscope and profilometer was used to measure the etch depth and inspection of complete nitride etch followed by another oxygen ash.

The next step was to remove the epi layers around the ridges (laser and EAM) to achieve the designated stack. For this, a series of wet etches were performed to remove the InGaAs/InGaAsP cap layer. First, the wafer was dipped into buffered hydrofluoric acid or BOE (10:1) for 1 second. Then, the etchant solution for InGaAs/InGaAsP H_2SO_4:H_2O_2:DI water (1:2:10) [51] was used at about 5°C for 15 seconds followed by rinsing with DI water for 60 sec and N2 dry. Next, profilometer was used to Measure the etched depth. The etch and measure steps were repeated for an additional 2 sec etch time until the depth of etch indicated reaching to the etch stop layer. Afterwards, the photoresist was stripped off the wafer using acetone followed by isopropyl alcohol (IPA).

A dry etch was then performed to remove the rest of the layers to etch 80% through InP layers ending in layer 16. This means a $1.2\mu m$ etch into the InP layer was required. The reactive ion etches or CH_4/H_2 RIE process was used to perform this etch. This process is proven to be best for etching very fine structures with features as small as $0.1\ \mu m$ to a depth of more than $1\mu m$ into GaInAsP. Using RIE for this step is specifically important due to its capability of directional etching while remaining highly anisotropic. RIE deploys a combination of physical and chemical reactions with the target to etch a specific material from it [52].

This dry etch is followed by another wet etch to remove the remaining InP cladding. The proper solution for this step is HCl: DI water: H_3PO_4 (12:3:5) etchant at about 5°C. There is an InGaAsP etch stop layer just below the InP cladding designed to avoid over-etching. At this point measuring the ridge height with profilometer should indicate around $1.6\mu m$ plus the height of nitride (1200 Å). The etch stop layer is then removed using H_2SO_4:H_2O_2:DI water (1:2:10) etchant at about 5°C for 15 seconds. Once the etch is complete, a final inspection and measurement was performed to make sure the height is correct before removing the nitride layer. A solution of BOE:DI water

(1:10) at room temperature was used for 90 seconds to remove the nitride layer and the height of the ridge was measured to show around $1.6 \mu m$. Figure 85 shows a picture taken under the microscope after this step, showing the ridges.

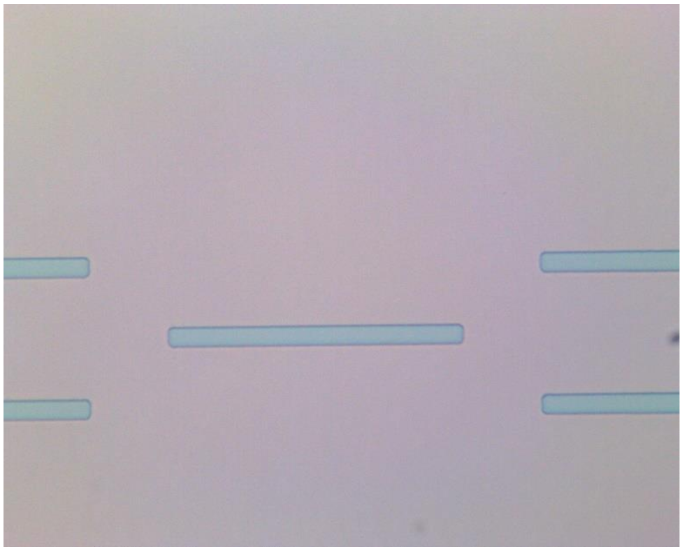

Figure 85. The laser and EAM ridges fabricated using silicon nitride mask and a combination of methane/hydrogen dry etch and wet etch to the epitaxial etch stop layer.

5.2.2. Ion Implant

Ion implantation was performed next, to provide isolation for laser and EAM ridges as shown in Figure 86. The Implant mask was designed to wrap around the EAM structure to provide complete isolation and reduce leakage to the minimum and was designed around laser ridge as two brackets.

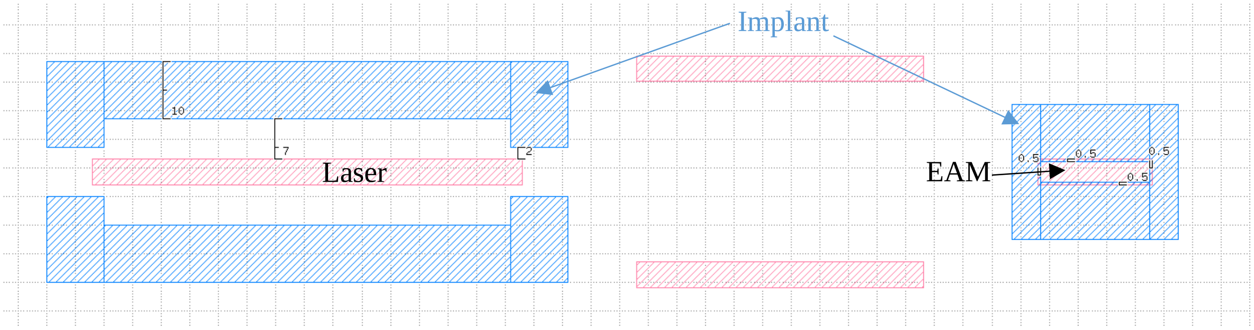

Figure 86. Mask layer 2, Ion Implant

The photolithography step for the wafers were performed at SMU cleanroom using the typical Shipley 1813 and MJB3 mask aligner to expose and develop the patters. Figure 87 shows an optical image of one laser structure after ion implantation photomask pattern. Ion implantation is performed in a low heat medium where ions of a selected element are accelerated into a target. The dose and energy of the ion is carefully calculated based on the damage is has on each layer of the epi structure. In compounds where the defect level is close to the conduction band as in AlInGaAs it is better not to overdo the implant because the defect level can be a deep dopant. Helium was used as a dopant with a dose of $5 \times 10^{13}/cm^2$ at 30 KeV. The wafers were then shipped to an implant facility to get the ion implantation.

Figure 87. Ion implant photomask pattern

Once the wafers were received after ion-implantation, photoresist was removed before moving onto the next step. At this stage, a shadowing effect was observed after removing the photoresist so there was a concern that the implant might have passed through the photoresist. However, isolation tests showed that this was not the case.

5.2.3. DBR and Outcoupler Gratings

The next step in this process was to deposit a layer of silicon nitride to be used as a mask for patterning the DBR grating windows. For this step a PECVD system was used followed by photolithography for the second mask, DBR nitride opening shown in Figure 88. Two mask sets (corresponding to case 6 and case 8) were designed and ordered to be used for DBR grating with different lengths to explore the results. The length of the grating was selected based on the designs explained in previous chapter to be $6\mu m$ and $12\mu m$ for the front mirror and $14\mu m$ and $30\mu m$ for the back mirror for case 6 and case 8, respectively.

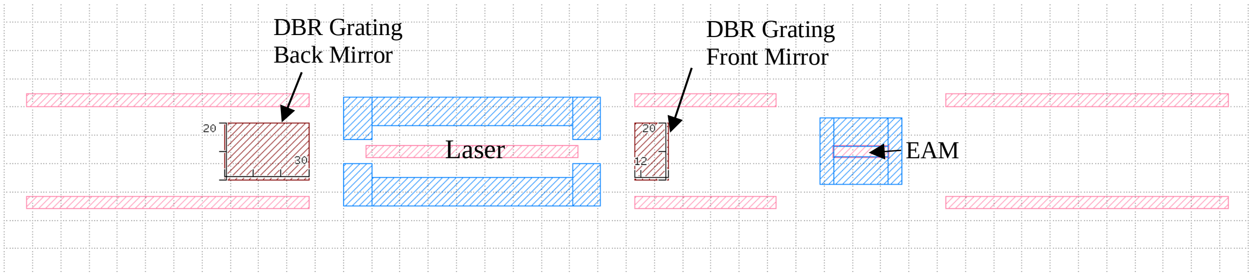

Figure 88. Mask layer 3, DRB grating windows. Ridges are shown in pink and DBR grating openings are shown in maroon.

After patterning the openings, the nitride was removed using a wet etch in a BOE:DI Water (1:10) solution and the photoresist was stripped. A further etch of layer 14 was performed only for case 8 wafers before moving onto patterning the grating. Figure 89 shows an optical image of the DBR opening in nitride layer at this stage.

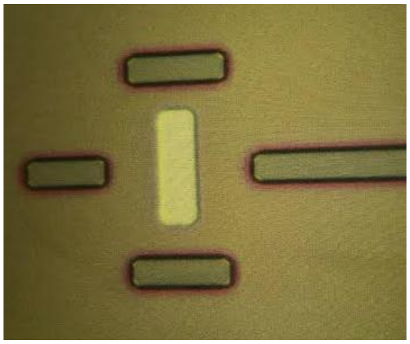

Figure 89. DBR window defined by opening silicon nitride to expose the areas being used for grating (shown in bright yellow) and the laser, EAM and dummy ridges (shown in dark rectangles)

Holography method was used to pattern the gratings. A schematic diagram of the holography table setup at SMU is shown in Figure 90. This setup is used to make holographic gratings with a grating period, Λ, that is related to the incident angle, θ, with Eq. 4.1 below.

$$\Lambda = \frac{\lambda}{2\sin\theta} \tag{5.2}$$

The beam splitter used in this setup is a wedged plate beam splitter that is designed to avoid ghost patterns, a concept that is explained in Figure 91. Many beam splitters suffer from ghost patters, eventually affecting the quality of the pattern created. In this specific beam splitter, the wedge angle, α, and orientation is designed in a way that it traps the ghost pattern inside the prism using the concept of total internal reflection [53].

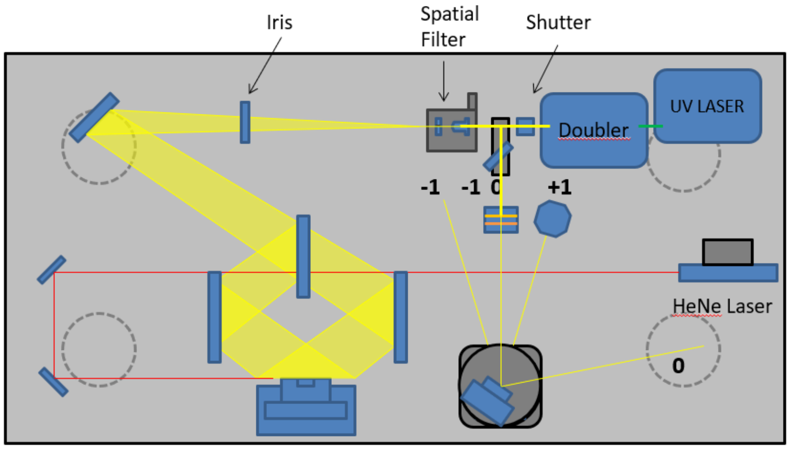

Figure 90. Schematic drawing of holography setup at SMU grating room

This concept does not require any extra coating which makes it suitable for use in high power systems. Deviation and displacement caused by this beam splitter can be compensated for simply by using another beam splitter.

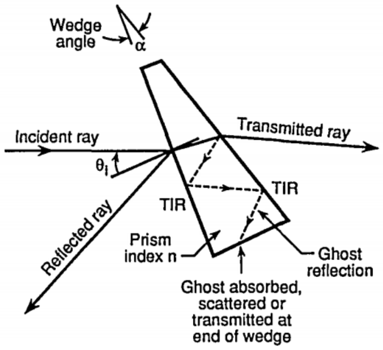

Figure 91. Propagation of light inside a ghost-less wedge beam splitter [53]

A bottom anti reflection coating (BARC) is used before spinning photoresist on the wafers. The BARC layer is intended to attenuate the reflection of incident light from the wafer surface into the resists that can affect resolution and repeatability for small, near resolution limited, feature sizes [54], [55]. DUV42P-6 was spun on the wafer at 2250 RPM for 30 sec to achieve a target thickness of 600 Å for the BARC layer and it was baked on a hot plate at 200°C for 60 seconds.

Next, a photoresist sensitive to UV light was selected since the laser source for holography system is a UV source. UV6-0.6 resist was made by diluting UV6 in a 1:2 ratio with a P-Thinner. Photoresist was spun on at 1200 RPM to achieve a $1700A$ thickness followed by a soft bake at 130°C for 60 seconds. At this point the wafer was ready to be exposed using the holography setup shown in Figure 90. A post bake on hot plate at 140°C for 90 seconds strengthened the resist before developing in MF26A developer for 12 seconds. Then it was rinsed with DI water and blow dried with nitrogen gun.

A SEM inspection was performed at this point to make sure the grating teeth came out fine, then beginning the process of etching down the DBR grating mirrors. For this step a dry etch using RIE system was used to achieve a clean footstep. For Case 6 etching was performed into layer 14, InP layer while for Case 8 it was into layer 13, InGaAsP layer with a target depth of 1000 Å and 1240Å, respectively. After another SEM inspection to ensure landing on the correct layer, grating mask was stripped off, BARC was removed, and the nitride layer was removed using a 90 seconds dip into BOE.

With the grating structures being etched into the wafer, it was time to put down the low index filler into the grooves. Spin-on-glass (SOG) was spin coated with an intention to fill grating teeth to the top of the grating (1000 Å for Case 6 and 1240 Å for Case 8). The SOG from Accuglass 312B was selected due to its ability to produce as layer as thin as 2100 Å, with an index of 1.36 at 1310nm. The top of this layer was then etched back in CF4/O2 plasma process until planarized to top of grating. Figure 92 shows the SEM results of the gratings with the SOG layer on top (a) and etched back to the top of the gratings (b).

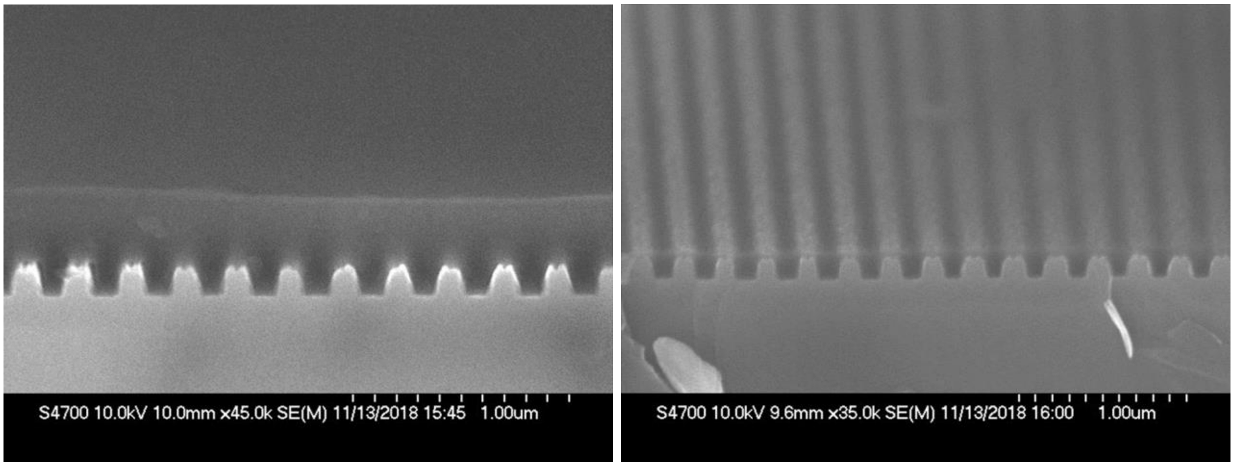

(a) (b)

Figure 92. Gratings from process development for NASA phase I (a) after the low index (index of 1.36 at 1310nm) spin glass is spun on with a target thickness of ~400nm and (b) after SOG is

etched back with CF4-based plasma with the intention of stopping at grating ridge tops to create the fill.

The high index amorphous silicon cover layer was then sputtered on top of the planarized gratings using the sputtering machine. The amorphous silicon target thickness for Case 6 was 5000Å and for Case 8 was 3500Å. Then photolithography for mask layer 4, DBR silicon etch, was performed using the conventional process flow followed by exposure, development, inspection and PR strip.

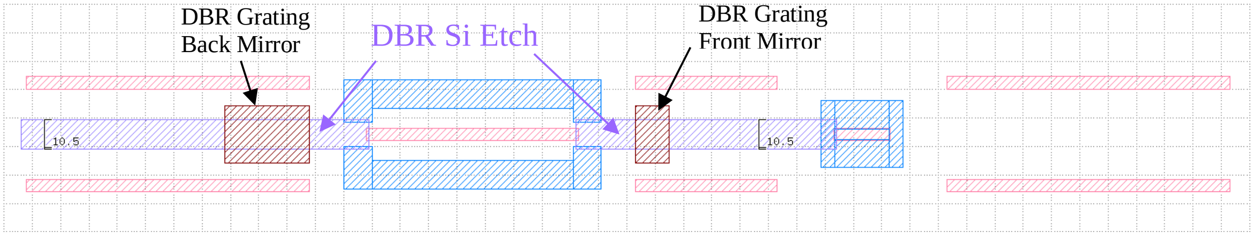

Figure 93. Mask layer 4, DBR Silicon etch windows

Technic RIE tool can be used at a high pressure CF4/O2 dry etch. Raising the pressure up above 400mT helps keep the etching fairly isotropic and enables etching the silicon layer, SOG layer and Nitride layer all at once from the sidewalls and other topography as well. Keeping the oxygen level low, makes this process more selective to the resist and it will be good enough to protect the DBR region. Figure 94 shows the result of this step.

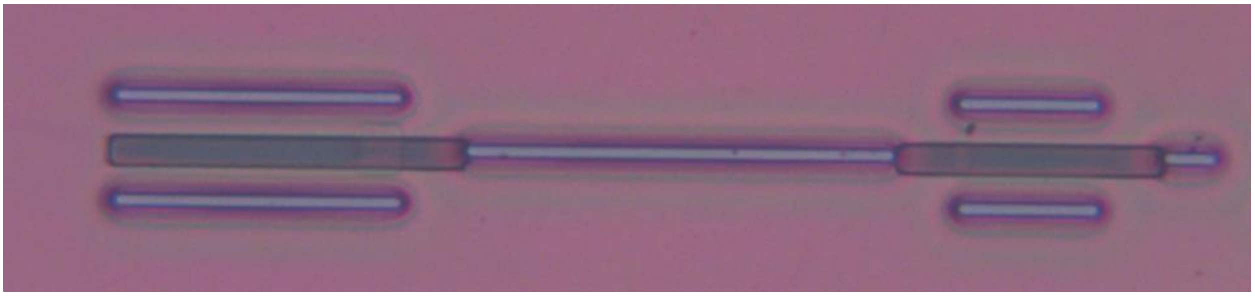

Figure 94. Optical image of the device post DBR Si etch

The next step was to deposit 1200 Å silicon nitride using PECVD system and photolithography to pattern the fourth mask layer, out-coupler nitride as shown in Figure 95. Then using BOE for 90 seconds would be enough to etch the nitride from the out-coupler window. After patterning the nitride, the photoresist was stripped off and wafers were ashed to get rid of any organic residue. This nitride layer is going to act as a mask for the holography step when patterning the out-coupler grating. The holography step used the same photoresist and conditions explained for DBR gratings. Except this time the grating period is different since the out-coupler is designed to work at second Bragg condition. The InP layer was then etched down to create the out-coupler grating.

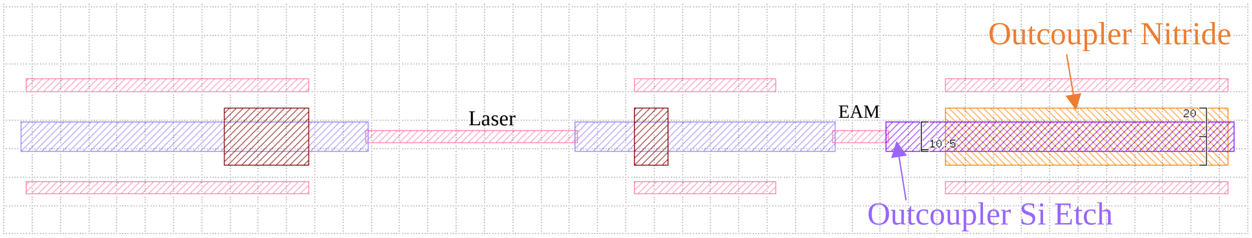

Figure 95. Mask layer 5 and 6, Outcoupler Nitride opening and Outcoupler Si Etch, respectively.

Fabrication of outcoupler for the device was skipped at this point to finish processing the rest of the device and to show that the laser and EAM work. Originally, the plan was to follow the results of simulations presented in previous chapter and deposit $0.19\mu m$ of amorphous silicon to act as the cover layer. Then to pattern mask layer 5, outcoupler Si Etch using photolithography as shown in Figure 95. The Silicon, SiO_2 and nitride layer would all be removed from this opening using an etchant that consists of 55 mL Glacial Acetic Acid, 35 mL Nitric Acid and 20 mL Hydrofluoric Acid (49%) for 15 seconds at room temperature. However, this part was sacrificed to get working device by the end of the deadline and the final device was implemented without an out-coupler.

5.2.4. Confinement Ridge

The next step was to fabricate the confinement ridge to create a common waveguide for all the components. The confinement ridge is designed to be 1 micron wider than the EAM ridge to allow for misalignment as shown in Figure 96. For lithography, photoresist Shipley 1813 was spun at 4500 RPM for 30 seconds with a target thickness of 14-16 kÅ. Then a soft bake was performed at 100°C for 60 seconds followed by exposure through the 6th mask layer, Confinement Ridge mask using MJB3 mask aligner at 194 Watts for 5.5 seconds.

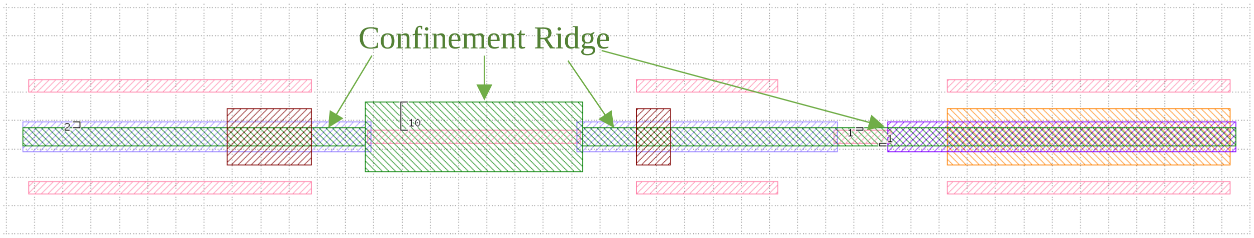

Figure 96. Mask layer 7, Confinement Ridge

After that, the photoresist was developed in MF-26A developer for 45 seconds followed by a hard bake hot plate at 100°C for 5 minutes. The confinement ridge was then dry etched in the RIE system. Figure 97 exhibits the optical image of the confinement ridge after etching after the photoresist was removed.

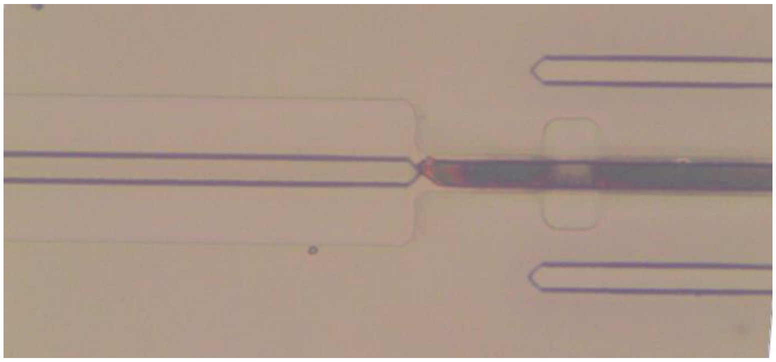

Figure 97. Optical image of the laser area with confinement ridge defined and etched.

5.2.5. N-well

After defining the confinement ridge, it was time for photolithography for layer 8, N Well, shown in Figure 98 in pink color. The purpose of N-well pads is to connect the top metal layer to the n-substrate. Therefore, big holes needed to be etched down to the substrate, nitride would be put on afterwards, then via through this layer using the N-Via layer.

N-well pads were designed big enough to allow for probing with small resistance and capacitance. Another criteria to consider when designing the N Well layer was that there has to be a good distance between the pads and the sides of the die so a designer does not accidentally cut through them when dicing the dies whether with a laser cutter, mechanical saw or scribe and break. The width of the streets therefore was designed to be 50µm. It is important to keep the metal-to-metal distance above a 5µm distance to avoid cross talk and capacitance loss [56].

Photolithography for this layer followed the same recipe used throughout this project, S1813 was spun at 4000 RPM for 30 seconds. Then wafers were patterned using MJB3 Karl Suss and developed in MF-26A developer for 45 seconds. A hard bake is necessary at this step to harden the photoresist pattern to withstand the wet etch process. After that, the wafer was etched in an InP etchant to etch InP layer, followed by InGaAsP etch to layer 2, followed by InP etch all the way down to the substrate.

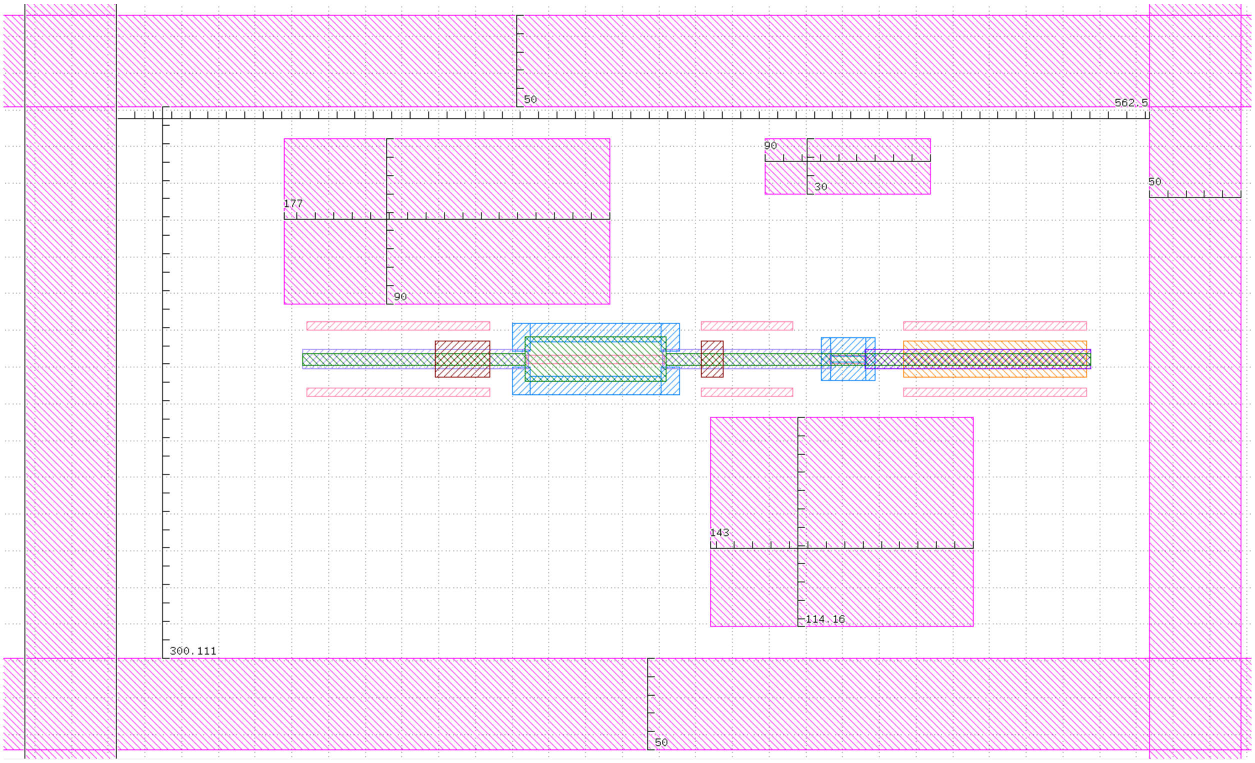

Figure 98. Mask layer 8, N Well shown in pink with measurements as specified

5.2.6. Passivation, P-Via and N-Via

The P-Via and N-Via masks are patterned using a photoactive benzocyclobutene (BCB)-based polymer rather than photoresist. Research led to the decision to spin BCB only once to use for both masks. Then the two masks P-Via and N-Via were used one after the other to expose the designated areas in each. The N-metal mask was exposed with higher dose. Then both masks were developed at the same time to pattern the holes in the BCB layer. BCB can act as a passivation layer to ensure an electric insulation between p and n side. BCB keeps capacitance low and planarizes the surface to enable better contact to metal. Targeting $3\mu m$, CYCLOTENE 4022-35 BCB was selected since it can provide a range of thickness between $2.5 - 5\mu m$ with a dielectric constant of ~2.65 [57]. To put the BCB on, start by increasing the speed to 500 RPM for 5-10 seconds to spread resist before spin, then spun at 3500 RPM for 20 seconds. A soft bake on the hot plate at 70°C for 90 seconds was followed. Post bake height target showed 3.1 microns.

Next, the resist was patterned with mask layer 9, P-Via, exhibited in Figure 99 in solid maroon using MJB3 mask aligner. This alignment was very delicate due to the small features of P-Via opening ($2.5\mu m$ width withing $1\mu m$ distance inside the ridges). Since developing was not performed immediately after exposure, a 90°C hotplate was needed to stabilize the film before exposing it through the second mask.

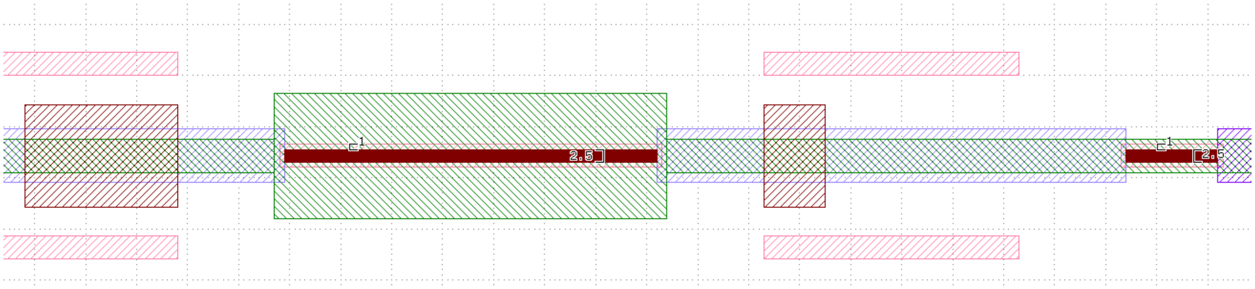

Figure 99. Mask layer 9, P-Via shown in solid maroon defined inside the laser and EAM ridges within 1 microns.

As for the N-Via mask, layer 10, the openings were bigger than the ones for P-Via, therefore a higher dosage was required. The pattern used for this mask is exhibited in Figure 100. The design follows the same rules as the N-Well mask but it is shrunk by $5\mu m$ on each side to ensure it sits within the N-Well openings. After this, the wafers were immersed in DS3000 developer and were developed until the openings were clear with an additional 50 % over develop to ensue both masks are patterned properly. Figure 101 shows an optical image of the p contact openings at this stage.

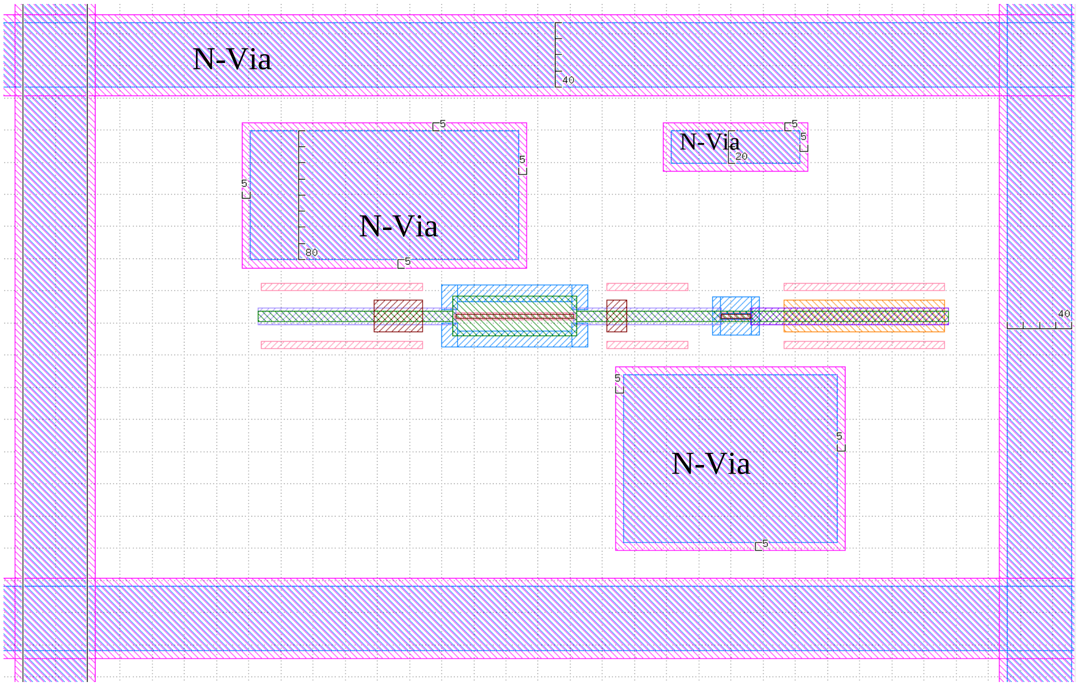

Figure 100. Mask layer 10, N-Via shown in stripe blues with measurements as specified

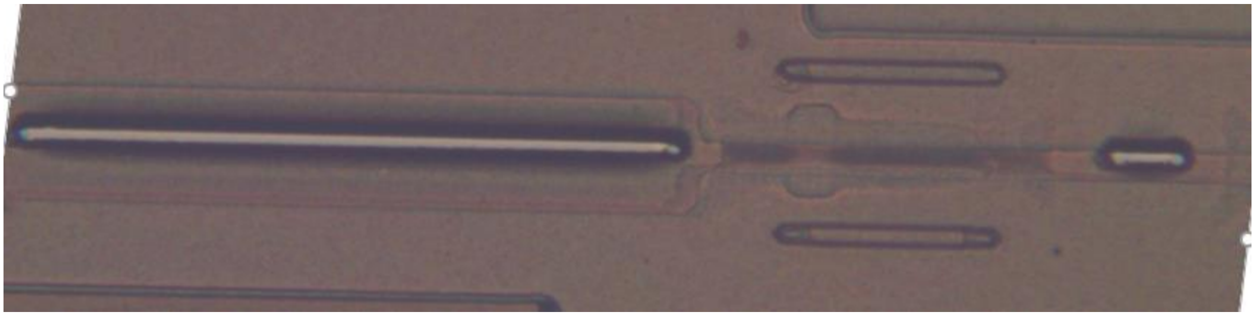

Figure 101. Optical image of the wafer post BCB dry etch of p contact opening

The results showed that both N and P via openings were clear and P via was aligned very well on the ridge. The height of the BCB was then measured with profilometer to show 3.3 microns which will shrink after curing.

This step was followed by a post develop bake at 90°C for 60 seconds and was cured in a box oven containing less than 100 ppm of oxygen at 250°C for 60 minutes. This process was performed in three steps, first wafers were placed in the oven while ramping the temperature to 150°C in 15 minutes, next it was soaked for 15 minutes and ramped to 250°C and finally it was soaked for 60 minutes. It was then cooled to under 150°C before opening the oven. Then a descum was performed using 80:20 O2:CF4 in Technics tool. BCB thickness was measured after this step and showed around. Figure 102 shows an optical image of the wafer at this stage.

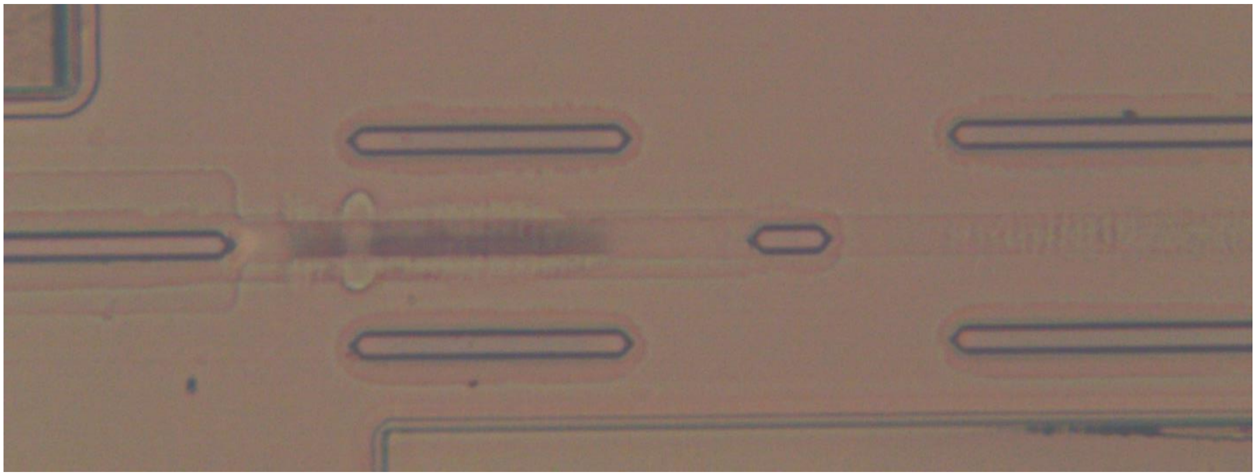

Figure 102. Optical image of wafer post BCB cure.

5.2.7. Metallization

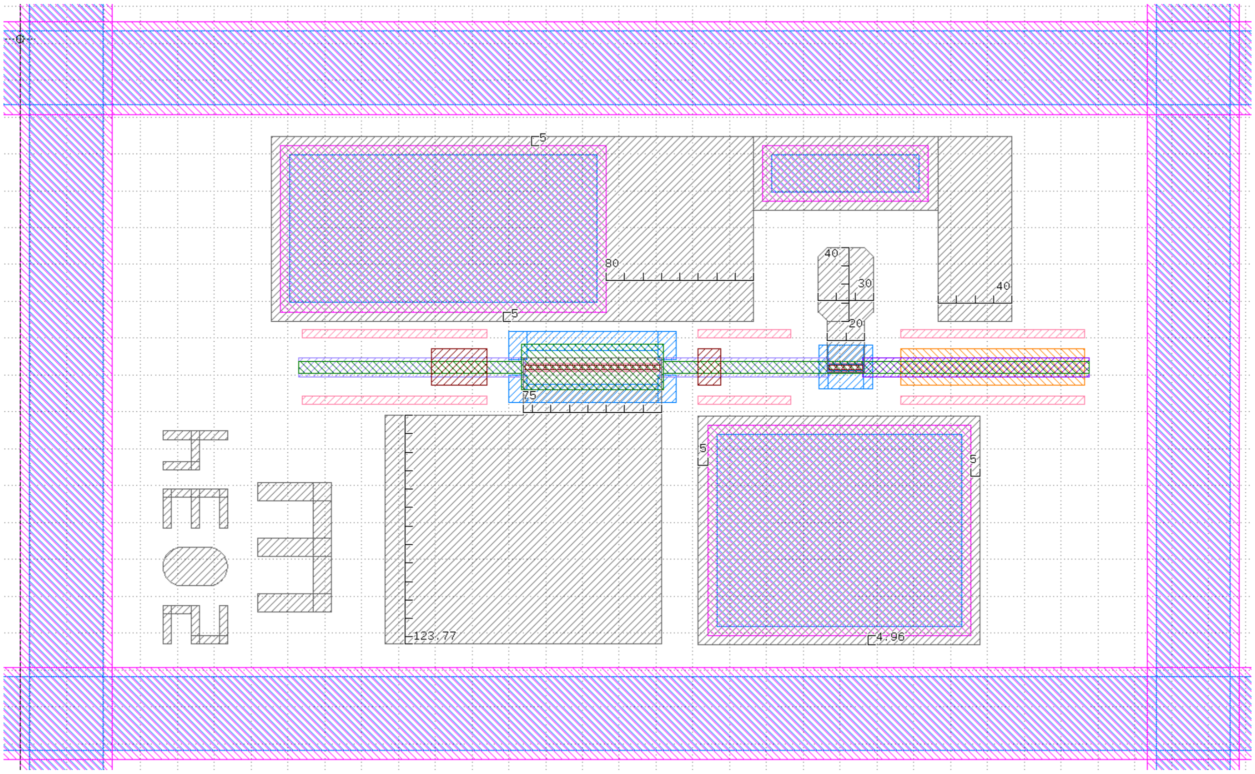

Figure 103. Mask layer 11, Metal layer in gray with measurements as shown.

The last step in fabricating was the Metal Deposition and Lift-off Process. With the P-Via and N-Via patterned on BCB there was no need to use a lithography method. Therefore, E-beam tool was used to deposit a stack of metal layers with the following thicknesses: Ni 50Å, Ge 50Å, Au 675Å, Ge 275Å, Ni 230Å, Au 2000Å which yields to a total thickness of 3280Å or 0.328μm.

The metal layer sitting on top of the BCB was then lifted off by soaking the wafers in acetone for 60 seconds to remove the backside tape, followed by acetone spray for lift-off. Figure 104 shows an optical image of the result.

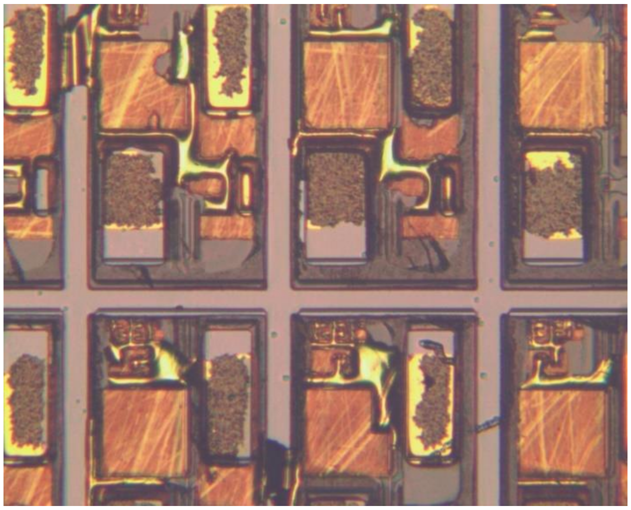

Figure 104. Optical image of one of the wafers after lift-off process- fail attempt

In a first attempt, the lift-off results were not satisfying. As a result, it was decided to introduce a layer of lift-off resists (LOR) before spinning the photoresist. Using these two layers enabled better definition of pattern post lift-off as shown in Figure 105.

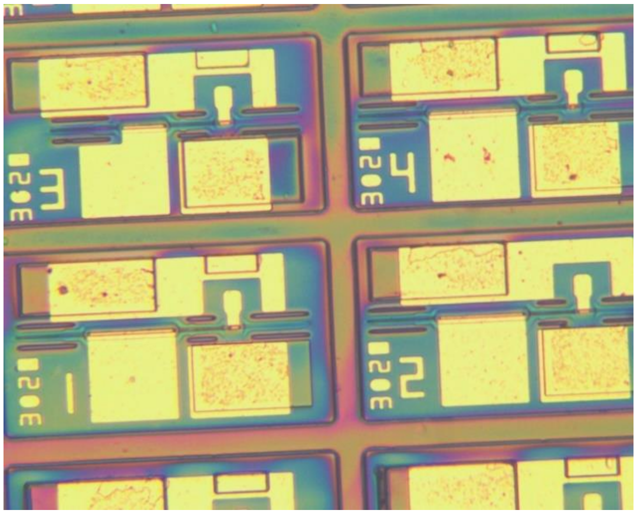

Figure 105. Optical image of wafer after metal is successfully lifted off

The wafer then went through an O2 Clean: 100sccm O2, 75mTorr at 200 W RF for 180 seconds to remove any excess organic material. At the end, it was annealed at 390°C for 20 minutes. The results of first annealing were not promising as shown in Figure 106, therefore it was decided to anneal the wafers yet one more time.

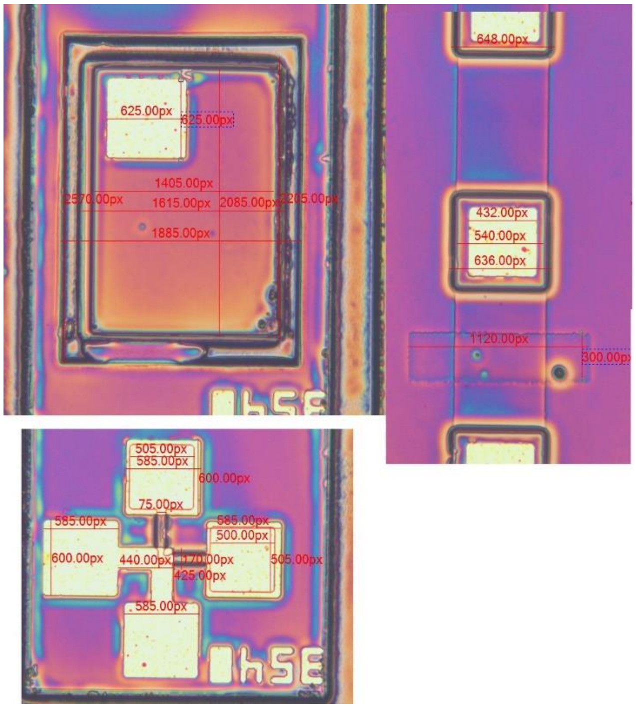

Figure 106. Optical image and measurements on a few test devices on the wafer post first annealing

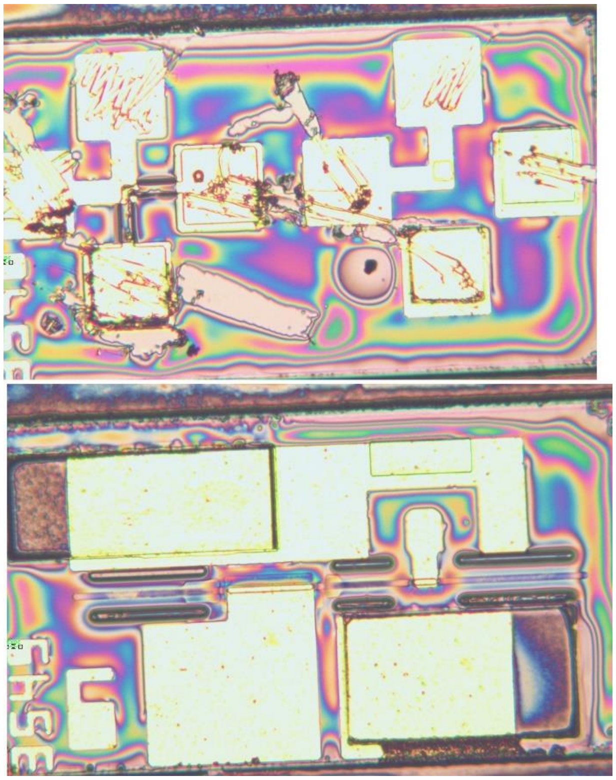

Figure 107. Optical image of the wafer on two different locations with devices and test structures post second annealing (picture was taken after probing, scratch marks on the test devices are due to probing)

The processing of the wafers was finished at this point and wafers were ready for wafer thinning and dicing.

5.2.8. Backside thinning

The process of wafer thinning was performed at IntelliEpi. The wafer thickness must be measured as first step using a digital thickness gauge like the one shown in Figure 108. The thickness was measured to be 362μm before thinning and the target thickness after thinning is 140μm.

Figure 108. Measuring the wafer thickness using a digital thickness gauge

Next, the chuck was put on a hot plate and used the powdered carbowax3350 to wax wafers on it. Wafers were facing down so that the back is exposed for thinning. A few dummy pieces were used on the outside of the chuck to even out the wafer surface as shown in Figure 109. To get rid of the excess wax underneath the wafer pieces, they should be gently pressed and then cooled down.

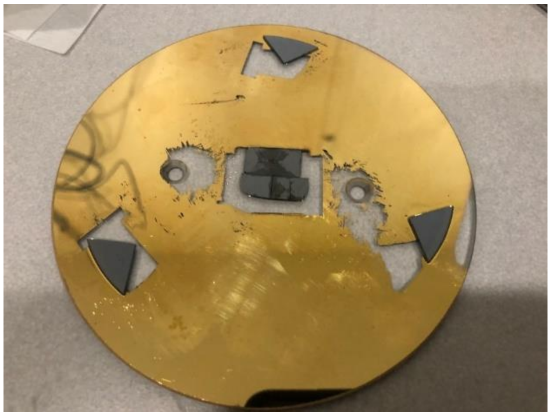

Figure 109. Wafer and dummy pieces waxed on top of the chuck facing down.

Next, the automatic thinner shown in Figure 110 was used for the thinning process. This tool that has several settings to adjust and monitor the thinning process. After that, 20g of Eminess ultra-sol L9 was mixed with 500ml water to be used as lubricant and friction maker and was poured into the container on top of the rotating machine.

Figure 110. Automatic wafer thinner setup at IntelliEpi

Next, turned the rotating machine was turned on and powder was mixed first. DI water was poured into the surface and put the chuck that is screwed to the glass and aluminum holder facing down inside the white ring and set the speed to 50rpm. The chuck must be rotated every once a while to make sure of even thinning. Starting with 5 minutes incrementing 1-minute intervals, the result must be measured at every step and repeated until the desired thickness is reached. A total of 10 minutes was needed to get the desired thickness of 140µm. At the end the surface was cleaned with DI water and tissues and the cap was put on. The wafer pieces did not need to be removed from the dummy silicon wafer since next step was to put down the backside metal on them. At a thickness of 150µm they were too fragile to be handled separately at this point.

5.2.9. Cleaving

After thinning wafers, n-metal was deposited on the backside and they were ready for cleaving. Cleaving is a process of mechanical or laser sawing the wafer into dies or in this case bars. If processing a commercial product, it would be cleaved into dies. However, this device was to be tested with university lab equipment therefore needed to be cleave into bigger than a die size for handling. Therefore, bars of ~612µm and 1cm long was selected. Loomis scriber available at Photodigm was used to scribe the wafers.

Figure 111 shows the full device including the 1550 nm laser and integrated EAM and the vertical orange lines are where was intended to be cleaved. It is important to make sure that the cleaves go through the ridges, so the vertical bars could have been be moved tens of microns to the left to make sure cleaving through the ridges occur. This was due to omitting the fabrication of the out-coupler. We can send an updated cleave drawing. The tolerance on exactly where the cleaves occur is many tens of microns. A mechanical scribe tool has a very fine blade that can be used to indent a line where cleaving is intended. The wafer pieces are placed on a sticky stretched plastic and a small cylinder rolls over the top of wafers to apply enough pressure for the wafers to break along the intended lines.

Figure 111. Position and distance between cleave lines for a finished product

Chapter 6

CONCLUSION AND FUTURE WORKS

An efficient, short outcoupler was designed and optimized for an 11 quantum well integrated laser-EAM device operating at wavelengths in the 1550 nm region which could out-couple 80% of the optical power in a 17µm long grating or 90% in a 26µm long grating.

Simulations using primarily Floquet-Bloch analysis demonstrated two Enhanced Coupling Strength (ECS) grating configurations. One configuration requires depositing a thin low-index liner layer conformal to a grating interface and then adding a high-index cover layer (ECS-liner or ECSL). A second configuration requires filling the grooves of the grating with a low index material (n ~ 1.3), such as spin-on glass, and then adding a high-index cover layer (ECS-no liner or ECSNL). Both structures significantly improve the outcoupling and reflectivity of second-order gratings. The ECSNL structure generally has the best performance.

Generic second-order ECS output couplers were analyzed and optimized to provide maximum out-coupled power for a 10µm grating length. A conventional grating provides a maximum of 42% out-coupled power. For ECSL structure, maximum out-coupled power of 63% was achieved with a 75nm liner thickness, 50% duty cycle, and 0.1µm cover layer. For ECSNL structure, maximum out-coupled power of 82% was achieved with a 0.2µm cover layer and 50% duty cycle.

Because of the difficulty of fabricating the small period gratings required for first-order gratings, especially in the visible and UV wavelength regions, second-order gratings can be optimized to maximize reflectivity instead of outcoupling. Maximum reflectivities are shown at duty cycles of ~75% (conventional gratings), ~80% (ECSL gratings) and 35% (ECSNL gratings).

A complete mask set and process flow was developed for the fabrication of the monolithic laser-EAM device for operation at wavelengths of 1550nm and 1310nm. The Laser-EAM device utilizes the exact same patented quantum well active region for both the laser and the EAM which allows the structure to be grown in a single epitaxial run and fabricated with relatively simple processes. The Laser-EAM can operate over a 100C temperature range without a thermos-electric cooler and uses only 100 fJ/bit [2].

Validity of SMU Floquet-Bloch software was confirmed by comparison with the simulation results from Finite Difference Time Domain (FDTD) and EigenMode Expansion (EME) methods for simple generic (5 layer) waveguide gratings structures.

In the future, FDTD and EME commercial software should be able to analyze the 30 plus layers of the 11 quantum well Laser-EAM by running on the SMU High Performance Computer, providing further verification of the SMU Floquet-Bloch software.

Future work also includes improving the SMU Floquet-Bloch software to include hundreds of higher-order space harmonics, which will reduce some errors encountered in simulations of ECSL gratings.

Finally, completing the fabrication and testing of entire Laser-EAM devices including an out-coupler grating at a range of wavelengths from ~1300nm to ~1700nm is expected within a year. Both holographic and e-beam gratings will be used in the fabrication of the devices.

APPENDIX

Traveler

DOE STTR Traveler

Lot ID:		**Epi Source:**	Nlight
		Wafer No.	
Customer:	DOE STTR	**Rev.**	

Step #	**Process**	**Procedure/Parameters**	**Qty In**	**Qty Out**	**Operator**	**Date**	**Data/Comments**	
		PHOTO PATTERN RIDGE MASK						
1	Inspect Wafers Metallurgical Microscope	Inspect Epi wafer for defects and cleanliness. Document all defects before process.						
2	Cleave Wafers	Cleave wafers into pieces for processing if necessary. Put the remain wafer sections back in the dry box for future use.						
4	Silicon Nitride Deposition STS PECVD	Recipe: **mansin.se**t: (He = 250sccm, 500sccm N_2, 50sccm SiH_4, 600mTorr, 70W RF)					Target Thickness (Å)	1200 **(+ - 200)**
							Target Run Time (sec)	
							Actual Run Time (sec)	
							Actual Thicknes (Å)	
							Actual n Value	
6	Dry Bake Solvent Hood	Hot plate bake at 100°C for 60 sec.						
7	Spin Resist Cee Spinner	S1813 resist.4500 RPM for 30 seconds					Typical Thickness: 1.35 microns	
8	Soft Bake Solvent Hood	Hot plate bake at 100°C for 60 sec.						
9	Clean Alignment Edge Solvent Hood	Use q-tips soaked with acetone to clean across the cleaving edge of the wafer that is parallel to the major flat for the ridge alignment.						
10	Expose Karl Suss Alignmer	Dose: xx mJ/cm^2, ____ seconds exposure at 194 Watts					Mask ID: Ridge 1	
							Lamp Power (mW/cm^2)	
							Expose Time (sec)	#DIV/0!
11	Develop Acid Hood	AZ MF-26A developer 45 seconds. DI water rinse for _______ sec., N_2 dry.					Actual Develop Time (sec)	
12	Inspect Metallurgical Microscope	Inspect wafers for complete develop and pattern definition.					Width of resist top on ridge ______________________________	
13	Hard Bake Solvent Hood	Hot plate bake at 100°C for 300 sec.					Profilometer height __________________________________	
	Ash	O2 Ash, 500 mT, 100 W, 1 minute etch						
14	Etch Silicon Nitride Oxford RIE	CF4/O2, 190 mT, 100W, 15-16 minutes etch					Target Etch Depth (A)	
							Target Etch Time (sec)	
							Actual Etch Time (sec)	
16	Inspect Microscope and measure height with profilometer	Inspect for complete nitride etch and measure profilometer height.						
17	Ash	O2 Ash, 500 mT, 100 W, 1 minute etch						

Wet Etch Ridge Pattern								
18	Etch Cap Layer InGaAs/InGaAsP:	1) DI water rinse 30 sec to ensure the wafer is wetting ok. 2) BOE (10:1) dip for 1 sec. 3) Wet etch InGaAs/InGaAsP in H2SO4 : H2O2 : DI water (1:2:10) etchant at about 5°C for 15 sec. DI water rinse for 60 sec., N2 dry 4) Measure etched depth. 5) Repeat step # 3 - 4 for additional 2 sec etch time.					Target Depth (A)	Etch layer 16 and 15, target 1100 A
							Actual Depth (A) (mask - depth)	
19	Inspect Metallurgical Microscope	Inspect wafers for complete etch.						
20	Strip Resist Solvent Hood	Acetone rinse, IPA rinse, N2 Dry.						
21	Inspect Metallurgical Microscope	Inspect wafers for complete removal of resist.						
DRY ETCH RIDGE PATTERN								
22	Ash	Plasma Ash, O2 etch. 5 minutes run time.						
23	Inspect Metallurgical Microscope	Inspect wafer for complete removal of residues and cleanliness.						
24	Partial Dry Etch Cladding InP	RIE, 12 mTorr, 50 W,_______ min run time.					**Dry etch 80% through InP layers 14, 13, 12 = 1.2 micron of InP etch, actual depth:**	
	Ash in Speaks	O2 etch, 500 mTorr, 100 W, 10 min run time						
Wet Etch Ridge Pattern Continue…								
25	Wet Etch Cladding InP Leftover	1) DI water for 30 sec to ensure the wafer is wetting ok 2) BOE (10:1) dip for 1 sec 3) Etch InP cladding in HCl: DI water: H3PO4 (12:3:5) etchant at about 5°C for _____ sec					Etch time_______ Height _________ , height should be about 1.61 microns + nitride thickness	
26	Etch 1st Etch Stop InGaAsP	H2SO4 : H2O2 : DI water (1:2:10) etchant at about 5°C for 15 sec. DI water rinse for 30 sec., N2 dry.					**Etch layer 11, Height _______________**	
27	Strip Nitride	BOE : DI water = 1:10 at RT for 90 sec., DI water rinse for 30 sec., N2 dry.					Height without Nitride _______________________	
28	Ash Oxford RIE	Recipe: Man O2 Clean: 100sccm O2, 75mTorr, 100 W RF. Run Time = 120 sec.						
29	Inspect and Measure Final Depth and Width of Ridge	Inspect for wafer cleanliness and complete nitride removal. Measure depth and width of ridge at top, center, and bottom of wafers.						

PECVD SILICON NITRIDE DEPOSITION and PHOTO PATTERN OC

30	Calibrate Silicon Nitride Deposition Rate STS PECVD	Recipe: **mansin.set**: (Argon/He = 1250sccm, 600sccm N_2, 100sccm SiH_4, 600mTorr, 70W RF, Run Time = 300 sec). --					Thickness Spec.	850 - 1000Å
							n Value Spec.	1.9354
							Actual Thickness (Å)	
							Actual n Value	
31	Silicon Nitride Deposition STS PECVD	Recipe: mansin.set: (Argon/He = 1250sccm, 600sccm N2, 100sccm SiH4, 600mTorr, 70W RF, Run Time = xxx sec). --					Target Thickness (Å)	**1200** **(+ - 200)**
							Target Run Time (sec)	
							Actual Run Time (sec)	
							Actual Thickness(Å)	
							Actual n Value	
40:154140:1	Spin HMDS Cee Spinner	MCC Primer 80/20. **PROG #5**: 3000 RPM for 40 sec.						
33	Dry Bake Solvent Hood	Hot plate bake at 100°C for 60 sec.						
34	Spin Resist Cee Spinner	S1813 resist. 4000 RPM for 30 sec.					Typical Thickness: 14.0 - 16.0kÅ	
35	Soft Bake Solvent Hood	Hot plate bake at 100°C for 90 sec.						
36	Expose Karl Suss	5.5 second exposure, 194 Watts					Mask ID: Gratings4	
							OC opening pull back distance.	
							Lamp Power (mW/cm^2)	
							Expose Time (sec)	
37	Develop Acid Hood	MF-26A developer for 45 sec. DI water rinse for 30 sec., N_2 dry.					Actual Develop Time (sec)	60
38	Inspect Metallurgical Microscope	Inspect wafers for complete develop and pattern definition.						
39	Hard Bake Solvent Hood	Hot plate bake at 100°C for 5 min.						
40	Ash Oxford RIE	Recipe: **Man O2 Clean**: 100sccm O_2, 75mTorr, 100 W RF. Run Time = 120 sec.						
41	Wet Etch Nitride	BOE : DI water = 1:10 at RT for _90_ sec., DI water rinse for 60 sec., N2 dry.					<-- DI water wet wafer before go in BOE -- (OC windows all clear)	
42	Inspect Metallurgical Microscope	Inspect wafers for complete silicon nitride etch.						
43	Strip Photoresist	Rinse with Acetone and IPA, N2 dry.						
44	Ash Oxford RIE	Recipe: **Man O2 Clean**: 100sccm O_2, 75mTorr, 100 W RF. Run Time = 120 sec.						
25	Wet Etch InP layer 10	1) DI water for 30 sec to ensure the wafer is wetting ok 2) BOE (10:1) dip for 1 sec 3) Etch InP cladding in HCl: DI water: H3PO4 (12:3:5) etchant at about 5°C for XX sec						

PHOTO PATTERN GRATING for OC								
45	Spin BARC Cee Spinner	**DUV42P-6 PROG #3: 1500 RPM for 40 sec.**					Target Thickness (A)	741
45.1	Pre- Bake Solvent Hood	Hot plate bake at 100°C for 60 sec.						
46	Bake Solvent Hood	Hot plate bake at 190°C for 120 sec.						
47		Repeated step # 45 & 46.						
48	Spin Resist Cee Spinner	UV6-0.6 resist (1:2) dilution UV6-0.6 resist to P-Thinner. **PROG #4:** 1400 RPM					Target Thickness (A)	1700
49	Soft Bake Solvent Hood	Hot plate bake at 100°C for 90 sec.						
50	Expose SMU Gratings Process	SMU Grating Exposure Process					Target Grating Period (Å)	
							Actual Gratings Period (Å)	
							Laser Power at Stage ($\mu W/cm^2$)	
							Actual Expose time (sec)	
							Exposure Dose ($\mu J/cm^2$)	
51	Post Bake Solvent Hood	Hot plate bake at 140°C for 60 sec.						
52	Develop	AZ 300 MIF for 60 sec., DI water rinse for 60 sec., N_2 dry.						
53	Hard Bake Solvent Hood	Hot plate bake at 100°C for 120 sec.						
54	SEM Inspection Hitachi S-800 SEM							
55	open gratings pattern Oxford RIE	Recipe: **Gratings pattern etch**: 25 sccm O_2, 50 sccm Ar, 25mTorr, 150 W RF. Typical Run Time = 80 sec.					Actual Etch Time (sec)	75

Confinement Ridge Process

	Spin HMDS Cee Spinner	MCC Primer 80/20. **PROG #5**: 3000 RPM for 40 sec.						
33	Dry Bake Solvent Hood	Hot plate bake at 100°C for 60 sec.						
34	Spin Resist Cee Spinner	S1813 resist.4500 RPM for 30 seconds					Typical Thickness: 14.0 - 16.0kÅ	
35	Soft Bake Solvent Hood	Hot plate bake at 100°C for 60 sec.						
36	Expose Karl Suss	Dose: xx mJ/cm^2, 5.5 seconds exposure at 194 Watts					Mask ID: Ridge6	
								0.5 - 2.0um
							Lamp Power (mW/cm^2)	7.5
							Expose Time (sec)	10.00
37	Develop Acid Hood	MF-26A developer for 45 sec. DI water rinse for 30 sec., N_2 dry.					Actual Develop Time (sec)	60
38	Inspect Metallurgical Microscope	Inspect wafers for complete develop and pattern definition.						
39	Hard Bake Solvent Hood	Hot plate bake at 100°C for 5 min.						
40	Ash Oxford RIE	Recipe: **Man O2 Clean**: 100sccm O_2, 75mTorr, 100 W RF. Run Time = 120 sec.						
57	Dry Etch Confinement Ridge	RIE, 12 mTorr, 50 W, ___XXX___ min run time.					Etch to layer X	
58	SEM Inspection Hitachi S-800 SEM							
59	Strip Off Resist	Rinse with Acetone and IPA, N2 dry.						
60	Clean Wafer Section (Ash)	O2 etch. 500 mTorr, 100 W, 5 min. run time.						

Ion Implant

	Spin Resist Cee Spinner	Pattern Mask with 2 um of resist using 1700 RPM for S1813 resist, pattern (or use 1818 for thicker)						
	Soft Bake Solvent Hood	Hot plate bake at 100°C for 90 sec.						
	Expose Karl Suss	Dose: xx mJ/cm^2, 5.5 seconds exposure at 194 Watts					Ion Implant7	
	Develop Acid Hood	MF-26A developer for 60 sec. DI water rinse for 30 sec., N_2 dry.						
	Inspect Metallurgical Microscope							
	Hard Bake	Hot plate bake at 100°C for 5 min.						
	Ion Implant	ship out for Ion Implant						
	Strip resist	Use solvents first, if this doesn't work, use oxygen plasma as well or commerical strippers						

ETCH GRATINGS for OC and deposit SiO2 and Silicon in gratings region

57	Dry Etch InP Grating	RIE, 12 mTorr, 50 W, _____ min run time.					Etch 2000 Angstroms Deep	
58	SEM Inspection Hitachi S-800 SEM							
59	Strip photoresist	Rinse with Acetone and IPA, N2 dry.						
60	Clean Wafer Section (Ash)	O2 etch. 500 mTorr, 100 W, 5 min. run time.						
104	Liner deposition	Deposit SiO2 thickness XXXX						
	Silicon deposition	Deposit Silicon thickness XXXX						

Pattern OC liner5

	Spin HMDS Cee Spinner	MCC Primer 80/20. **PROG #5**: 3000 RPM for 40 sec.						
33	Dry Bake Solvent Hood	Hot plate bake at 100°C for 60 sec.						
34	Spin Resist Cee Spinner	S1813 resist. 4000 RPM for 30 sec.					Typical Thickness: 14.0 - 16.0kÅ	
35	Soft Bake Solvent Hood	Hot plate bake at 100°C for 90 sec.						
36	Expose Karl Suss	5.5 second exposure, 194 Watts					Mask ID: Liner5	
							Lamp Power (mW/cm^2)	
							Expose Time (sec)	
37	Develop Acid Hood	MF-26A developer for 45 sec. DI water rinse for 30 sec., N_2 dry.					Actual Develop Time (sec)	
38	Inspect Metallurgical Microscope	Inspect wafers for complete develop and pattern definition.						
39	Hard Bake Solvent Hood	Hot plate bake at 100°C for 5 min.						
40	Ash Oxford RIE	Recipe: **Man O2 Clean**: 100sccm O_2, 75mTorr, 100 W RF. Run Time = 120 sec.						
	Etch Si, SiO2	Etch Silicon, SiO2, and Nitride with isotropic silicon etch: Room temperature 55 mL Glacial Acetic Acid 35 mL Nitric Acid 20 mL Hydrofluoric Acid (49%) for 15 seconds						
59	Strip Off Resist	Rinse with Acetone and IPA, N2 dry.						
60	Clean Wafer Section (Ash)	O2 etch. 500 mTorr, 100 W, 5 min. run time.						

N-Well

	Spin HMDS Cee Spinner	MCC Primer 80/20. **PROG #5**: 3000 RPM for 40 sec.						
33	Dry Bake Solvent Hood	Hot plate bake at 100°C for 60 sec.						
34	Spin Resist Cee Spinner	S1813 resist. 4000 RPM for 30 sec.					Typical Thickness: 14.0 - 16.0kÅ	
35	Soft Bake Solvent Hood	Hot plate bake at 100°C for 90 sec.						
36	Expose Karl Suss	5.5 second exposure, 194 Watts					Mask ID: nwell8	
								0.5 - 2.0um
							Lamp Power (mW/cm^2)	7.5
							Expose Time (sec)	10.00
37	Develop Acid Hood	MF-26A developer for 45 sec. DI water rinse for 30 sec., N_2 dry.					Actual Develop Time (sec)	60
38	Inspect Metallurgical Microscope	Inspect wafers for complete develop and pattern definition.						
39	Hard Bake Solvent Hood	Hot plate bake at 100°C for 5 min.						
40	Ash Oxford RIE	O2 etch. 500 mTorr, 100 W, 5 min. run time.						
	Wet etch N-Well	InP etch XX seconds, followed by InGaAsP etch to layer 2, followed by InP etch to substrate + X angstroms target depth					Initial height ___________________________________	
							Post InP etch height _______________________________	
							Post InGaAsP etch height__________________________	
							Post InP etch height _______________________________	
59	Strip Off Resist	Rinse with Acetone and IPA, N2 dry.						
60	Clean Wafer Section (Ash)	O2 etch. 500 mTorr, 100 W, 5 min. run time.					Height without resist __________________	

BCB Process

	Spin Adhesion promoter	Spin AP300 adhesion promoer, 3000 RPM 15 seconds						
33	Dry Bake Solvent Hood	Hot plate bake at 100°C for 30 sec.						
34	Spin Resist Cee Spinner	Puddle 4022-35 BCB, RPM 3500 20 seconds					Special ramp process 1) increase speed to 500 RPM for 5-10 seconds to spread resist before spin. Post bake height target is 3.1 microns	
35	Soft Bake Solvent Hood	Hot plate bake at 70°C for 90 sec. Note: we can use "endpoint" monitors with our lots						
36	Expose Karl Suss P metal	30 mJ/cm^2; Contact chamber vacuum = -0.3. Align XXXXX , **NOTE1:** recommended exposure does is 20 mJ, **Note2** : If developing does not occur immediately after exposure, a 50 C hotplate is needed to stablize the film.					Mask ID: P Contact 9	
							Lamp Power (mW/cm^2)	
							Expose Time (sec)	
36	Expose Karl Suss N metal	30 + X mJ/cm^2					Mask ID: N Contact 9	
							Lamp Power (mW/cm^2)	
							Expose Time (sec)	
	Develop	Immersion develop with DS3000, develop until clear + additional 50 % over develop						
	Rinse	rinse in DI water and N2 dry						
39	Inspection						N and P metal clear, P metal aligned well on ridge, measure height of resist with profilometer, should be about 3.3 microns (will shrink with cure)	
	Post Develop Bake	90 C for 60 seconds						
	Cure	box oven < 100 ppm of oxygen. 250 C for 60 minutes					Step 1 15 min ramp to 150 C, soak for 15 minutes, ramp to 250 C and soak for 60 minutes, cool before opening to < 150 C	
40	Descum	Use 80:20 O2:CF4 etch in Technics					Measure BCB thickness ______________________________	

Metallization

40		Treatment before metallization ? Perhaps quick BOE dip?						
	P and N Metal	SMU Ebeam P-metal process but with thick gold, total thickness = one micron						
142	Inspect Metallurgical Microscope							
143	Lift Off Solvent Hood	Soak wafers in acetone for 600 sec to remove backside tape. Acetone spray (**max pressure <20psi**) to remove resist and excess nitride. IPA rinse, N_2 dry.						
144	Measure Au Thickness Dektak						Actual Au Thickness (KÅ)	**#DIV/0!**
							Actual Plating Rate (Å/min)	#DIV/0!
145	Inspect Metallurgical Microscope	Inspect wafers for complete removal of resist and excess Au.						
146	Ash Oxford RIE	Recipe: **Man O_2 Clean**: 100sccm O_2, 75mTorr, 200 W RF. Run Time = 180 sec.						
147	Anneal JPEG Annealer	Recipe: AlGaAs390C. Save historical anneal filename.					Anneal Temp. (°C)	390°C
							JPEC Filename Saved	

References

[1] B. G. Streetman and S. K. Banerjee, Solid State Electronic Devices, 7th ed., Austin, Texas: Pearson, 2016.

[2] R. H. Johnson and G. A. Evans, "Temperature Insensitive Integrated Electro-Absorption Modulator and Laser, Ralph H. Johnson and Gary A. Evans". US Patent Patent 9762025, 12 September 2017.

[3] J. Clerk-Maxwell, "A Treatise on Electricity and Magnetism," *Nature,* pp. 478-480, 1873.

[4] D. Marcuse, Theory of Dielectric Optical Waveguides, New York: Academic Press, 1974.

[5] F. Chen, H. Amekura and Y. Jia, "Fundamentals of Ion Beam Technology, Waveguides, and Nanoparticle Systems," in *Ion Irradiation of Dielectrics for Photonic Applications,* vol. 231, Singapore, Springer, 2020, pp. pp 1-19.

[6] B. E. A. Saleh, Fundamentals of Photonics, Hoboken, NJ: Wiley-Interscience, 2007.

[7] J. C. Palais, Fiber Optics Communications, Fourth Edition ed., Upper Saddle River, New Jersey: Prentice Hall,, 1998.

[8] C. R. Doerr and H. Kogelnik, "Dielectric Waveguide Theory," *Journal of Lightwave Technology,* vol. 26, no. 9, pp. 1176-1187, 1 May 2008.

[9] "ASU MBE Optoelectronics Group," Arizona State University, [Online]. Available: https://mbe.engineering.asu.edu/research/downloads/. [Accessed 23 01 2022].

[10] Renk, Basics of Laser Physics, Springer, 2012.

[11] O. Svelto, S. Longhi, G. D. Valle, S. Kück, G. Huber, M. Pollnau, H. Hillmer, S. Hansmann, R. Engelbrecht, H. Brand, J. Kaiser, A. B. Peterson, R. Malz, S. Steinberg, G. Marowsky, U. Brinkmann, D. Lot, A. Borsutzky, H. Wächter, M. W. Sigrist and E. Saldin, Lasers and Coherent Light Sources, New York: Springer Handbook of Lasers and Optics, 2007.

[12] B. Zhao and A. Yariv, "Quantum Well Semiconductor Lasers," in *Semiconductor Lasers I,* Academic P, 1999, pp. 1-121.

[13] W. T. Tsang, "Extremely low threshold (AlGa)As graded index waveguide separate-confinement heterostructure lasers grown by molecular beam epitaxy," *Applied Physics Letter*, vol. 39, 1982.

[14] M. Prevedelli, P. Cancio, G. Guisfredi, F. Pavone and M. Inguscio, "Helium, Frequecny Control of DBR Diode Lasers at 1.08 Micrometer and Precision Spectroscopy of," *Optics Communications,* vol. 125, 1996.

[15] J. Talghader and J. S. Smith, "Thermal dependence of the refractive index of GaAs and AlAs measured using semiconductor multilayer optical cavities," *Applied Physics Letter,* vol. 66, no. 335, 1995.

[16] A. Müller, D. Vijayakumar, O. B. Jensen, K.-H. Hasler, B. Sumpf, G. Erbert, P. E. Andersen and P. M. Petersen, "16 W output power by high-efficient spectral beam combining of DBR-tapered diode lasers," *Optics Express*, vol. 19, no. 2, p. 1228, 2011.

[17] G. A. Evans and J. M. Hammer, Surface Emitting Semiconductor Lasers and Arrays, Boston Academic Press, 1993.

[18] H. Kressel and J. Butler, Semiconductor Lasers and Heterojunction LEDs, New York, 1977.

[19] K. S. Mobarhan, "Test and Characterization of Laser Diodes: Determination of Principal Parameters," *Newport Application Notes,* vol. 1.

[20] P. C. Safa Kasap, Springer Handbook of Electronic and Photonics Materials, Springer, 2006.

[21] K. Iga and F. Koyama, "Surface Emitting Lasers," in *Semiconductor Lasers II, Materials and Structures*, Yokohama.

[22] D. S. Chemla, "Quantum Wells for Photonics," *Physics Today* , vol. 38, no. 5, pp. 56-64, 1985.

[23] W. Chang, "Multiple Quantum Well Electroabsorption Modulators for RF Photonic Links," in *RF Photonic Technology in Optical Fiber Links*, Cambridge University Press, 2002.

[24] M. Peschke, B. Saravanan, C. Hanke and B. S. T. Knodl, "Investigation of the capacitance of integrated DFB-EAMs with shared active layer for 40 GHz bandwidth," in *The 17th Annual Meeting of the IEEE Lasers and Electro-Optics Society, 2004. LEOS 2004.,* Rio Grande, PR, USA, 2004.

[25] Intel, "AN 835: PAM-4 Signaling Fundamentals," Intel, 2018.

[26] R. Horner, "Shift from NRZ to PAM-4 Signaling for 400G Ethernet," DesignWare Technical Bulletin.

[27] N.-H. Sun, J. Butler, G. Evans, L. Pang and P. Congdon, "Analysis of Grating-Assited Directional Couplers Using the Floquet-Block Theory," *Journal of Lightwave Technology,* pp. 2301-2315, 1997.

[28] J. Butler, Field Theory of Optical Guided Waves, Dallas: Southern Methodist University, 2015.

[29] R.-H. He, *Enhanced Coupling Strength Gratings for Outcouplers in Optical Waveguides,* Dallas: Southern Methodist University, 2018.

[30] R. Ramaswami, K. Sivarajan and G. Sasaki, Optical Networks: A Practical Perspective, Elsevier Science & Technology, 2009.

[31] A. Yariv and P. Yeh, Photonics; Optical Eelctronics in Modern Communications, 6th ed., Oxford University Press, 2007.

[32] W. Huang, B. Little and S. Chaudhuri, "A New Approach to Grating-Assisted Couplers, Huang," *Journal of Lightwave Technology,* vol. 9, no. 6, pp. 721-728, 1991.

[33] W. Huang and H. Haus, "Power Exchange in Grating-Assisted Couplers," *Journal of Lightwave Technology,* vol. 7, no. 6, 1989.

[34] R.-H. He, "Enhanced Coupling Strength Gratings for Outcouplers in Optical Waveguides," Southern Methodist University, Dallas, Texas, United States, 2018.

[35] F. C. II, M. Dezfuli, W. Zhang, S. McWilliams, R. H. Johnson, N.-H. Sun, J. K. Butler and G. A. Evans, "First-Order Enhanced Coupling Strength (ECS) Gratings in III-V Photonic Waveguides," in *SPIE Photonics West,* San Francisco, CA, 2022.

[36] F. C. II, W. Zhang, M. Dezfuli, S. McWilliams, R. H. Johnson, N.-H. Sun, J. K. Butler and G. A. Evans, "Analysis of First-Order Enhanced Coupling Strength (ECS) Gratings in III-V Photonic Waveguides," *To be published,* 2022.

[37] A. Hardy, D. Welch and W. Streifer, "Analysis of Second-Order Gratings," *IEEE Journal of Quantum Electronics,* vol. 25, no. 10, 1989.

[38] J. K. Butler, N.-H. Sun and G. A. Evans, "Waveguide Characteristics Near the Second Bragg Condition," *IEEE Access,* To be published.

[39] G. Evans, J. Butler, R.-H. He, J. Kirk, J. Yao, X. Zheng and A. Krishnamorthy, "Enhanced Coupling Strength Gratings for Couplers in III-V Compound Dielectric Waveguides," Journal of Lightwave Technology, 2017.

[40] D. Taillaert, P. Bienstman and R. Baets, "Compact efficient broadband grating coupler for silicon-on-insulator waveguides," *Optics Letter,* vol. 29, no. 23, 2004.

[41] D.-X. Xu, J. H. Schmid, G. T. Reed, G. Z. Mashanovich, D. J. Thomson and M. Nedeljkovic, "Silicon photonic integration platform-have we found the sweet spot?," *IEEE Journal of Selected Topics in Quantum Electronics,* vol. 20, no. 4, 2014.

[42] M. Achtenhagen, N. Amarasinghe and G. Evans, "High-power distributed bragg reflector lasers operating at 1065 nm," *IEEE Electronics Letter,* vol. 43, no. 14, pp. 757-759, 2007.

[43] M. Dezfuli, W. Zhang, F. C. II, S. McWilliams, R. H. Johnson, N.-H. Sun, J. K. Butler and G. A. Evans, "Analysis of Second-Order Enhanced Coupling Strength Grating Out-Coupler in III-V Photonic Waveguides," *To be published,* 2022.

[44] G. A. Evans, J. K. Butler and R.-H. H. Jay Kirk, "Enhanced Coupling Strength Gratings". US Patent 10371898, 6 August 2019.

[45] G. A. Evans, J. K. Butler, J. B. Kirk, R.-H. He, J. Yao, G. Li, X. Zheng and A. V. Krishnamoorthy, "Enhanced Coupling Strength Grating Having a Cover Layer". US Patent 10620379, 14 April 2020.

[46] M. Dezfuli, F. C. II, W. Zhang, S. McWilliams, R. H. Johnson, N.-H. Sun, J. K. Butler and G. A. Evans, "Second-Order Enhanced Coupling Strength Grating Outcouplers in III-V Photonic Waveguides," in *SPIE Photonics West,* San Francisco, 2022.

[47] F. C. II, First Order Enhanced Coupling Strength (ECS) Gratings for Laser-Electro Absorption Modulator (EAM) Transmitter, Dallas, TX: Southern Methodist University, 2022.

[48] I. Geok, K. Radhakrishnan and H. Wang, "A Metamorphic HEMT and HBT Perspective," in *13th GaAs Symposium*, Paris, 2005.

[49] I. Futurrex, *Technical Information on Intermediate Coating IC1-200.*

[50] N. Stavitski, J. H. Klootwijk, H. W. v. Zeijl, A. Y. Kovalgin and R. A. M. Wolters, "Cross-Bridge Kelvin Resistor Structures for Reliable Measurement of Low Contact Reisstances and Contact Interface Characterization," *IEEE Transactions on Semiconductor Manufacturing. Vol. 22, No. 1,* p. 146, 2009.

[51] A. R. Clawson, "Guide to references on III±V semiconductor chemical etching," Materials Science and Engineering, 31, University of California at San Diego, CA, USA, 2000.

[52] C. Cremer and M. Schienle, "RIE etching of deep. Bragg grating filters in GaInAsP/InP," *Electronics Letter,* vol. 25, no. 17, pp. 1177-1178, 1989.

[53] T. W. Liepmann, "Wedged Plate Beam Splitter Without Ghost Reflections," *Applied Optics,* vol. 31, no. 28, pp. 5905-5906, 1992.

[54] Q. Wang and U. Griesmann, "Versatile bilayer resist for laser lithography at 405 nm on glass substrates," *Optical Engineering,* vol. 52, no. 10, 2013.

[55] Science, Brewer, *DUV 42P Datasheet*, Brewer Science.

[56] M. Lavagno and L. Scheffer, Electronic Design Automation For Integrated Circuits Handbook, CRC Press, 2014.

[57] D. Chemical, *Dow CYCLOTENE™ 4022-35 Advanced Electronic Resins*, Midland, MI: The Dow Chemical Company, 2006.

[58] H. Nishihara and T. S. Masamitsu Haruna, Optical Integrated Circuits, Mcgraw-Hill Oprical and Electro-Optical Engineering Series, 1987.

[59] A. Yariv, "Coupled Mode Theory for Guided-Wave Optics," *IEEE Journal of Quantum Electronics,* vol. 9, pp. 919-933, September 1973.

[60] Marcuse, "Radiation Loss of Grating-Assited Directional Coupler," *IEEE Journal of Quantum Electronics,* vol. 26, no. 4, pp. 675-684, April 1990.

[61] H. Kogelnik and C. V. Shank, "Coupled-Wave Theory of Distributed Feedback Lasers," *Journal of Applied Physics,* vol. 43, no. 5, 1972.

[62] W. Huang, "Coupled Mode Theory for Optical Waveguides-An Overview," *Optical Society of America,* vol. 11, no. 3, pp. 963-984, 1994.

[63] H. Haus, W. Huang, S. Kawakami and N. Whitaker, "Coupled Mode Theory of Optical Waveguides," *Journal of Lightwave Technology,* vol. 5, no. 1, 1987.

[64] D. Marcuse, "Directional Couplers Made Of Nonidentical Asymmetric Slabs. Part I Synchronous couplers," *Journal of Lightwave Technology,* vol. 5, no. 1, pp. 113-119, 1987.

[65] W. S. Park and S. R. Seshadri, "Theory of the Second-Order Reflection Grating," *Journal of Optical Society of America,* vol. 3, no. 10, 1986.

[66] A. Yariv and P. Yeh, Photonics: Optical Electronics in Modern Communications, London, U.K.: Oxford Univ. Press, 2007.

[67] R. H. Dennard, "Past progress and future challenges in LSI technology," *IEEE Solid-State Circuits Magazine,* vol. 7, no. 2, pp. 29-38, Jun 2015.

[68]